FY 2013 Summary Report: Post-Irradiation Examination of Zircaloy-4 Samples in Target Capsules and Initiation of Bending Fatigue Testing for Used Nuclear Fuel Vibration Integrity Investigations

Fuel Cycle Research & Development

Prepared for
U.S. Department of Energy
Used Fuel Disposition Campaign

R. H. Howard, Y. Yan, J. Wang,
L. J. Ott, R. L. Howard
Oak Ridge National Laboratory

September 30, 2013

FCRD-UFD-2013-000369

Approved for public release; distribution is unlimited.

DISCLAIMER

This information was prepared as an account of work sponsored by an agency of the U.S. Government. Neither the U.S. Government nor any agency thereof, nor any of their employees, makes any warranty, expressed or implied, or assumes any legal liability or responsibility for the accuracy, completeness, or usefulness, of any information, apparatus, product, or process disclosed, or represents that its use would not infringe privately owned rights. References herein to any specific commercial product, process, or service by trade name, trade mark, manufacturer, or otherwise, does not necessarily constitute or imply its endorsement, recommendation, or favoring by the U.S. Government or any agency thereof. The views and opinions of authors expressed herein do not necessarily state or reflect those of the U.S. Government or any agency thereof.

OAK RIDGE NATIONAL LABORATORY
MANAGED BY UT-BATTELLE FOR THE U.S. DEPARTMENT OF ENERGY

Oak Ridge National Laboratory is a multi-program laboratory managed and operated by UT-Battelle, LLC for the U.S. Department of Energy under contract DE-AC05-00OR22725.

SUMMARY

This report documents ongoing work performed at Oak Ridge National Laboratory (ORNL) for the Department of Energy, Office of Fuel Cycle Technology Used Fuel Disposition Campaign (UFDC), and satisfies the deliverable for milestone M2FT-13OR0805041, "Data Report on Hydrogen Doping and Irradiation in HFIR." This work is conducted under WBS 1.02.08.05, Work Package FT-13OR080504 ST "Storage and Transportation-Experiments – ORNL."

The objectives of work packages that make up the S&T Experiments Control Account are to conduct the separate effects tests (SET) and small-scale tests that have been identified in the Used Nuclear Fuel Storage and Transportation Data Gap Prioritization (FCRD-USED-2012-000109). In FY 2013, the R&D focused on cladding and container issues and small-scale tests as identified in Sections A-2.9 and A-2.12 of the prioritization report.

ORNL's FY 2013 activities included the following:

- Continue irradiation of hydrogen-doped cladding in High Flux Isotope Reactor (HFIR)
- Characterize and determine mechanical properties of first batch of cladding irradiated in HFIR
- Initiate activities to conduct fuel bend testing based on processes and protocols developed to support similar testing for the Nuclear Regulatory Commission
- Chair the ASTM International Subcommittee for Fuel Characterization standard

This page intentionally left blank.

CONTENTS

SUMMARY iii

1. Post-Irradiation Examination of Zircaloy-4 Samples in Target Capsules 1
   1.1 Introduction 1
   1.2 Specimen Preparation 2
      1.2.1 Description of Cladding Materials 2
      1.2.2 Hydrogen Charging 2
      1.2.3 Characterization of Hydrided Zircaloy-4 Specimens 5
   1.3 Neutron Irradiation of Hydrided Specimens in HFIR 8
      1.3.1 Design Description 8
      1.3.2 HFIR Operating Conditions during the Irradiation of HYCD-1 and HYCD-2 14
   1.4 Preliminary PIE Results of Irradiated Specimens HYCD-1 and HYCD-2 20
      1.4.1 Visual Examination of HYCD-1 and HYCD-2 20
      1.4.2 Dose Rate Measurements 27
      1.4.3 Optical Metallographic Examination 28
      1.4.4 Outer Diameter Measurements 34

2. THE DEVELOPMENT OF A REVERSAL BENDING FATIGUE TESTER FOR SPENT FUEL VIBRATION INTEGRITY INVESTIGATION 37
   2.1 Introduction 37
   2.2 Test System Concept 37
   2.3 Test System Development and Status 38
   2.4 Development of Measurement Methods 39
   2.5 Test Protocol and Experimental Demonstration 42
   2.6 Out-of-Cell Proof of Methodology Test Plan 44
   2.7 Out-of-Cell Proof of Methodology Testing Using Zircaloy-4 Samples 48
   2.8 MONOTONIC TEST 49
   2.9 CYCLE TEST 49

3. RESULTS OF MONOTONIC TEST 49
   3.1 Surrogate Rod with Epoxy Bond 49
   3.2 Surrogate Rod without Epoxy Bond 52

4. RESULTS OF CYCLE TEST 53
   4.1 Summary 53
   4.2 Surrogate Rod with Epoxy Bond 54
      4.2.1 5 Hz Cycle Tests 54

5. REFERENCES 65

APPENDIX A DOSE RATE SURVEY REPORT ON HYCD-1 AND HYCD-2 67

APPENDIX B HYDRIDED ZIRCALOY-4 AND ZIRLO SAMPLES FOR HFIR IRRADIATION 69

APPENDIX C DRAWING X3E020977A608 71

FIGURES

Figure 1. The 901 Brew Furnace for hydrogen doping. 3
Figure 2. Temperature profile for hydriding cladding materials. 3
Figure 3. Hydrided Zircaloy-4 showing surface discolor. 4
Figure 4. New static hydriding system. 4
Figure 5. LECO RH-404 Hydrogen Analyzer used for determining the hydrogen content. 5
Figure 6. Hydrogen distribution for pre-hydrided Zircaloy-4 sample at 400°C for 8 hours with mixed gases of hydrogen and argon. 6
Figure 7. Micrographs showing hydride distributions in hydrogen-charged Zircaloy-4 samples. The average hydrogen content of this location is ≈70 wppm. 6
Figure 8. Micrographs showing hydride distributions in hydrogen-charged Zircaloy-4 samples. The average hydrogen content of this location is ≈150 wppm. 7
Figure 9. Micrographs showing hydride distributions in hydrogen-charged Zircaloy-4 samples. The average hydrogen content of this location is ≈320 wppm. 7
Figure 10. Micrographs showing hydride distributions in hydrogen-charged Zircaloy-4 samples. The average hydrogen content of this location is ≈610 wppm. 8
Figure 11. Cross section through HFIR illustrating the primary experimental sites (left) and a picture of the reactor core (right). 9
Figure 12. Flux trap irradiation locations for HYCD-1, HYCD-2, and HYCD-3. 10
Figure 13. HFIR fast neutron flux in the E3, E6, and C2 flux trap positions. 10
Figure 14. Experiment assembly schematic. 12
Figure 15. HYCD-1 Specimen loading. 13
Figure 16. HYCD-2 specimen loading. 14
Figure 17. HFIR operating history during the HYCD-1 and HYCD-2 irradiations. 15
Figure 18. Fast fluence (>1.0 MeV) in the HYCD-1 specimens. 16
Figure 19. Fast fluence (>1.0 MeV) in the HYCD-2 specimens. 17
Figure 20. HFIR operating temperatures in the HYCD-1 and HYCD-2 specimens. 18
Figure 21. Operating radial temperature drop in the HYCD-1 and HYCD-2 specimens. 19
Figure 22. Loop cask for HYCD-1 and HYCD-2 (OD × L =2 ft × 8 ft) at the IFEL. 20
Figure 23. HYCD-1 and HYCD-2 capsules in the North Cell of Building 3525. 21
Figure 24. In-cell milling to remove the cladding specimen from the capsule. 21
Figure 25. Illustration of removing the cladding specimens from the capsule. 23
Figure 26. HYCD-1 samples on molybdenum heater rod. 24
Figure 27. HYCD-2 samples on molybdenum heater rod. 24
Figure 28. Specimens removed from HYCD-1. 25

Figure 29. Specimens removed from HYCD-2. 26
Figure 30. High-magnification image of Specimen UFC1D1E. 27
Figure 31. Schematic illustration of the dose rate measurement on HYCD-1 and HYCD-2. 27
Figure 32. A diamond saw for radioactive sample sectioning in hot cell. 29
Figure 33. Five rings sectioned from Sample UFC1D1C, Capsule HYCD-1. 29
Figure 34. Five rings sectioned from Sample LRR1D7, Capsule HYCD-2. 30
Figure 35. Mount 6376, prepared from Sample UFC1D1C of Capsule HYCD-1. No unusual behavior was noted. 31
Figure 36. Mount 6377, prepared from Sample LRR1D7 of Capsule HYCD-2. Two through-wall cracks were observed. 32
Figure 37. High-magnification images of the two cracks observed in Figure 36. 33
Figure 38. Measurement sensor. 34
Figure 39. Measurement probe contacting pin gauge (black item in slot). 35
Figure 40. Display of the measure sensor. 35
Figure 41. U-frame-assisted bending fatigue testing setup for reversal bending when rigid arms are (a) closing, (b) neutral, and (c) opening. 38
Figure 42. Stress distribution in a fuel rod with compliant layer when the applied force was 178 N; the unit of stress is psi. The maximum von Mises stress is 220 MPa (3.185×104 psi). 38
Figure 43. Integrated ORNL U-frame Bose dual linear motor test bench. A horizontal arrangement is used to eliminate the effect of the U-frame mass on the specimen. 39
Figure 44. Three-point measurement method for the curvature of specimen through three LVDTs. The demonstration is on the U-frame setup equipped with linear ball bearings and integrated onto a MTS 810 servo-hydraulic test machine. 40
Figure 45. (a) Moment curve, (b) curvature curve, and (c) moment–curvature loops obtained by use of 3G U-frame with preloaded LRBs. The results are based on the rod made of SS tube only using the LRB U-frame on MTS 810 test machine under ±180 N, 10 N/s. 40
Figure 46. Moment-curvature response and the associated system rigidity evaluation. 41
Figure 47. Test protocol for reversal bending test. 42
Figure 48. Variation of (a) curvature, (b) moment, and (c) rigidity based on on-line monitoring of SSAP05: ±3 mm, 2 Hz. Specimen with octagonal rigid sleeve without Teflon sheets attached; $N_f = 3.7\times10^4$ cycles. 43
Figure 49. Cycling loading results in increases in curvature and hysteresis; measurements were conducted under load control mode on SSAP06 sample. 43
Figure 50. (a) Flexural rigidity property change results from cyclic loading. The measurements were conducted under static cyclic loading at specified points of cycle test. (b) Moment-curvature curves appeared to be quite linear in the tested range for SSAP04. Higher flexural rigidity was observed compared to SSAP02 due to epoxy bond of SSAP04. More significant decrease was observed in rigidity at higher cycles. 44

Figure 51. Axial tensile test results for stainless steel tubing used as surrogate rod for bending testing.....45

Figure 52. Integrated Bose reversal U-bent tester used for static and dynamic fatigue bending testing.....45

Figure 53. Static bending test result reveals good repeatability of developed testing protocol.....46

Figure 54. Reversal bending fatigue tests of SSAP samples show typical S-N trend; cycles of SSAP26 include 5.4 M at 10 Hz testing; SSAP25 was irradiated 2 weeks between six and seven fuel rod layers, and SSAP27 was irradiated in the same fuel pile for 4 weeks.....46

Figure 55. The evolution of SSAP flexural rigidities under different reversal bending fatigue loadings.....47

Figure 56. Test for SSAP11 was conducted on Bose with original setup: load ±200 N, moment ±20.38 N*m, 5 Hz. Initial displacement ±2.5 mm, initial curvature ±0.27 /m, initial strain ±0.14%. Specimen fractured near 678K cycles. About 40% drop in flexural rigidity occurred. 48

Figure 57. Test for SSAP12 was conducted on Bose with modified setup under condition: load ±200 N, moment ±20.38 N*m, 5 Hz. Initial displacement ±2 mm, initial curvature ±0.23/m, initial strain ±0.13%. Specimen fractured near 936 K cycles. About 42% drop in flexural rigidity.....48

Figure 58. (a) Moment, (b) curvature, and (c) moment–curvature curve for static bending test of ZRAP01 under 0.2 mm/s and maximum relative displacement of 20 mm at loading points of U-frame setup. 50

Figure 59. (a) Moment, (b) curvature, and (c) moment–curvature curve for static bending test of ZRAP12 under 0.2 mm/s and maximum relative displacement of 20 mm at loading points of U-frame setup. 51

Figure 60. Multiple transverse cracks developed on the surface of ZRAP01 during monotonic loading. 51

Figure 61. (a) Moment, (b) curvature, and (c) moment–curvature curve for static bending test of ZRAPM01 under 0.2 mm/s and maximum displacement of 20 mm at loading points of U-frame setup. 52

Figure 64 . Variation of (a) curvature, (b) moment, and (c) rigidity based on online monitoring; measurement results for (d) curves of moment versus curvature and (e) flexural rigidity versus curvature of ZRAP03: ±200 N, 5 Hz.....56

Figure 65. Variation of (a) curvature, (b) moment, and (c) rigidity based on online monitoring; measurement results for (d) curves of moment versus curvature and (e) flexural rigidity versus curvature of ZRAP04: ±150 N, 5 Hz.....57

Figure 66. Variation of (a) curvature, (b) moment, and (c) rigidity based on online monitoring; measurement results for (d) curves of moment versus curvature and (e) flexural rigidity versus curvature of ZRAP09: ±150 N, 5 Hz.....58

Figure 67. Variation of (a) curvature, (b) moment, and (c) rigidity based on online monitoring; measurement results for (d) curves of moment versus curvature and (e) flexural rigidity versus curvature of ZRAP10: ±175 N, 5 Hz.....59

Figure 68. Variation of (a) curvature, (b) moment, and (c) rigidity based on online monitoring; measurement results for (d) curves of moment versus curvature and (e) flexural rigidity versus curvature of ZRAP11: ±200 N, 5 Hz. 60

Figure 69. Variation of (a) curvature, (b) moment, and (c) rigidity based on online monitoring; measurement results for (d) curves of moment versus curvature and (e) flexural rigidity versus curvature of ZRAP13: ±250 N, 5 Hz. 61

Figure 70. Variation of (a) curvature, (b) moment, and (c) rigidity based on online monitoring; measurement results for (d) curves of moment versus curvature and (e) flexural rigidity versus curvature of ZRAP14: ±300 N, 5 Hz. 62

Figure 71. Images showing fractured rods for (a) ZRAP03, (b) ZRAP04, (c) ZRAP09, (d) ZRAP10, and (e) ZRAP11. 63

Figure 72. Micrograph of part of the surface of ZRAP13 rod showing transverse fracture of about 4 mm length kinked near a surface flaw. 64

TABLES

Table 1. Dimensions and chemistry of Zircaloy-4 and ZIRLO used in the ORNL test program (the “<” sign indicates below the testing detection limit). 2

Table 2. HYCD-1 clad specimens. 12

Table 3. HYCD-2 clad specimens. 13

Table 4. HFIR-powered operation for Cycles 440B, 441, and 442. 15

Table 5. HYCD-1 clad specimen fast fluences (>1.0 MeV). 16

Table 6. HYCD-2 clad specimen fast fluences (>1.0 MeV). 17

Table 7. Operating temperatures in the HYCD-1 and HYCD-2 clad specimen(s). 19

Table 8. Dose rates on the HYCD-1 and HYCD-2 specimens. 28

Table 9. Summary of the MET mounts for optical metallographic examination. 30

Table 10. Outer diameter measurement for as-fabricated and hydrided samples before the HFIR irradiation. 36

Table 11. Outer diameter measurement of the specimens from Capsule HYCD-1. 36

Table 12. Outer diameter measurement of the specimens from Capsule HYCD-2. 36

Table 13. Summary of Zircaloy-4 surrogate rod tests. 53

ACRONYMS

DAC	design analysis and calculation
FEA	finite-element analysis
HFIR	High Flux Isotope Reactor
IFEL	Irradiated Fuel Examination Lab
LRB	linear roller bearings
LVDT	linear variable differential transformer
LWR	light water reactor
MET	metallographic
OD	outer diameter
ORNL	Oak Ridge National Laboratory
PIE	post-irradiation examination
RT	room temperature
SET	separate effects tests
SS	stainless steel
UFDC	Used Fuel Disposition Campaign
UNF	used nuclear fuel
UTS	ultimate tensile strength
VLTS	very long-term storage
wppm	parts per million by weight

This page intentionally left blank.

USED FUEL DISPOSITION CAMPAIGN

FY 2013 SUMMARY REPORT: POST-IRRADIATION EXAMINATION OF ZIRCALOY-4 SAMPLES IN TARGET CAPSULES AND INITIATION OF BENDING FATIGUE TESTING FOR USED NUCLEAR FUEL VIBRATION INTEGRITY INVESTIGATIONS

1. POST-IRRADIATION EXAMINATION OF ZIRCALOY-4 SAMPLES IN TARGET CAPSULES

1.1 Introduction

During normal reactor operations, the nuclear fuel in a reactor experiences corrosion, which results in the formation of a waterside corrosion layer (oxide) and the introduction of hydrogen into the zirconium (Zr) cladding via the reaction $2H_2O+Zr \rightarrow ZrO_2+4H$. With increasing corrosion, the hydrogen concentration in the cladding will exceed its terminal solid solubility and brittle zirconium hydrides ($Zr+2H \rightarrow ZrH_2$) may precipitate as the cladding cools. This causes cladding ductility and failure energy to decrease [1–3], weakening the cladding. This cladding degradation due to hydride precipitates increases the likelihood of cladding failure during very long-term storage and/or transportation of used nuclear fuel (UNF).

The DOE Used Fuel Disposition Campaign (UFDC) tasked Oak Ridge National Laboratory (ORNL) to investigate the behavior of light-water-reactor (LWR) fuel cladding material performance related to extended storage and transportation of UNF. Fast-neutron irradiation of pre-hydrided zirconium-alloy cladding in the High Flux Isotope Reactor (HFIR) at elevated temperatures has been used to simulate the effects of high burnup on fuel cladding for help in understanding the cladding materials properties relevant to very long-term storage (VLTS) and subsequent transportation. The irradiated pre-hydrided metallic materials testing will generate baseline data to benchmark hot-cell testing of actual high-burnup UNF cladding. More importantly, the HFIR irradiated samples will be free of alpha contamination and can be provided to researchers who do not have hot cell facilities to handle highly contaminated high-burnup UNF cladding to support their research projects for the UFDC.

In order to accomplish this research, ORNL has produced unirradiated zirconium-based cladding tubes with various known hydrogen concentrations. Four capsules (HYCD-1 to HYCD-4) containing 3.0 in. (7.62 cm) to 6.0 in. (15.24 cm) hydrided zirconium-based samples were inserted into HFIR for neutron irradiation in HFIR Cycle 440B. HYCD-1 was removed after one irradiation cycle (440B), and HYCD-2 was removed after three irradiation cycles (442). This report summarizes the characterization work that has been performed so far on HYCD-1 and HYCD-2. Capsules HYCD-3 and HYCD-4 have been removed from HFIR, but have not cooled sufficiently to move for further characterization.

1.2 Specimen Preparation

1.2.1 Description of Cladding Materials

Sandia National Laboratories provided ORNL with several cladding rods that are prototypic of nuclear-grade 17×17 Zircaloy-4 and ZIRLO assemblies. Measurements were performed to determine the OD, wall thickness, and chemical composition of the cladding material. Table 1 summarizes the dimensions and measured chemical composition of the Zircaloy-4 and ZIRLO cladding, along with nominal composition Zircaloy-4 cladding specified in ASTM B811.

Table 1. Dimensions and chemistry of Zircaloy-4 and ZIRLO used in the ORNL test program (the "<" sign indicates below the testing detection limit)

Parameter	Zircaloy-4[a]	17×17 Zircaloy -4	17×17 ZIRLO
OD, mm	---	9.50	9.50
Wall thickness, mm	---	0.57	0.57
Sn, wt.%	1.45	1.26	0.97
Nb, wt.%			0.98
O, wt.%	0.125	0.13	0.12
Fe, wt.%	0.21	0.22	0.08
Cr, wt.%	0.10	0.10	---
S, wppm			<10
C, wppm			90
N, wppm			50
H, wppm		10	12
Zr	Balance	Balance	Balance

[a]ASTM B811 for nominal composition of commercial Zircaloy-4 cladding.

1.2.2 Hydrogen Charging

Samples for hydriding were prepared by chemical etching in an acid blend of 49.5% nitric acid, 49.5% hydrogen peroxide, and 1% hydrofluoric acid and were then cleaned using ultrasonic baths at room temperature (RT) ethanol and water.

The zirconium cladding samples were hydrogen charged by the gaseous method at high temperature [4–5]. The target hydrogen concentrations ranged from tens of wppm to a few hundreds of wppm. The hydriding system used for hydrogen loading in this report is shown in Figure 1. It consisted of a furnace that was heated to 400–450°C in the presence of hydrogen to introduce the desired quantity of hydrogen into the sample [6]. The chamber was evacuated (up to three times, to ≈30 mm Hg below atmospheric pressure) before being filled with the charging gas, 96% Ar, 4% H_2, to reduce oxidation on the surface of the cladding. The temperature, charging gas flow rate, and test duration were optimized to achieve the desired hydrogen concentration. The samples were then cooled in the furnace in a pure argon environment. A typical temperature profile used for hydrogen charging is shown in Figure 2. After the hydrogen charging process, the sample surface was often slightly discolored, as shown in Figure 3. A new static hydriding system (Figure 4) was developed at ORNL in which the hydrogen loading in the cladding is more predictable. Specimens used for HYCD-4 were fabricated using the new hydriding system.

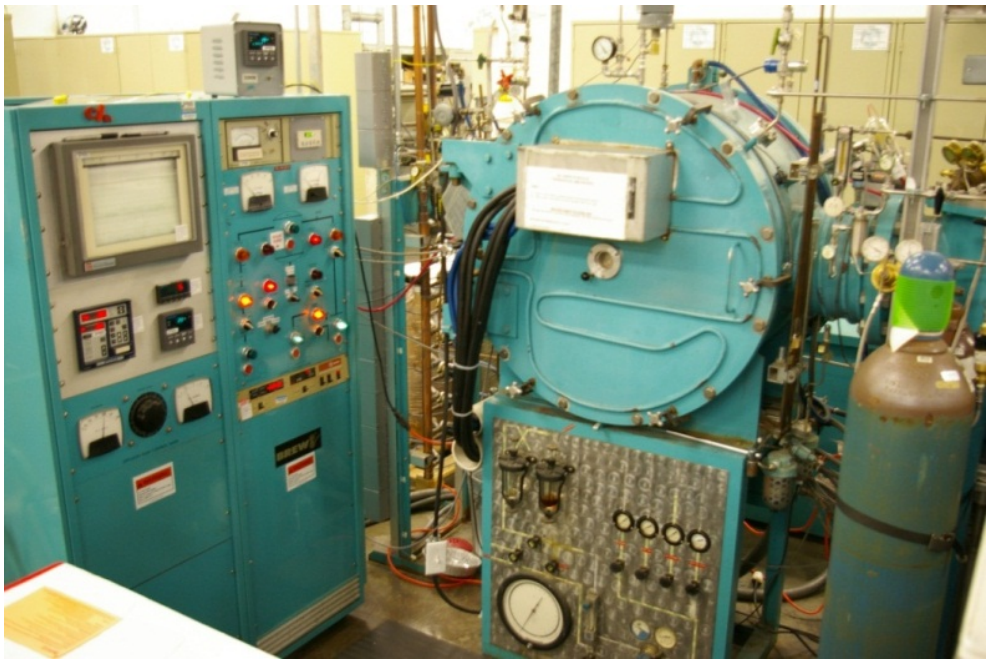

Figure 1. The 901 Brew Furnace for hydrogen doping.

Figure 2. Temperature profile for hydriding cladding materials.

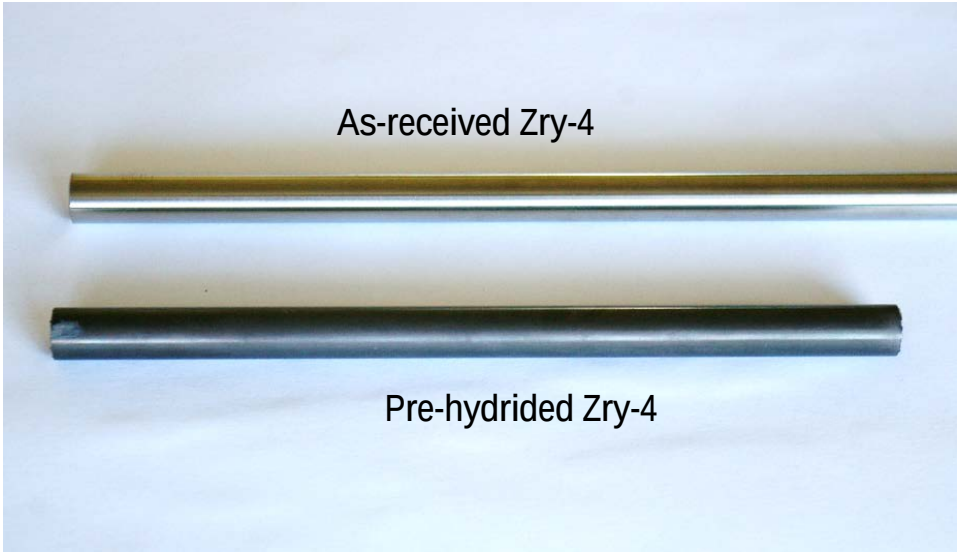

Figure 3. Hydrided Zircaloy-4 showing surface discoloration.

Figure 4. New static hydriding system.

1.2.3 Characterization of Hydrided Zircaloy-4 Specimens

The hydrogen content of the hydrided specimens was measured using the Vacuum Hot Extraction technique per ASTM E146-83. A LECO RH-404 Hydrogen Analyzer was used for hydrogen analysis, as shown in Figure 5. The equipment was verified using standards of known hydrogen content before each test. Under optimized test conditions, a relatively uniform hydrogen distribution along the axial direction was obtained (Figure 6). However, it was difficult to obtain repeatable hydrogen doping results with the 901 Brew Furnace. A new static system (Figure 4) was developed to improve material hydriding.

Metallographic examinations were performed on hydrided Zircaloy-4 samples. Although axial gradients in hydrogen content are sometimes observed in hydrided Zircaloy-4 samples, the ORNL hydriding procedure resulted in a uniform distribution of circumferential hydrides across the Zircaloy-4 wall. As shown in Figure 7–Figure 10, the hydride density increased as the hydrogen concentration in the sample increased. The measurements indicated the hydrogen content of the specimens shown in Figure 7–Figure 10 were from 70 to 610 wppm.

Figure 5. LECO RH-404 Hydrogen Analyzer used for determining the hydrogen content.

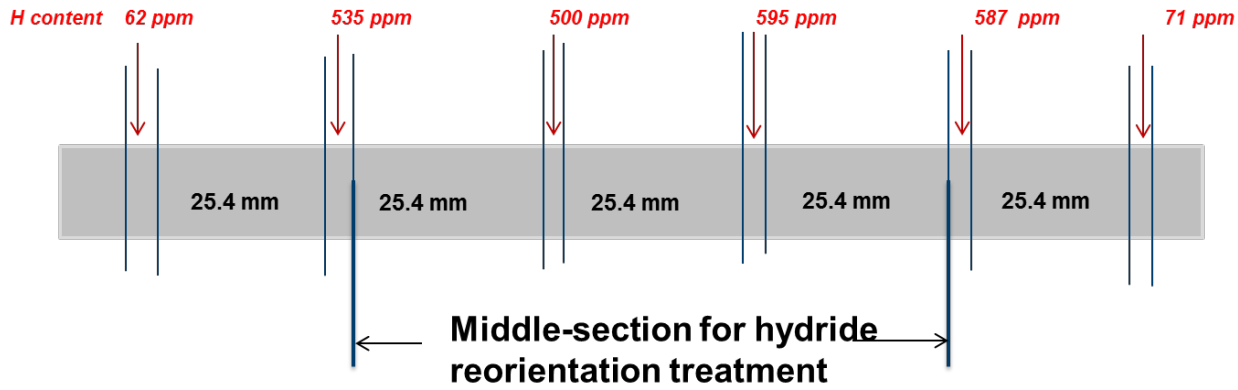

Figure 6. Hydrogen distribution for pre-hydrided Zircaloy-4 sample at 400°C for 8 hours with mixed gases of hydrogen and argon.

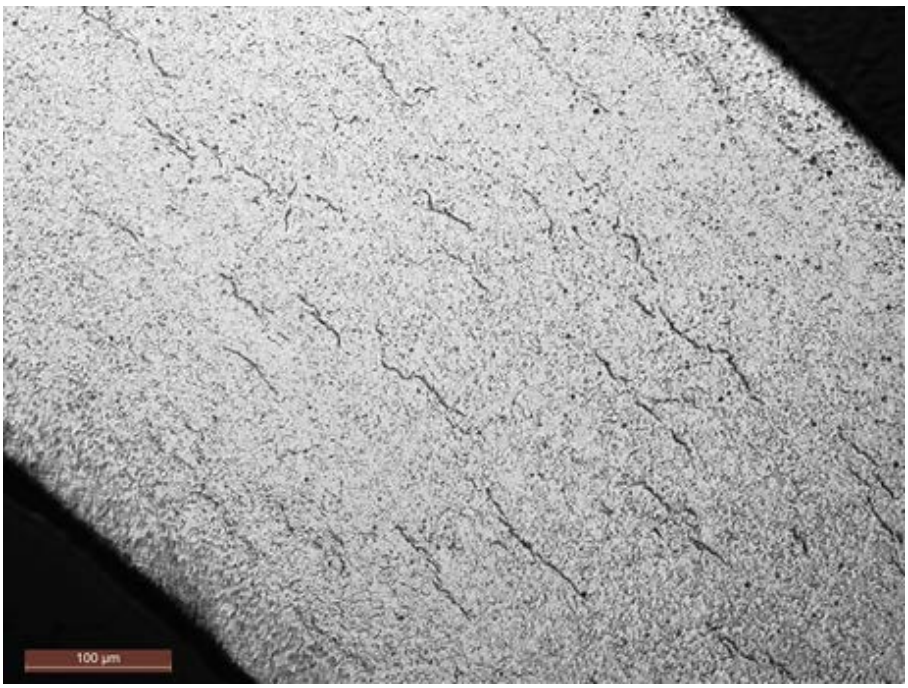

Figure 7. Micrographs showing hydride distributions in hydrogen-charged Zircaloy-4 samples. The average hydrogen content of this location is ≈70 wppm.

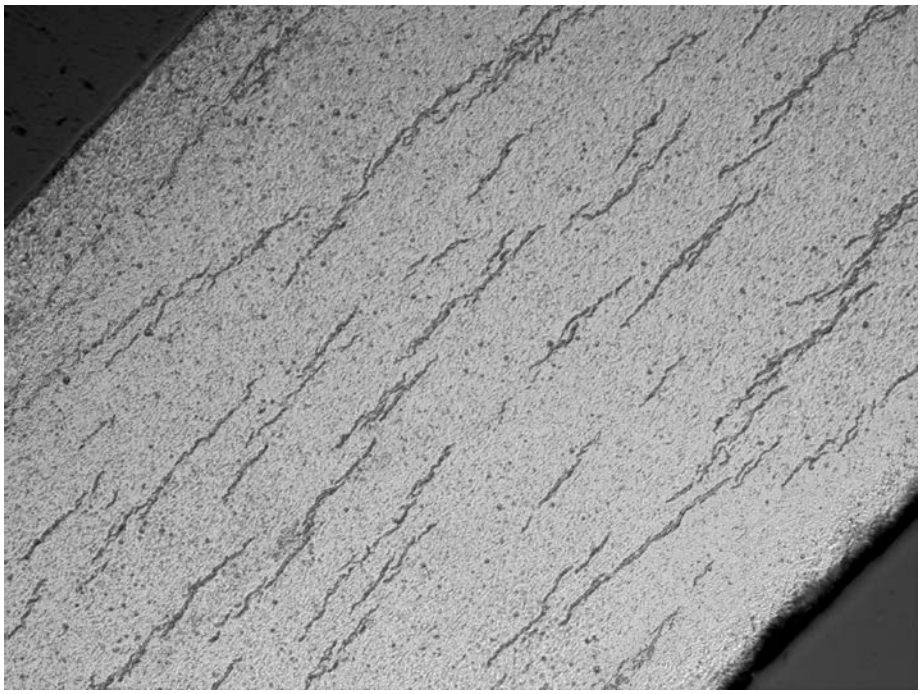

Figure 8. Micrographs showing hydride distributions in hydrogen-charged Zircaloy-4 samples. The average hydrogen content of this location is ≈150 wppm.

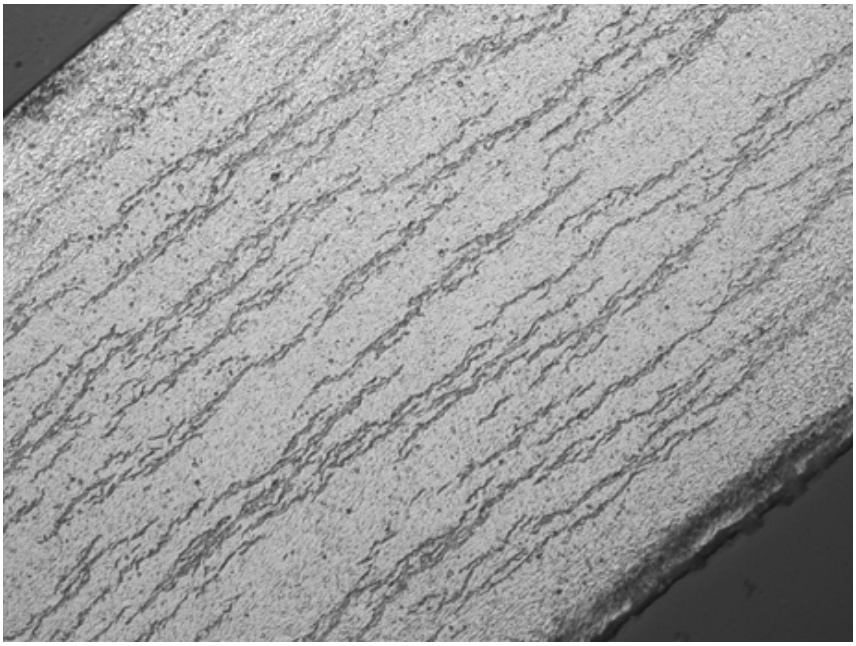

Figure 9. Micrographs showing hydride distributions in hydrogen-charged Zircaloy-4 samples. The average hydrogen content of this location is ≈320 wppm.

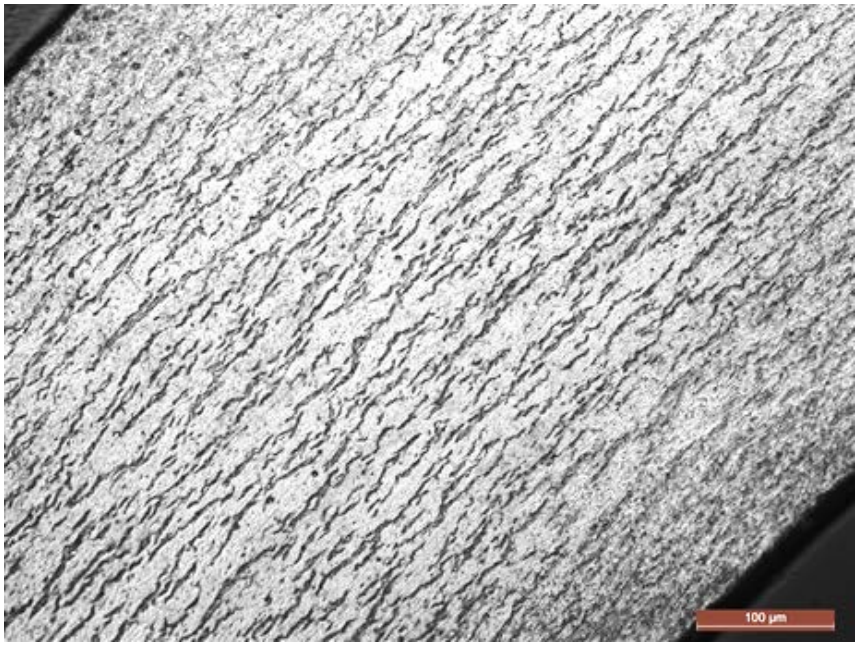

Figure 10. Micrographs showing hydride distributions in hydrogen-charged Zircaloy-4 samples. The average hydrogen content of this location is ≈610 wppm.

1.3 Neutron Irradiation of Hydrided Specimens in HFIR

Preparation of the hydride cladding specimens, as discussed in Section 1.2, resulted in the hydrides being uniformly distributed within the cladding. This parameter is not prototypic of the hydride morphology generated under normal LWR operation where the hydrides are more concentrated on the outside (OD) portions of the cladding. Under HFIR test irradiation conditions (at a prototypic LWR cladding surface temperature and temperature gradient across the cladding wall), normal cladding end-state hydride morphology inside the cladding was expected after irradiation. Two capsules (HYCD-1 and HYCD-2) were removed from the reactor after the first and third cycles of irradiation, respectively, for post-irradiation examination (PIE) to determine the resulting end-state hydride morphology. However, as described later in Section 1.4, there were difficulties in removing the specimens from the capsules after irradiation and the prototypic morphology was not achieved in the initial test. . The remainder of this section summarizes the general design and irradiation set up for all for capsules and the as-irradiated conditions (fluences and temperatures) for HYCD-1 and HYCD-2. The as-irradiated conditions for HYCD-3 and HYCD-4 will be provided at a future date as these capsules were not removed from the HFIR until June 2013.

1.3.1 Design Description

1.3.1.1 HFIR Target Facilities

HFIR is a beryllium-reflected, pressurized, light-water-cooled and moderated flux-trap-type reactor. The core consists of aluminum-clad involute-fuel plates, which currently utilize highly enriched ^{235}U fuel at a power level of 85 MWt.

The reactor core, illustrated in Figure 11, consists of two concentric annular regions, each approximately 61 cm in height. The flux trap is ~12.7 cm in diameter, and the outer fueled region is ~43.5 cm in diameter. The fuel region is surrounded by a beryllium annular reflector approximately 30.5 cm in thickness. The beryllium reflector is in turn backed up by a water reflector of effectively infinite thickness. In the axial direction, the reactor is reflected by water. The reactor core assembly is contained in a 2.44 m diameter pressure vessel, which is located in a 5.5 m cylindrical pool of water.

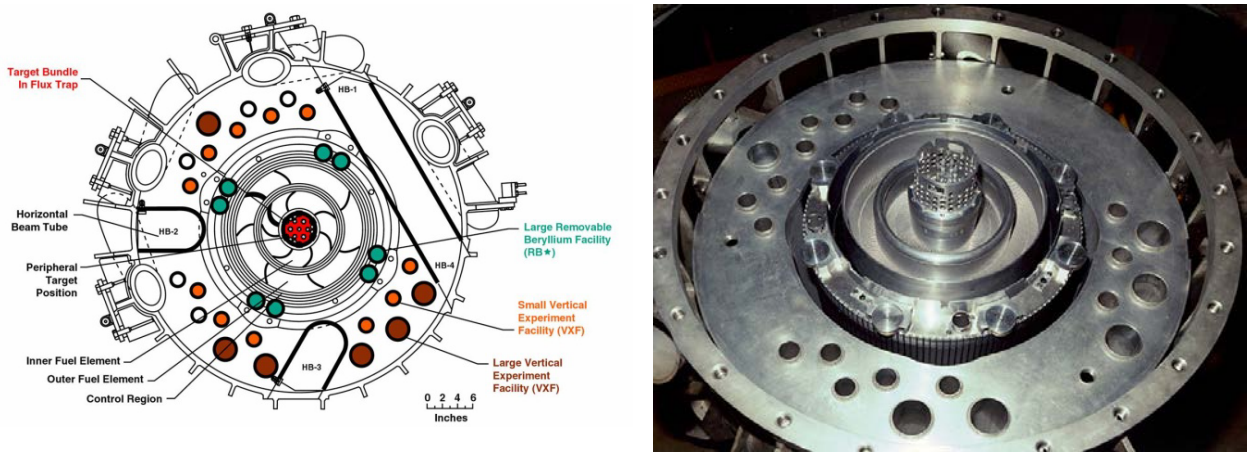

Figure 11. Cross section through HFIR illustrating the primary experimental sites (left) and a picture of the reactor core (right).

HYCD-1, HYCD-2, and HYCD-3 were placed in the flux trap of HFIR in positions E3, E6, and C2, respectively, as shown in Figure 12. The fast neutron flux in these positions in HFIR is illustrated in Figure 13 (as a function of core height).

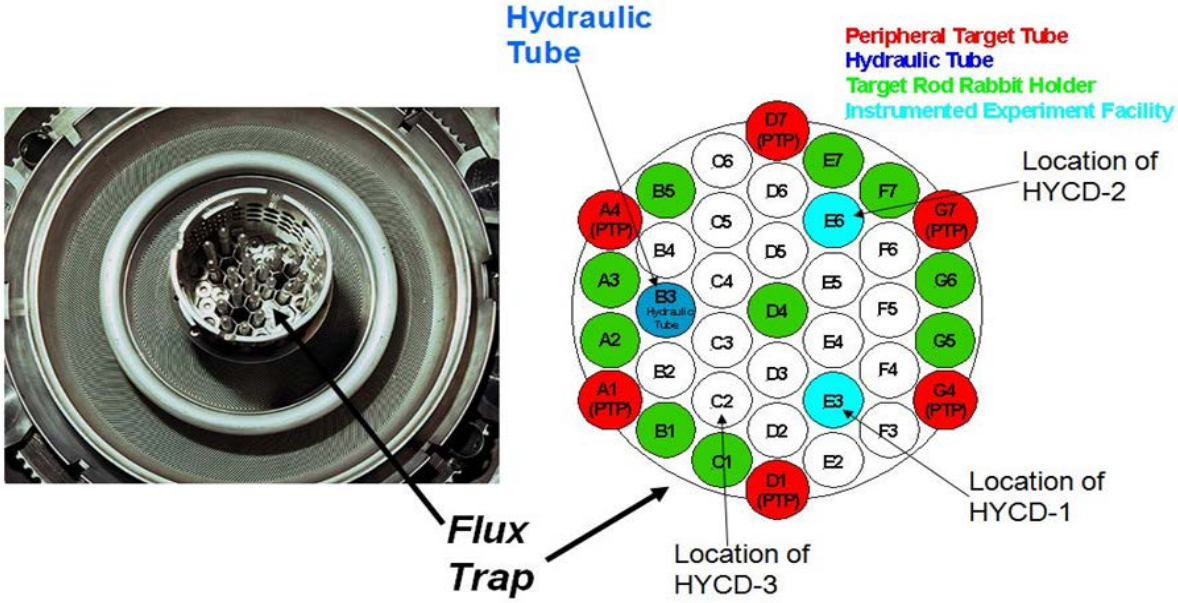

Figure 12. Flux trap irradiation locations for HYCD-1, HYCD-2, and HYCD-3.

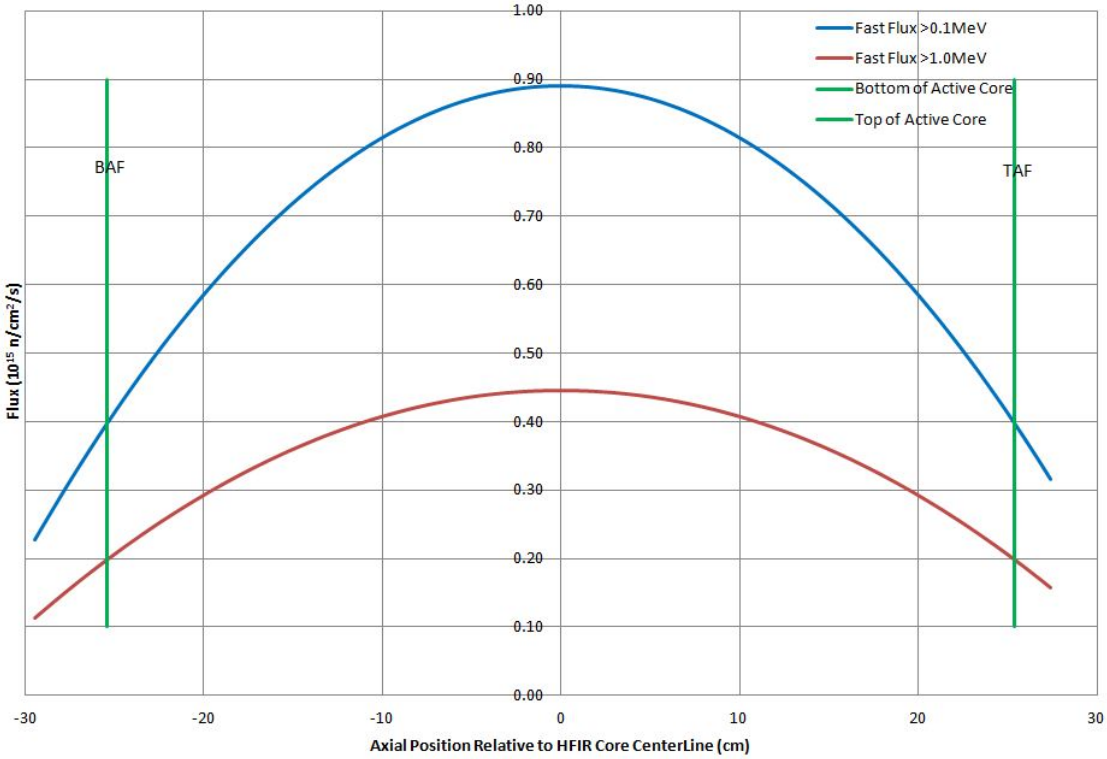

Figure 13. HFIR fast neutron flux in the E3, E6, and C2 flux trap positions.

1.3.1.2 General Experiment Design Description

The experiment assembly is shown on Drawing X3E020977A608 (Appendix C). A schematic of the assembly around the test specimens is illustrated in Figure 14.

Coolant is directed to the experiment by the Al-6061 outer shroud. The outer aluminum housing is the primary containment for the experiment and is also fabricated from Al-6061. The housing is made from No. 17, ½-in. Al-6061 tubing, which has an inner diameter of 9.73 mm (0.383 in.). The ends of the tubing are bored out to an inner diameter of 11.3 mm (0.445 in.) to meet the requirements of the existing design for the top and bottom caps and to support the approved weld procedures.

The Zircaloy-4 clad specimens have an outer diameter of 9.5 mm (0.3741 in.) and an inner diameter of 8.35 mm (0.3287 in.). The clad lengths will range from 76 mm (3.00 in.) to 152 mm (6.00 in.). The clad is fitted with a molybdenum rod that acts as a heater for the cladding. The molybdenum rod is 102 mm (4 in.) long for the 76 mm clad case and 178 mm (7 in.) long for the 152 mm clad case. The axial location of the clad centroid is located at the reactor mid-plane. Spacers made from ⅜ in. Al-6061 tubing are used to ensure this placement. For the 76 mm clad case, the top and bottom spacers are 224 mm (8.82 in.) and 227 mm (8.95 in.), respectively. Similarly, for the 152 mm clad case, the top and bottom spacers are 183 mm (7.22 in.) and 189 mm (7.45 in.), respectively. Both spacer sets are counterbored 12 mm (0.5 in.) at the end oriented closest to the reactor centerline to hold the excess molybdenum heater rod while also keeping the clad in the proper location. Six equal-spaced pads are punched into the ends of each spacer closest to the reactor centerline. This feature produces a slightly larger diameter than the original outer diameter of the spacer tube, and this dimension is set to keep the experiment centered in the housing tube.

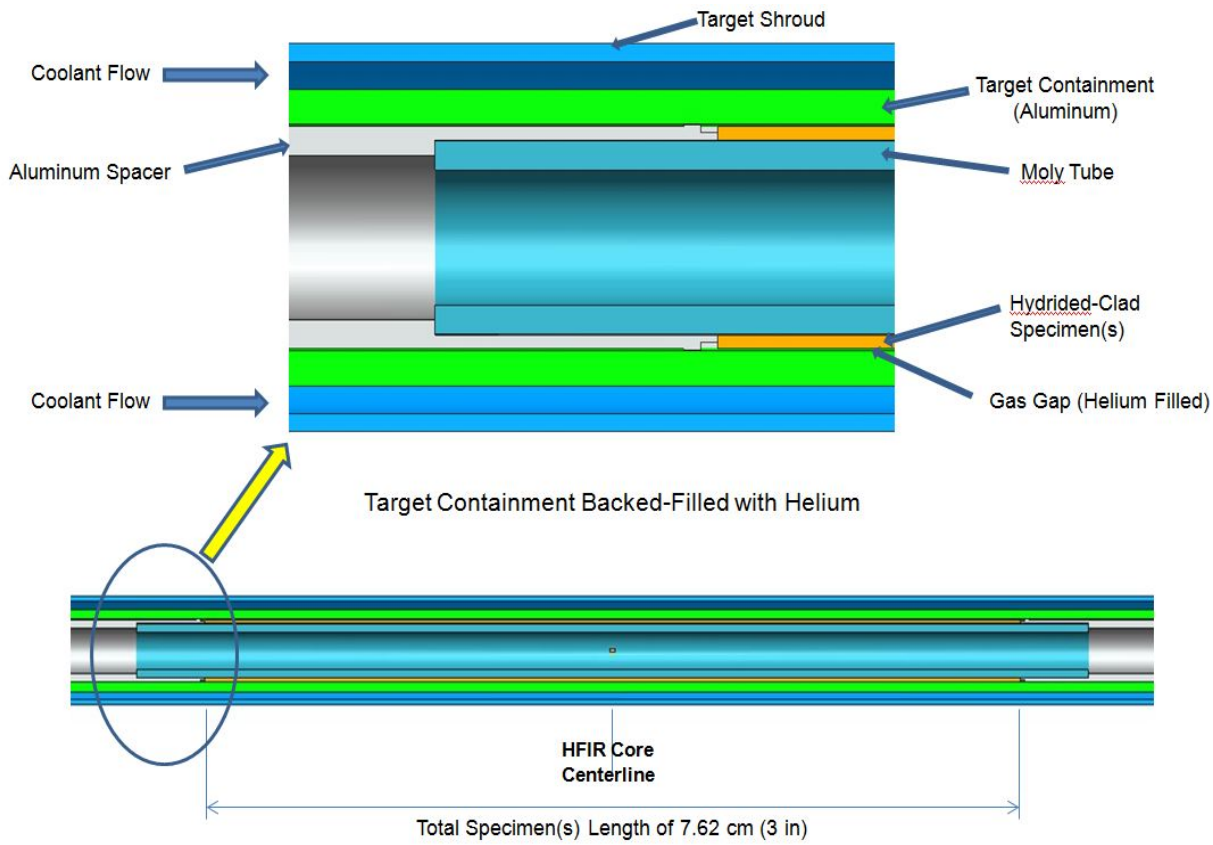

Figure 14. Experiment assembly schematic.

1.3.1.3 HYCD-1 Assembly Description

The clad specimen hydrogen contents (three samples, each 1 in. [2.54 cm] in length) utilized in HYCD-1 are provided in Table 2. The location of these specimens within the experiment assembly is shown in Figure 15.

Table 2. HYCD-1 clad specimens [1]

Specimen ID	Hydrogen content (wppm)
LRR4A20	<20
LRR1B5	~820
UCF1D1C	~450

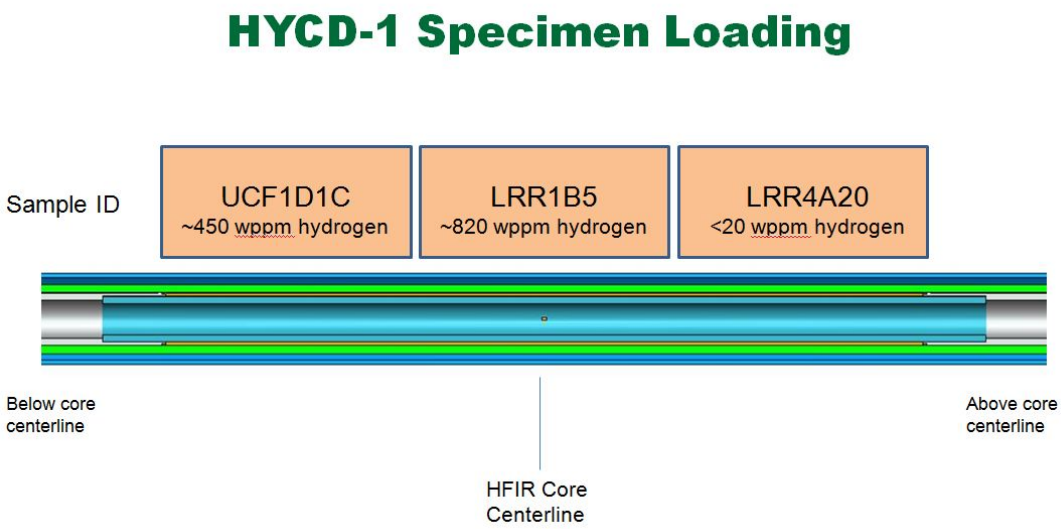

Figure 15. HYCD-1 specimen loading.

1.3.1.4 HYCD-2 Assembly Description

The clad specimen hydrogen contents (three samples, each 1 in. [2.54 cm] in length) utilized in HYCD-2 are provided in Table 3. The location of these specimens within the experiment assembly is shown in Figure 16.

Table 3. HYCD-2 clad specimens

Specimen ID	Hydrogen content (wppm)
LRR4A23	<20
LRR1D7	~550
UCF1D1E	~450

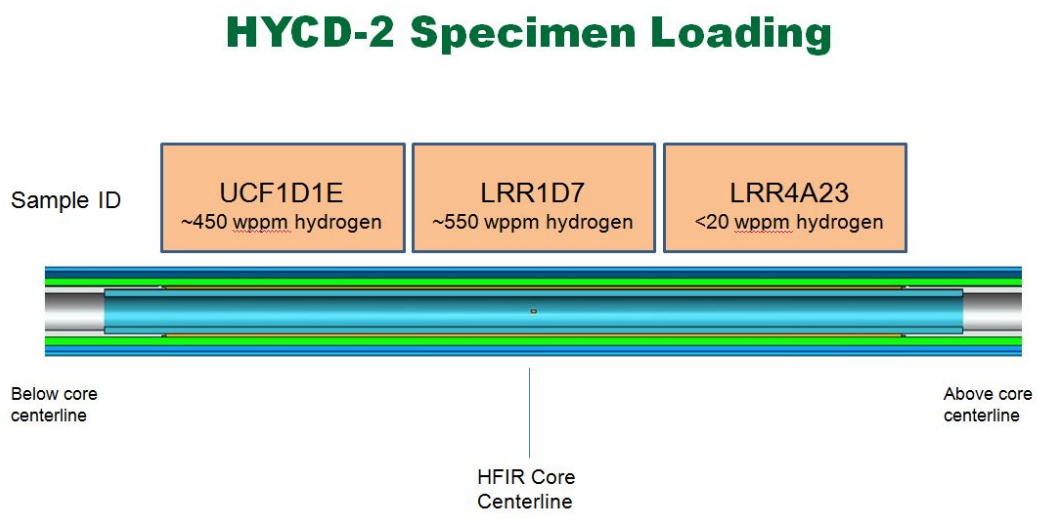

Figure 16. HYCD-2 specimen loading.

1.3.2 HFIR Operating Conditions during the Irradiation of HYCD-1 and HYCD-2

1.3.2.1 HFIR Operating History

HYCD-1, HYCD-2, and HYCD-3 were inserted in HFIR for Cycle 440B on March 26, 2012; HYCD-1 was removed after Cycle 440B and HYCD-2 after Cycle 442. The HFIR operating history for these cycles is illustrated in Figure 17. (Note that HYCD-4 was not inserted until November 20, 2012 that HYCD-3 and HYCD-4 were removed after Cycle 447).

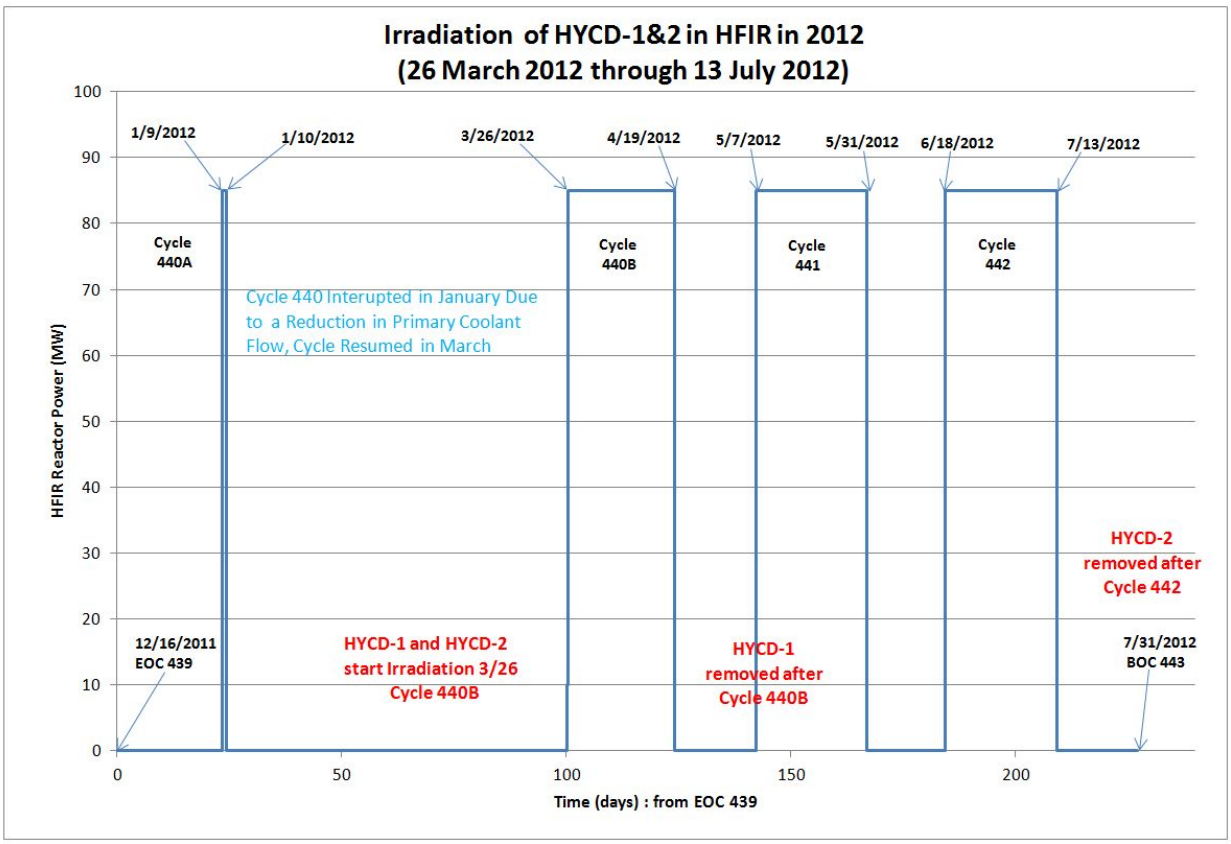

Figure 17. HFIR operating history during the HYCD-1 and HYCD-2 irradiations.

The days of powered operation for Cycles 440B, 441, and 442 are given in Table 4 (from operator logs on power ascension until time of SCRAM).

Table 4. HFIR-powered operation for Cycles 440B, 441, and 442

Cycle	Powered Operation (days)
440B	23.84
441	24.66
442	24.90

1.3.2.2 HYCD-1 and HYCD-2 Accumulated Fast Fluence

Given the neutron flux at the E3 and E6 positions (illustrated in Fig. 13) and the periods of powered operation in HFIR (Table 4), it is a straightforward calculation to determine the fast (>1.0 MeV) neutron fluence attained by the HYCD-1 and HYCD-2 specimens. The fast fluence (>1.0 MeV) accumulated in the HYCD-1 specimens is shown in Figure 18 and tabulated in Table 5.

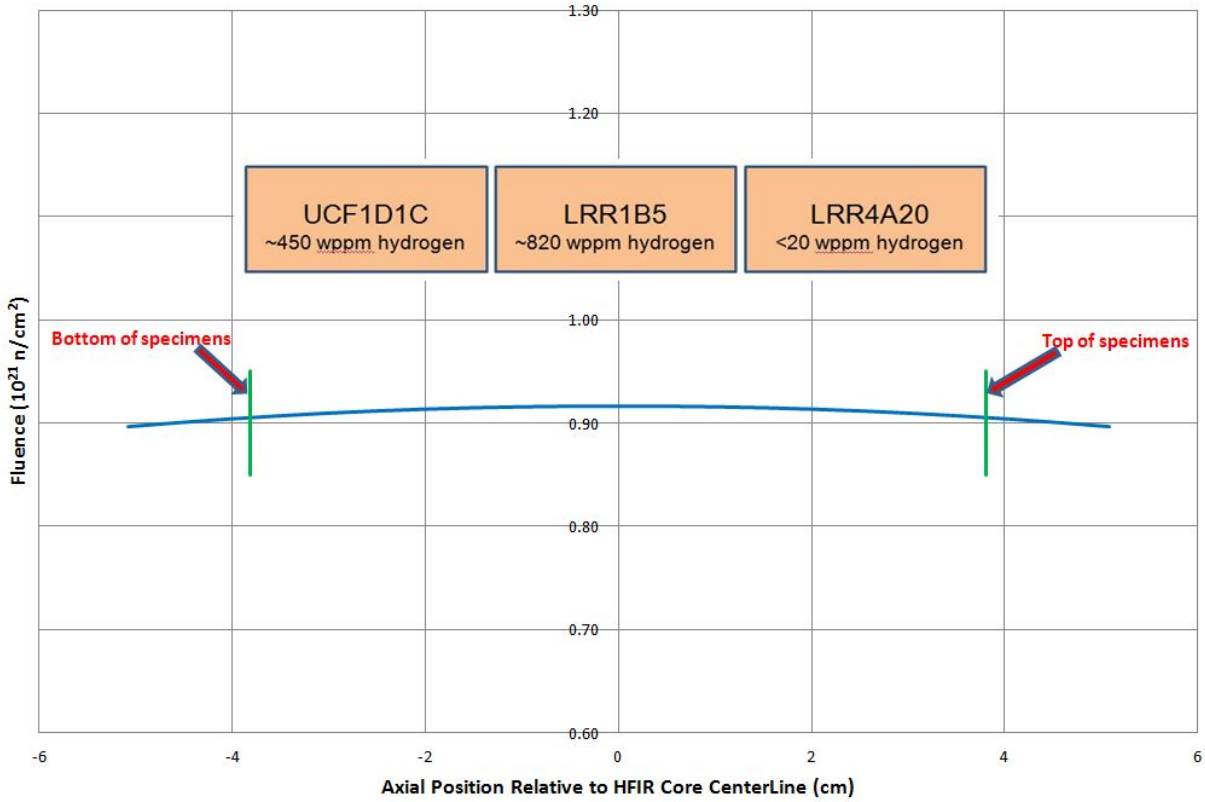

Figure 18. Fast fluence (>1.0 MeV) in the HYCD-1 specimens.

Table 5. HYCD-1 clad specimen fast fluences (>1.0 MeV)

Specimen ID	Neutron fluence (neutrons/cm^2)
LRR4A20	0.911e21 (±0.004)
LRR1B5	0.916e21 (±0.001)
UCF1D1C	0.911e21 (±0.004)

The fast fluence (>1.0 MeV) accumulated in the HYCD-2 specimens is shown in Figure 19 and tabulated in Table 6.

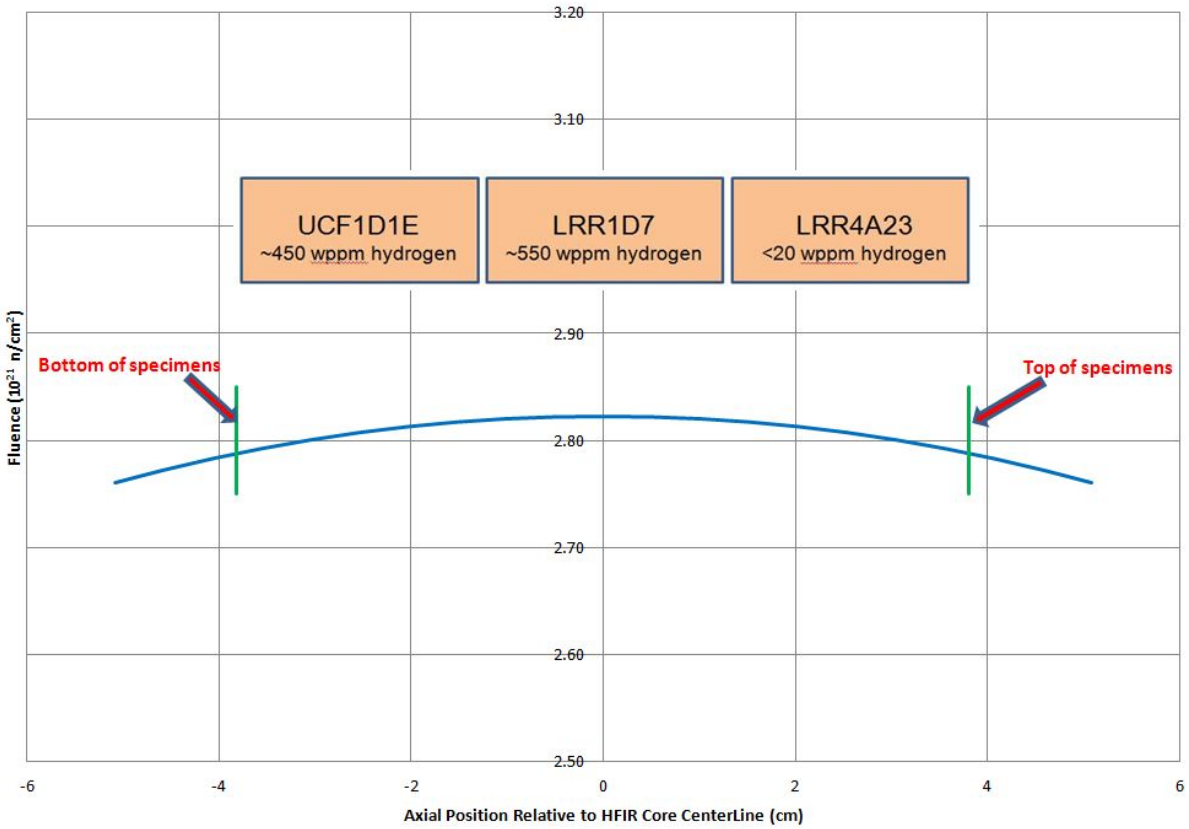

Figure 19. Fast fluence (>1.0 MeV) in the HYCD-2 specimens.

Table 6. HYCD-2 clad specimen fast fluences (>1.0 MeV)

Specimen ID	Neutron fluence (neutrons/cm^2)
LRR4A23	2.805e21 (±0.013)
LRR1D7	2.820e21 (±0.002)
UCF1D1E	2.805e21 (±0.013)

1.3.2.3 HYCD-1 and HYCD-2 Operating Temperatures

Since the capsules were not instrumented, the operating temperatures within the capsules are based on best-estimate simulations (design analysis and calculation [DAC], DAC-11-19-HYDRIDE01, February 2012, performed by R. Howard). A description of the ANSYS model and supporting DACs (fluid boundary conditions, component heat generation rates, materials of construction, finite-element model, etc.) were provided in *Neutron Irradiation of Hydrided Materials in HFIR-Summary of Initiial Activities FCRD-UFD-2013-000080*. These simulations provided the "best-estimate" operating inner and outer surface temperatures of the HYCD-1 and HYCD-2 specimens shown in Figure 20. The radial temperature

drop across the specimen(s) is illustrated in Figure 21. The temperatures and temperature drops experienced (calculated) for each of the specimens in HYCD-1 and HYCD-2 are tabulated in Table 7.

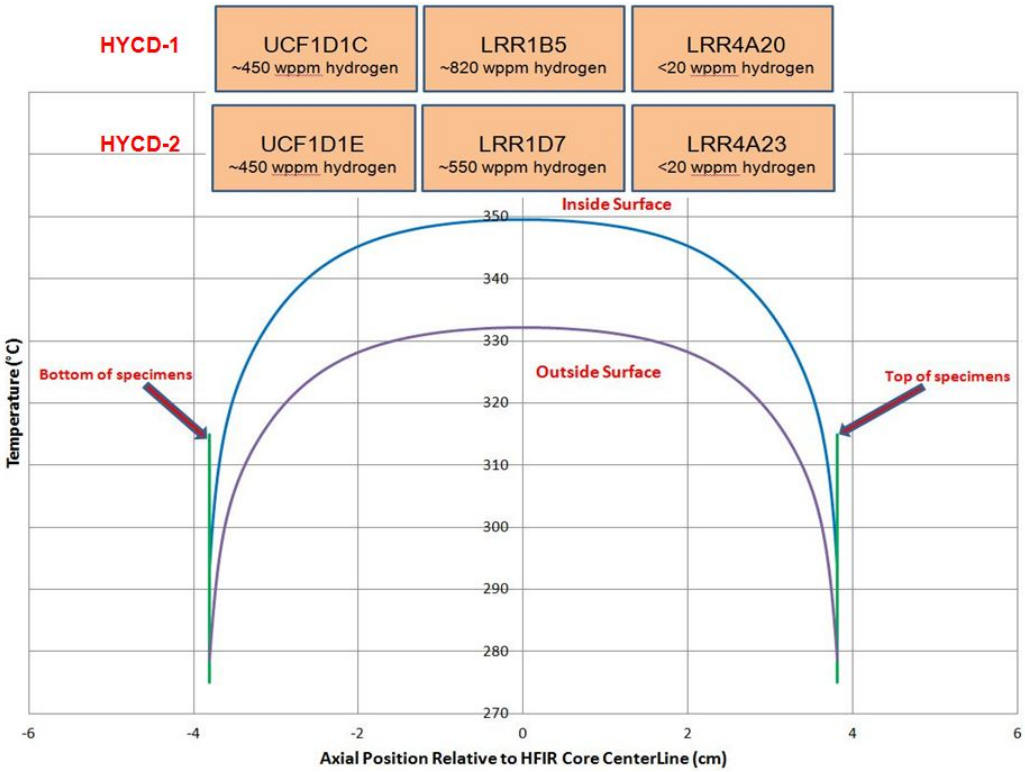

Figure 20. HFIR operating temperatures in the HYCD-1 and HYCD-2 specimens.

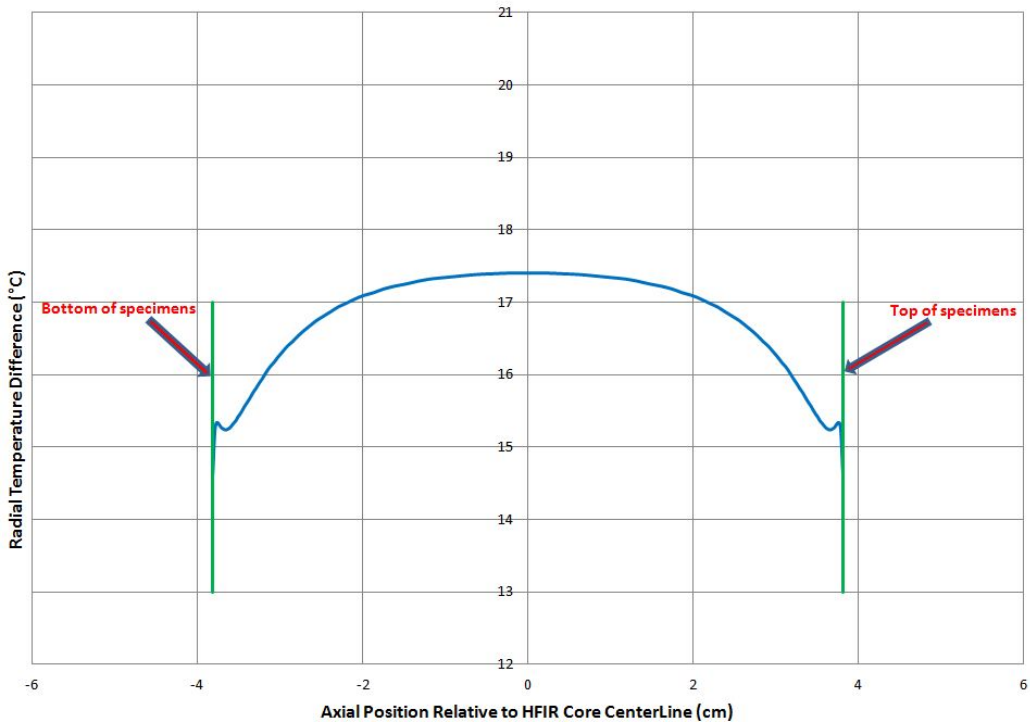

Figure 21. Operating radial temperature drop in the HYCD-1 and HYCD-2 specimens.

Table 7. Operating temperatures in the HYCD-1 and HYCD-2 clad specimen(s)

Position [cm] (relative to core centerline)	**-3.81 to -1.27**	**-1.27 to +1.27**	**+1.27 to +3.81**
HYCD-1			
Specimen ID	**UCF1D1C**	**LRR1B5**	**LRR4A20**
Avg. inner surface temperature (°C)	324.92	348.94	324.92
Inner surface temperature range (°C)	293.2 to 348.1	348.1 to 349.5	293.2 to 348.1
Avg. outer surface temperature (°C)	308.97	331.57	308.97
Outer surface temperature range (°C)	278.6 to 330.8	330.8 to 332.1	278.6 to 330.8
Avg. temperature drop across specimen (°C)	15.95	17.37	15.95
ΔT range (°C)	14.60 to 17.31	17.31 to 17.41	14.60 to 17.31
HYCD-2			
Specimen ID	**UCF1D1E**	**LRR1D7**	**LRR4A23**
Avg. inner surface temperature (°C)	324.92	348.94	324.92
Inner surface temperature range (°C)	293.2 to 348.1	348.1 to 349.5	293.2 to 348.1
Avg. outer surface temperature (°C)	308.97	331.57	308.97
Outer surface temperature range (°C)	278.6 to 330.8	330.8 to 332.1	278.6 to 330.8
Avg. temperature drop across specimen (°C)	15.95	17.37	15.95
ΔT range (°C)	14.60 to 17.31	17.31 to 17.41	14.60 to 17.31

There are significant axial temperature gradients in the top and bottom 1 in. (2.54 cm) clad specimens in both HYCD-1 and HYCD-2 (there is very low variation in the middle specimen). There are three primary reasons for these axial temperature gradients: (1) the structural gamma heating is at its maximum at the core centerline and decreases with increasing distance from the core centerline; (2) the structural gamma heating is greater for molybdenum (~43.3 W/g [centerline]) than the Zircaloy clad specimen (~38.5 W/g) and the aluminum spacers (~32.5 W/g); and (3) the thermal conductivity of aluminum is greater than that of the molybdenum and Zircaloy. Thus, not only does the total power generated decrease (away from the core centerline) but heat is also being conducted axially from the molybdenum heater to the colder aluminum spacers. These axially temperature variations are most acute in the smaller 3 in. (7.62 cm) capsules (HYCD-1 and HYCD-2); there will be gradients in the larger 6 in. (15.24 cm) capsules (HYCD-3), but the variation seen here would be confined to the top and bottom ~2 cm of the cladding specimens.

1.4 Preliminary PIE Results of Irradiated Specimens HYCD-1 and HYCD-2

1.4.1 Visual Examination of HYCD-1 and HYCD-2

After removal from the reactor, the HYCD-1 and HYCD-2 capsules were shipped to the Irradiated Fuel Examination Lab (IFEL) in a loop cask (Figure 22) for PIE. The cask arrived at the IFEL from the HFIR on November 6, 2012, approximately 4 months after HYCD-2 was removed from the HFIR reactor core. The two capsules were removed from the shipping cask and were loaded into the hot cell in January 2013 (Figure 23 and 24). They were identified by the labeling engraved on the capsule shroud tube as HYCD-1 and HYCD-2. The capsules appeared to be in good condition, and no unusual features were noted.

Figure 22. Loop cask for HYCD-1 and HYCD-2 (OD × L =2 ft × 8 ft) at the IFEL.

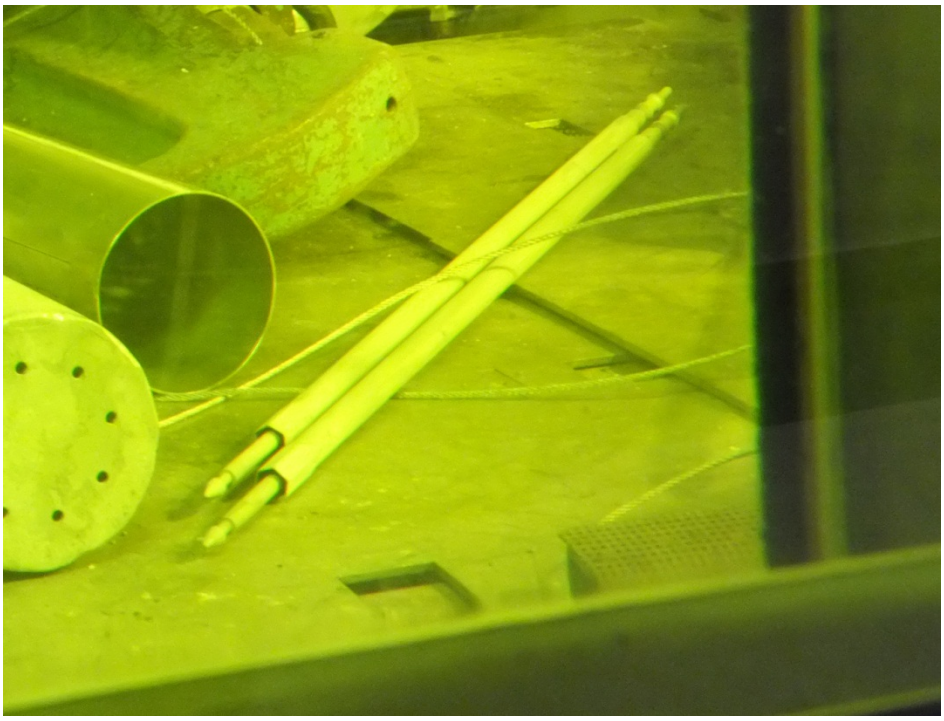

Figure 23. HYCD-1 and HYCD-2 capsules in the North Cell of Building 3525.

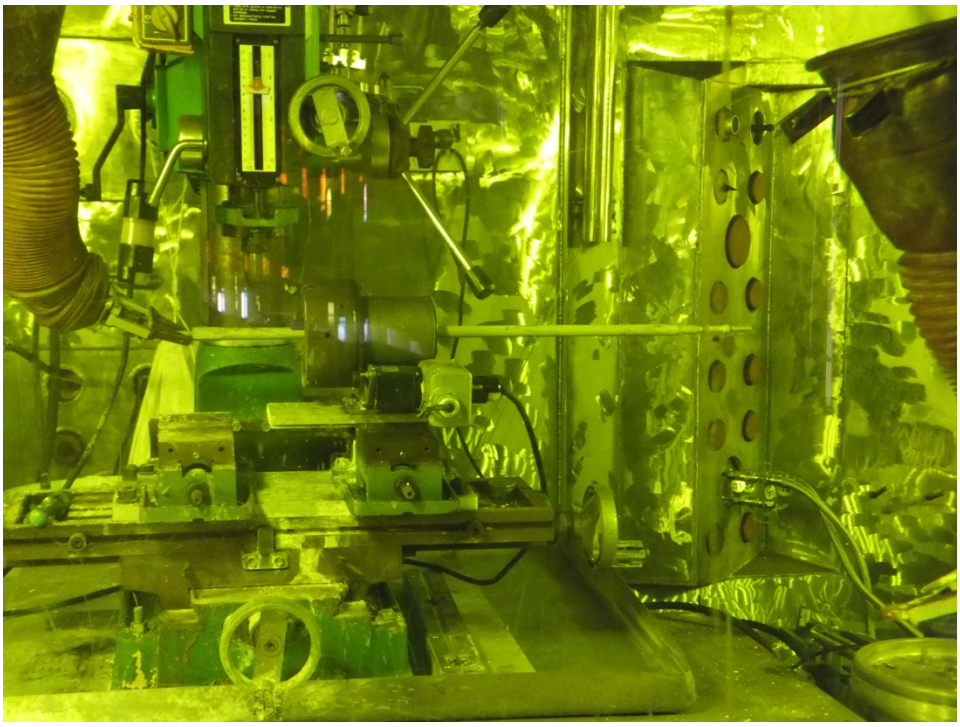

Figure 24. In-cell milling to remove the cladding specimen from the capsule.

Hydrided specimens were removed from the capsules by milling out the shroud and aluminum target containment at a location 4 in. from the marked feature towards the capsule centerline (Figure 25), removing the aluminum spacers, and pushing out the cladding specimen from the molybdenum heater rod (Figures 26 and 27). The HYCD-1 specimens were removed rather easily. The HYCD-2 samples proved to be more difficult to remove, and a significant amount of force was needed to remove cladding specimens UFC1D1E and LRR1D7 from the molybdenum heater rod. It should be noted that these cladding specimens may have been damaged during this removal process. Figure 28 and Figure 29 show the specimens after they were removed from HYCD-1 and HYCD-2, respectively. Figure 30 is a high-magnification image of Specimen UCF1D1E, which shows some unusual features near the middle of the cladding sample.

Target Capsule without shroud

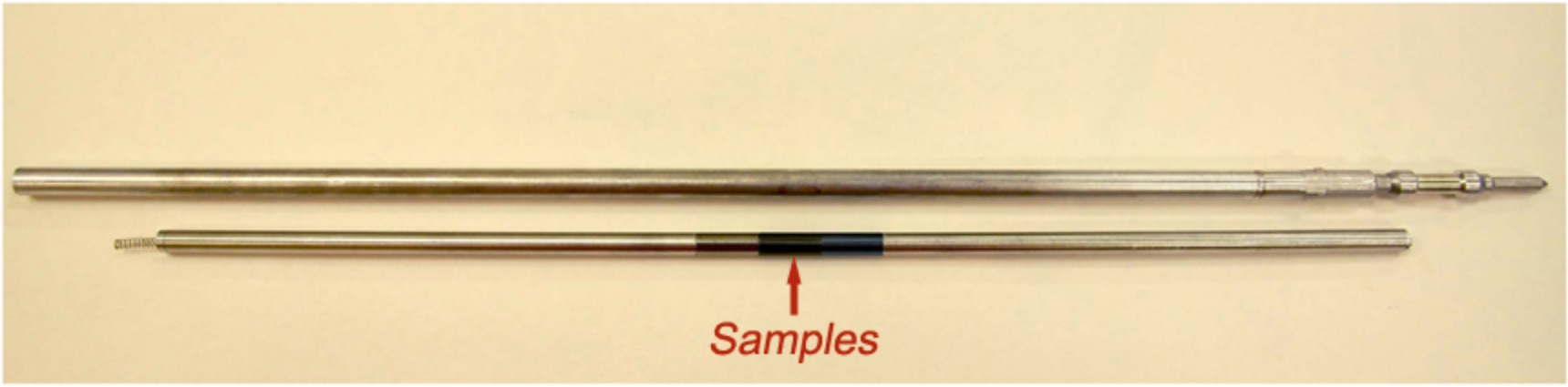

Target Capsule (without top cap) and internal components (3 in sample)

Figure 25. Illustration of removing the cladding specimens from the capsule.

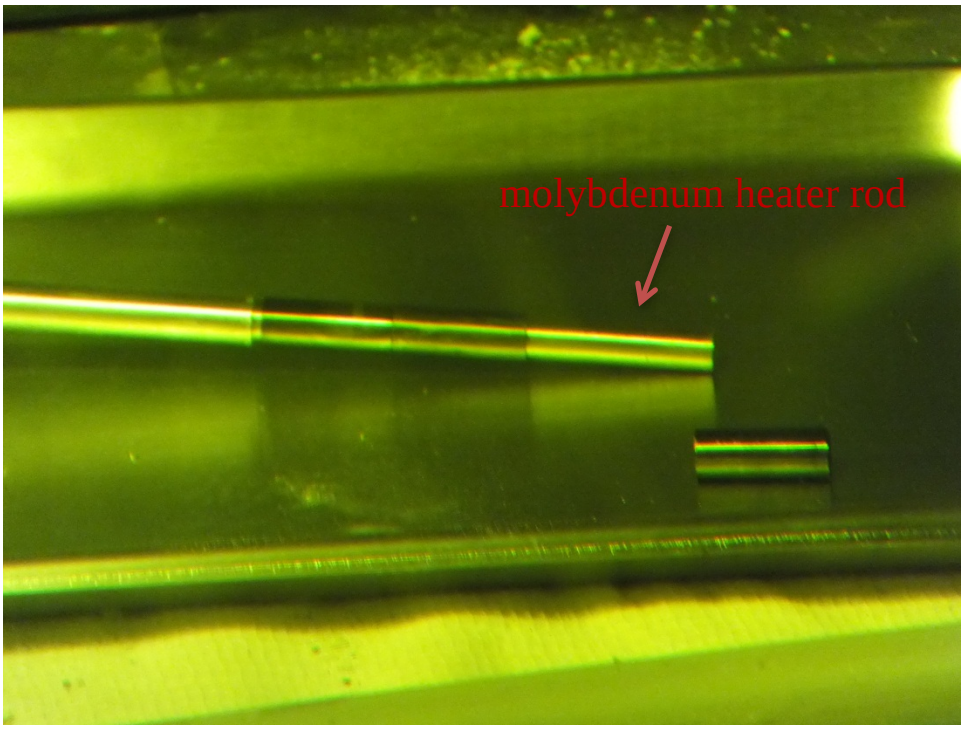

Figure 26. HYCD-1 samples on molybdenum heater rod.

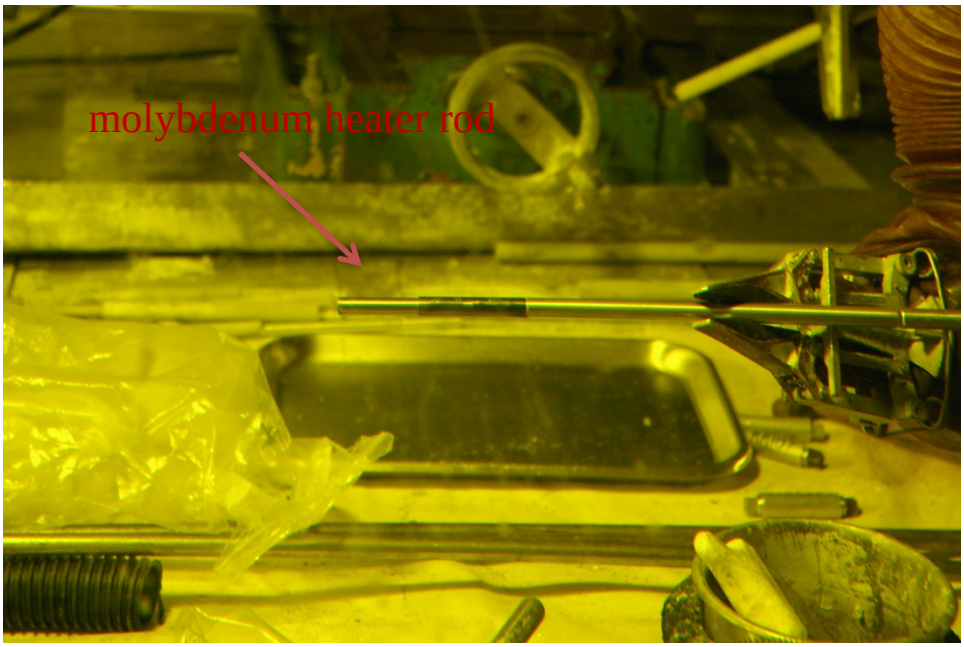

Figure 27. HYCD-2 samples on molybdenum heater rod.

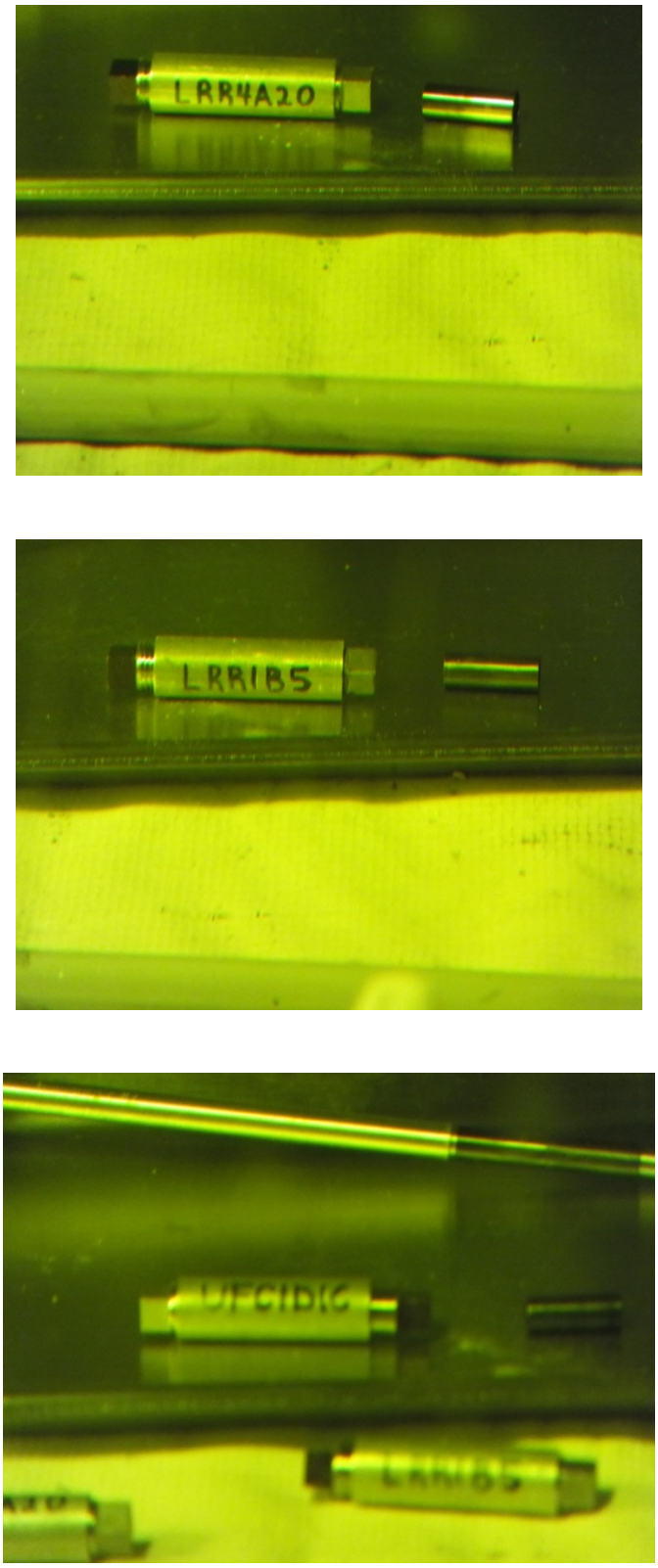

Figure 28. Specimens removed from HYCD-1.

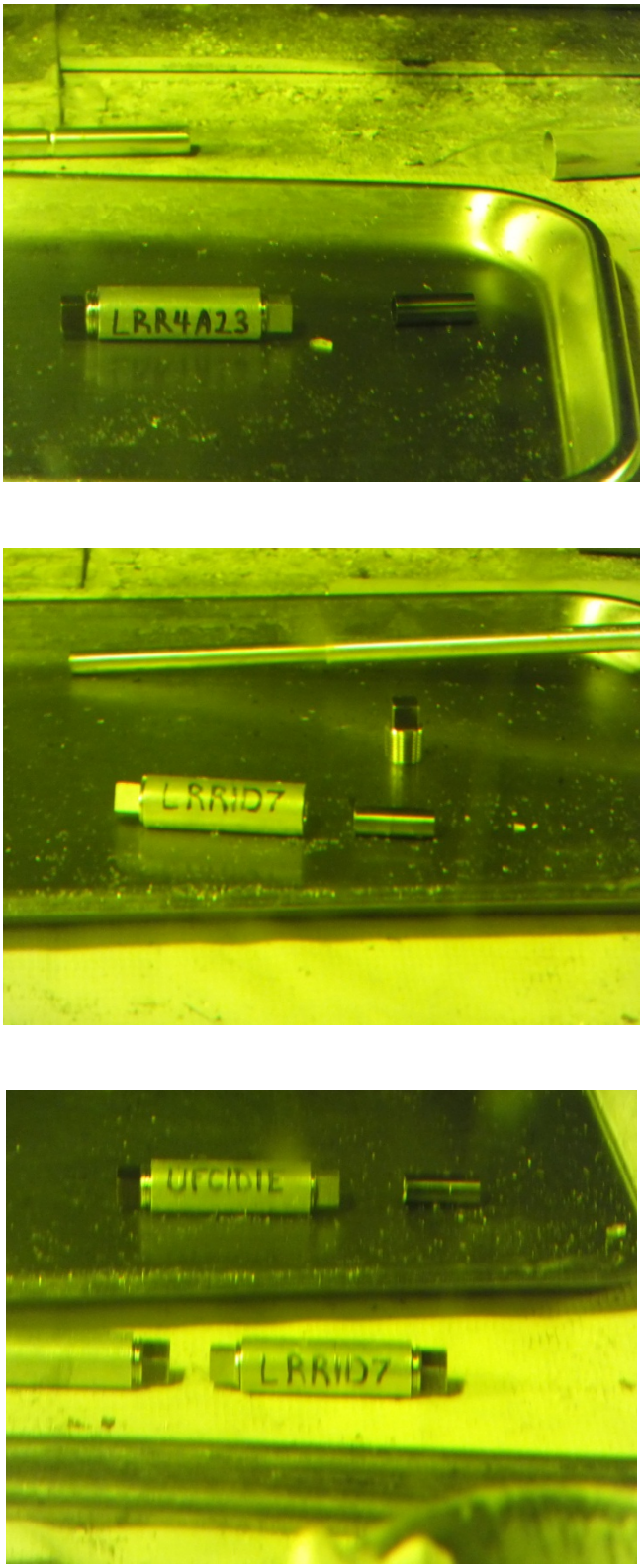

Figure 29. Specimens removed from HYCD-2.

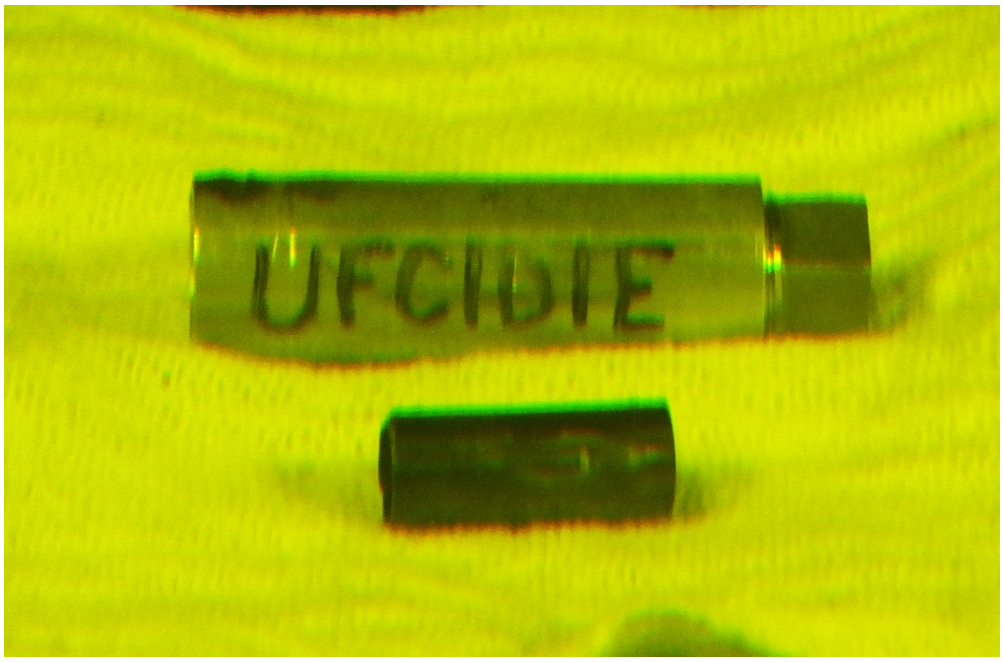

Figure 30. High magnification image of Specimen UFC1D1E.

1.4.2 Dose Rate Measurements

Dose rates of the HYCD-1 and HYCD-2 specimens were measured at 1 in. and 12 in., as illustrated in Figure 31. The detector used for the measurement is a Thmers Eberline RO20 Ion Chamber. For each capsule, a 1-in.-long specimen was selected. Table 8 summarized the measured dose rates. An ORNL Radiological Survey report in support of dose rating for these two HYCD-1 and HYCD-2 specimens is attached in Appendix A.

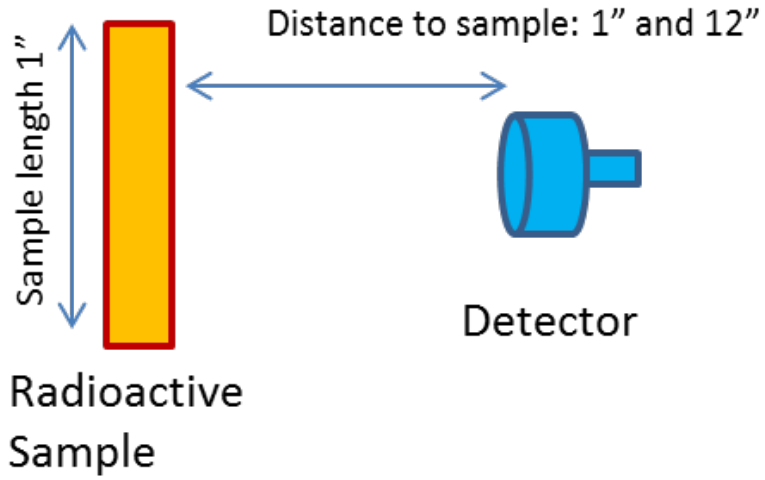

Figure 31. Schematic illustration of the dose rate measurement on HYCD-1 and HYCD-2.

Table 8. Dose rates on the HYCD-1 and HYCD-2 specimens

Capsule ID	HYCD-1	HYCD-2
Sample ID	UFC1D1C	LRR1D7
Cycle(s) in HFIR	1	3
Sample length	25.4 mm	25.4 mm
Wall thickness	0.57 mm	0.57 mm
Materials	Zircaloy-4	Zircaloy-4
Hydrogen content	≈450 wppm	≈550 wppm
Date removed from reactor	4/19/2012 - 5/7/2012	7/13/2012 – 7/31/2012
Date measured	2/18/2013	2/18/2013
Dose rate[a] at 1 cm	**20 R/h**	**40 R/h**
Dose rate[a] at 30 cm	**1 R/h**	**4 R/h**

[a]Background dose rate was approximately 35 mR/h.

1.4.3 Optical Metallographic Examination

Sample UFC1D1C was selected from HYCD-1 capsule and LRR1D7 from HYCD-2 for microstructural examinations. Both samples were 1 in. long and were sectioned by a diamond saw (Figure 32) in the hot cell into five shorter rings, as shown in Figures 33 and 34. Two optical metallographic (MET) mounts, as listed in

Table 9, were prepared by mounting the cut specimens (the middle rings shown in Figs. 33 and 34) with epoxy in a phenolic base mount.

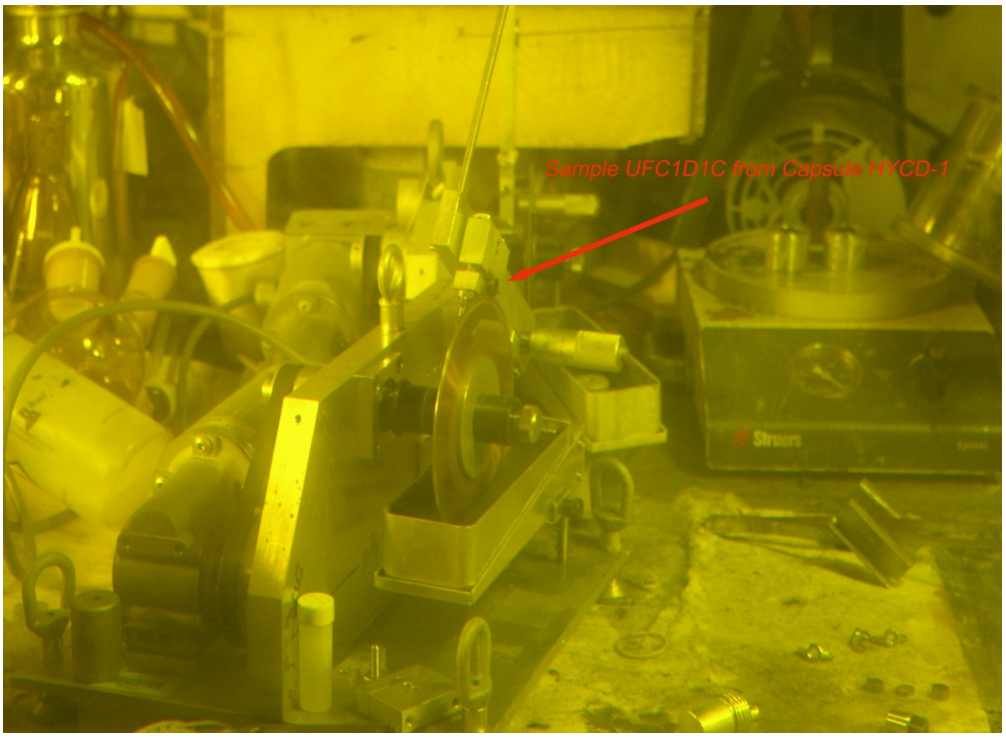

Figure 32. A diamond saw for radioactive sample sectioning in hot cell.

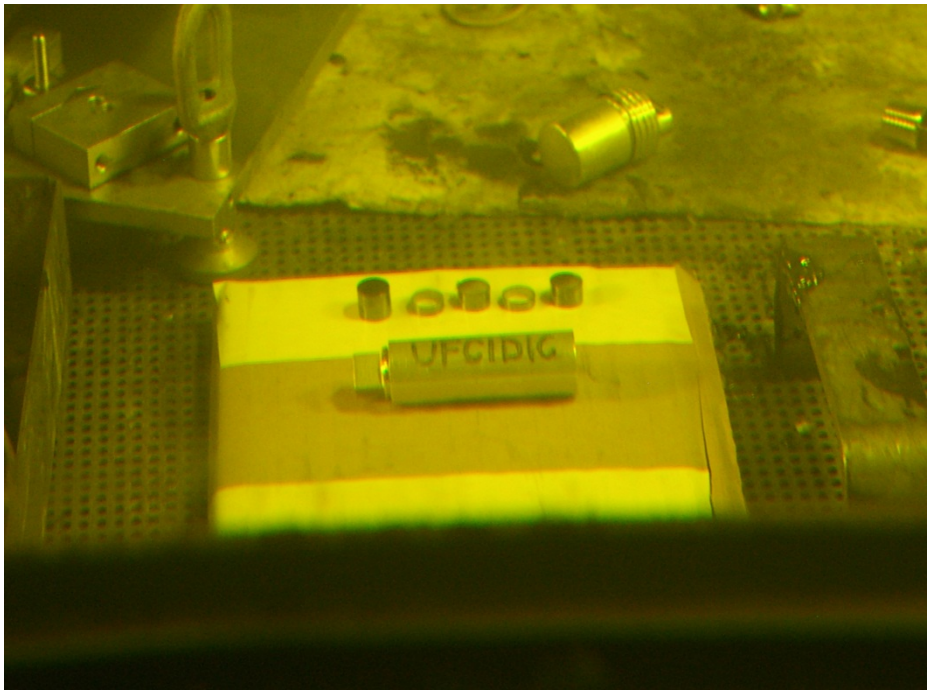

Figure 33. Five rings sectioned from Sample UFC1D1C, Capsule HYCD-1.

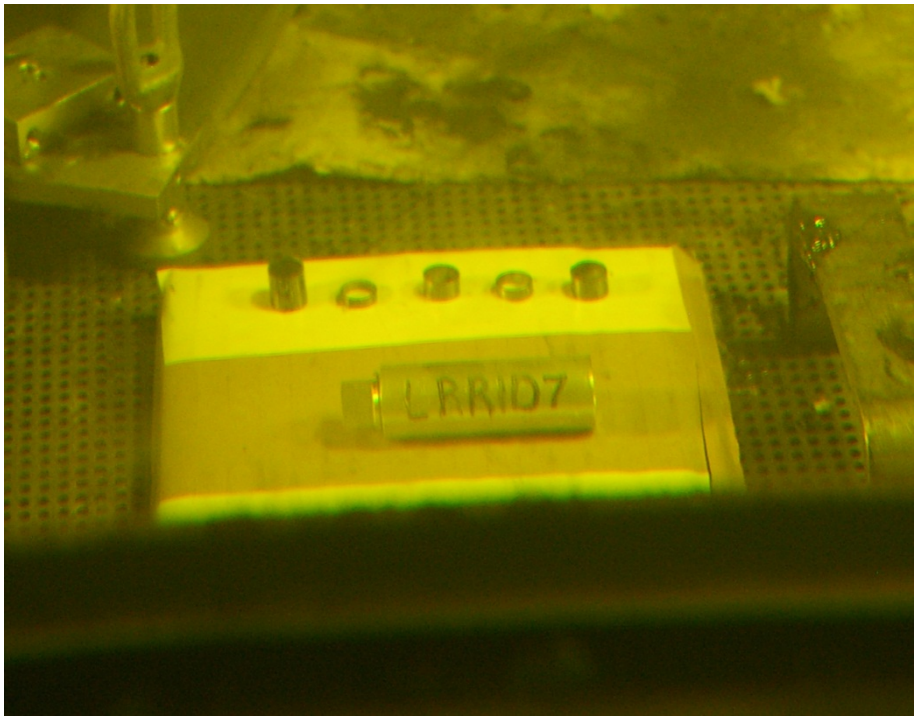

Figure 34. Five rings sectioned from Sample LRR1D7, Capsule HYCD-2.

Table 9. Summary of the MET mounts for optical metallographic examination

MET mount ID	6376	6377
Capsule ID	HYCD-1	HYCD-2
Sample sectioned	UFC1D1C	LRR1D7
Cycle(s) in HFIR	1	3
Wall thickness	0.57 mm	0.57 mm
Materials	Zircaloy-4	Zircaloy-4
Hydrogen content	≈450 wppm	≈550 wppm
Comments		2 cracks observed

These mounts were then ground flat and polished. After a final cleaning they were photographed using a commercial metallographic microscope, and the images were assembled into a final collage (Figure 35 and Figure 36). No unusual behavior was noted for Sample 6376. However, two through-wall cracks were observed for Sample 6377 (Figure 37). As the MET mount was prepared using the same process for the both samples, it is unlikely the cracks were introduced during the sample preparation. It appears that the damage to Sample 6377 was caused when the sample was removed from the HYCD-2 molybdenum heater rod. A capsule design change is under consideration to avoid this type of problem in the future.

Optical microscopy with as-polished MET mounts samples did not clearly indicate the hydride morphology. Metallographic examinations of the etched samples are under way and will be reported in the near future.

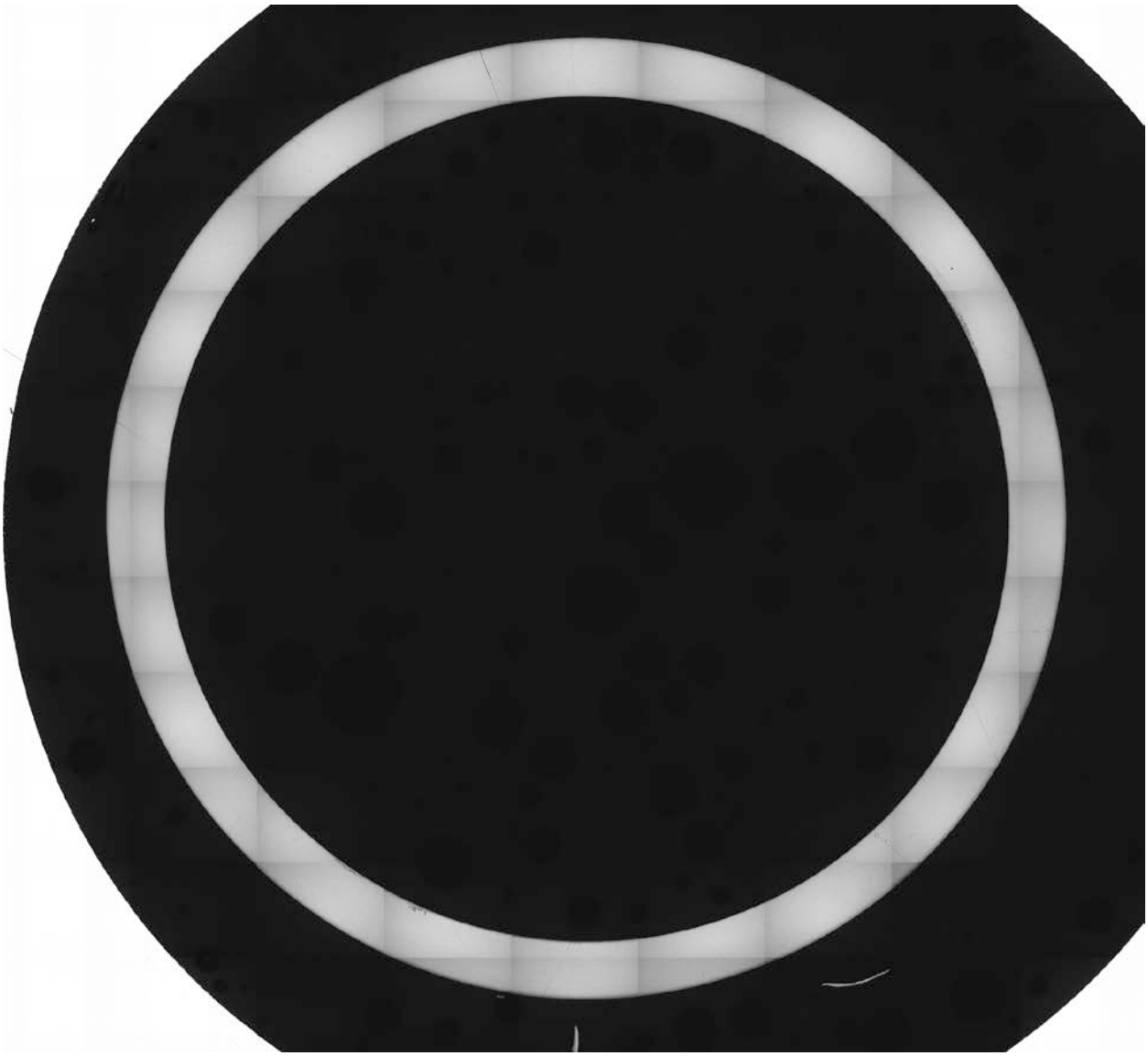

Figure 35. Mount 6376, prepared from Sample UFC1D1C of Capsule HYCD-1. No unusual behavior was noted.

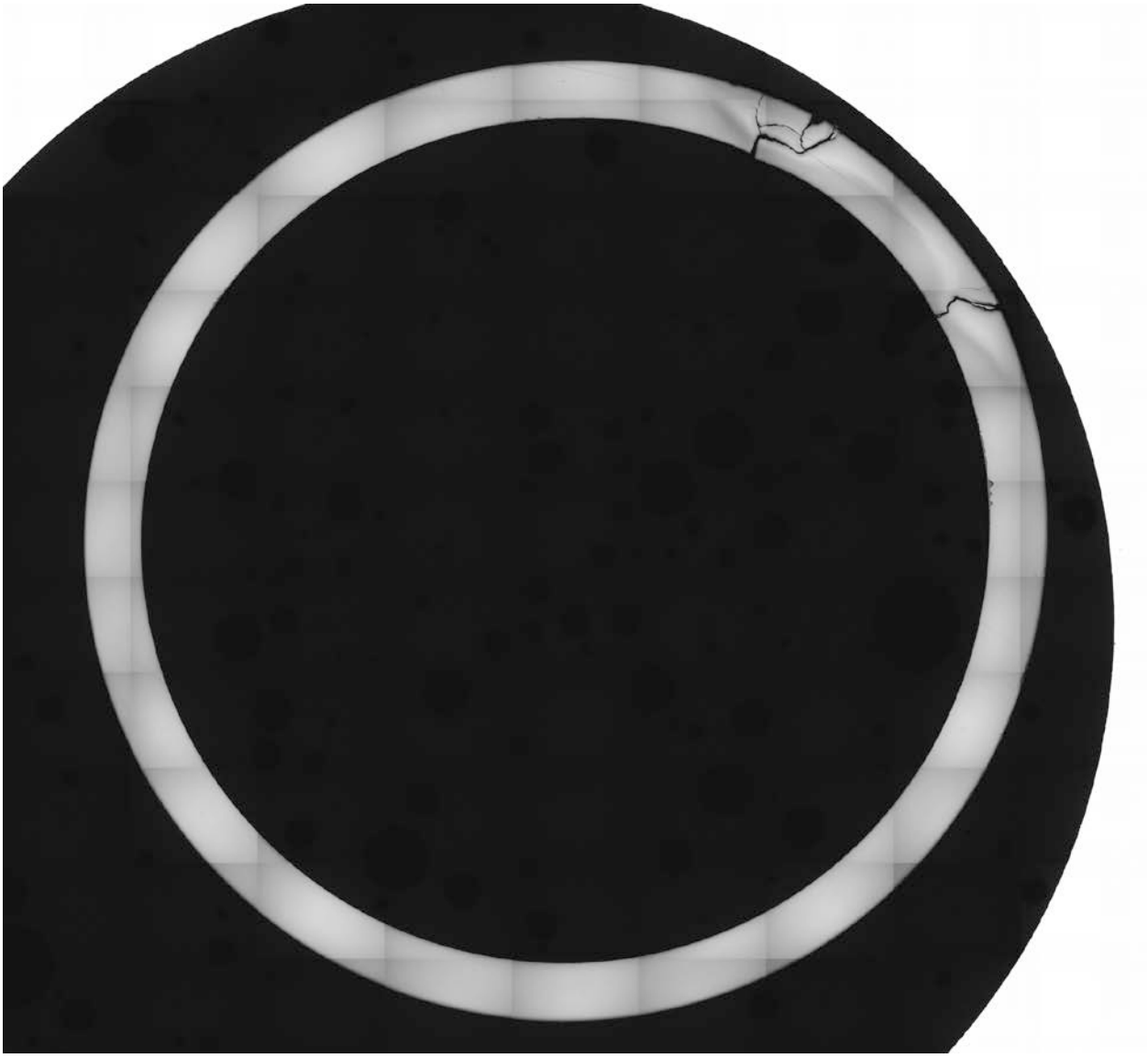

Figure 36. Mount 6377, prepared from Sample LRR1D7 of Capsule HYCD-2. Two through-wall cracks were observed.

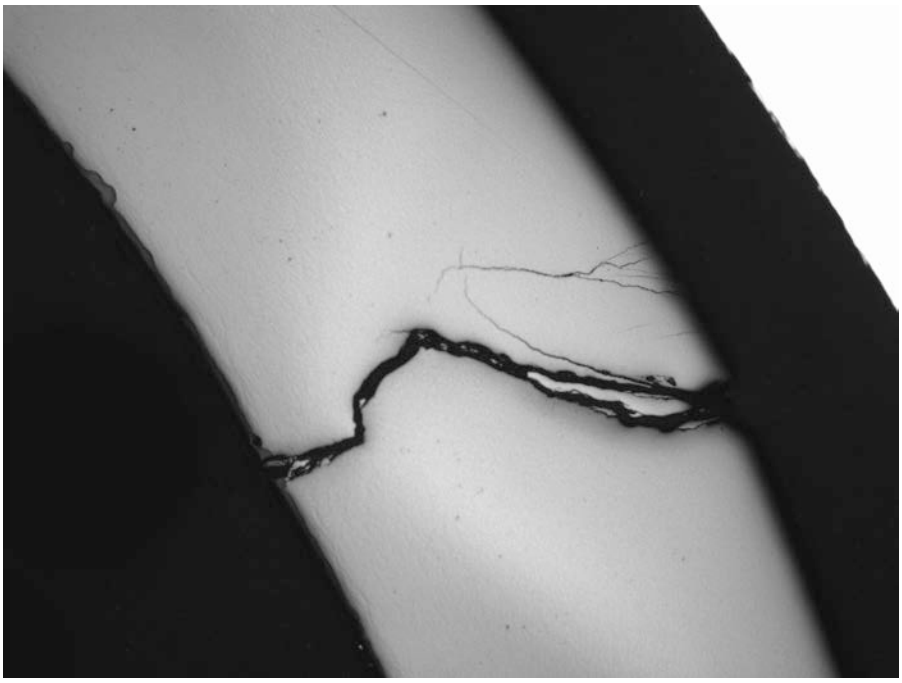

(a)

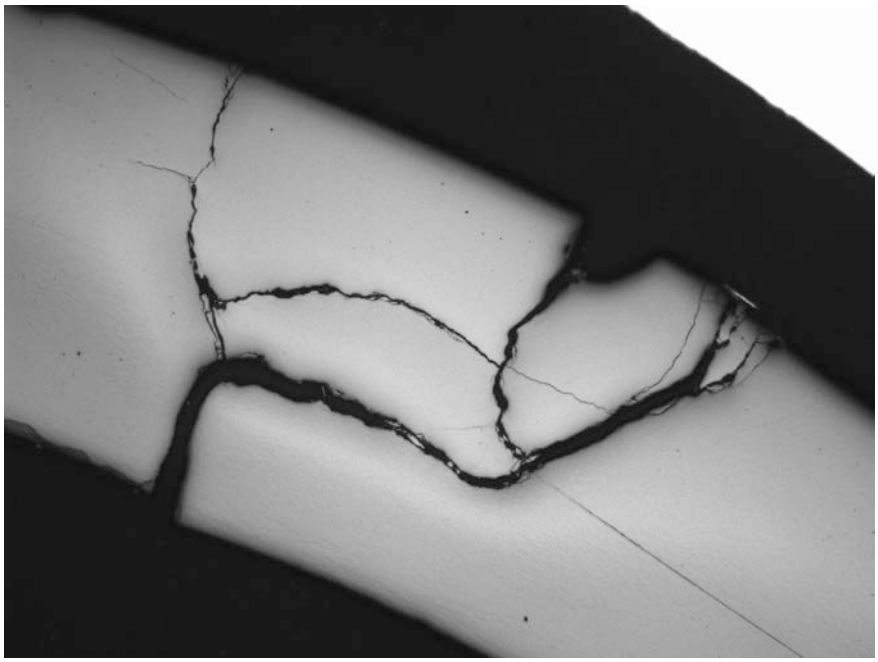

(b)

Figure 37. High-magnification images of the two cracks observed in Figure 36.

1.4.4 Outer Diameter Measurements

Outer diameter (OD) measurements were conducted with a measurement sensor (Figure 38), remotely operated in the main hot cell in the IFEL for Specimens LRR4A20 and LRR1B5 from HYCD-1 and for Specimens LRR4A24 and UFC1D1E from HYCD-2. Prior to beginning the measurement, the system was verified with a pin gauge standard, nominally 0.2450 in. (Figure 39). As shown in Figure 40, the measure sensor can record the OD value up to 0.00001 in.

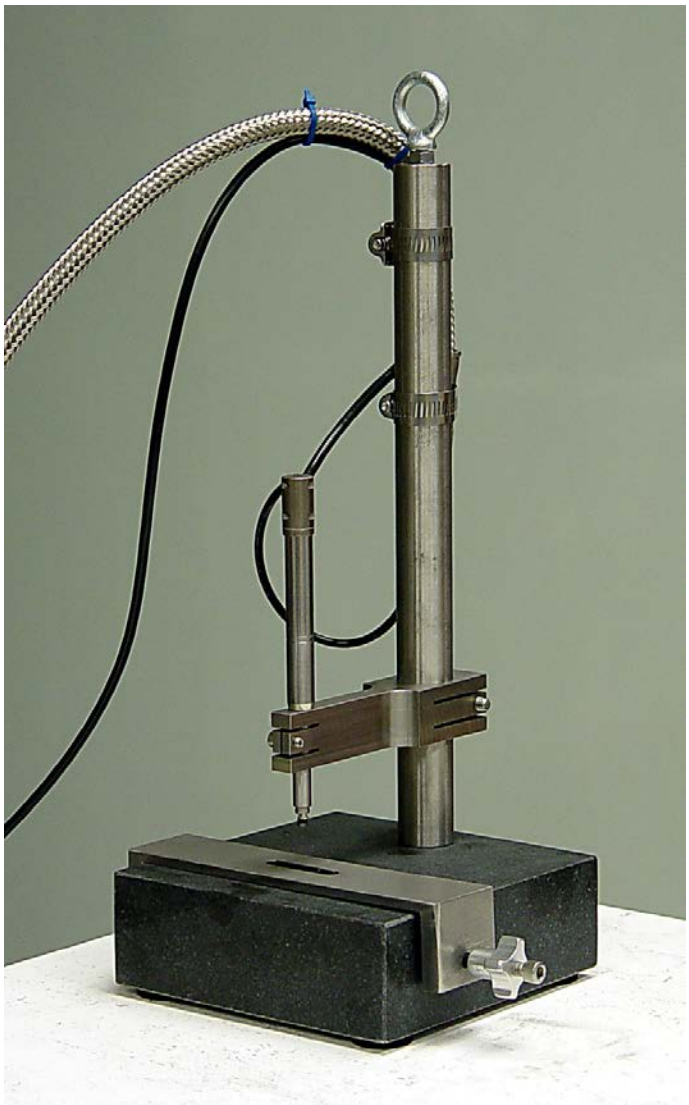

Figure 38. Measurement sensor.

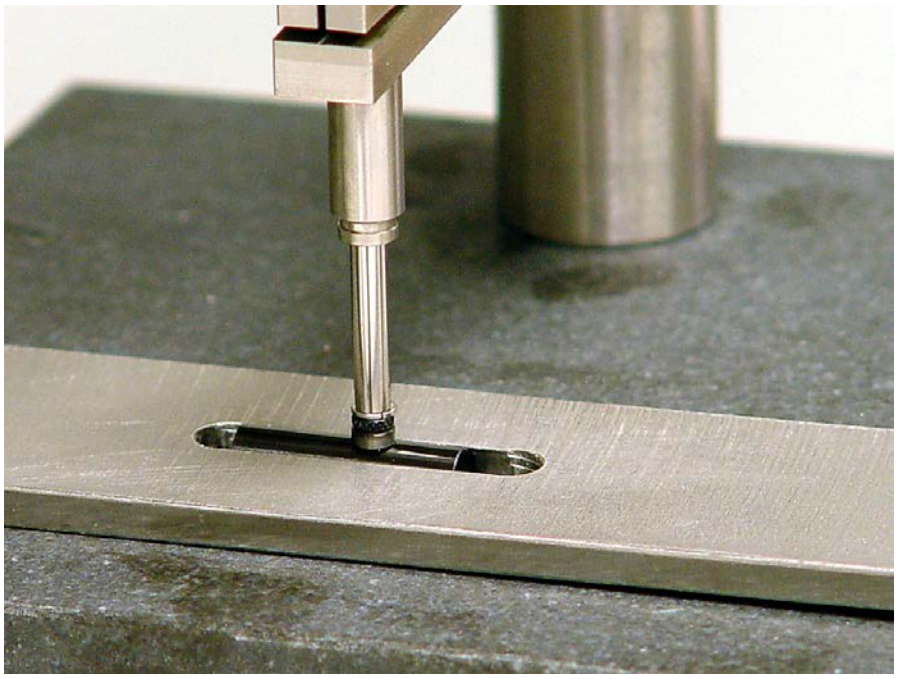

Figure 39. Measurement probe contacting pin gauge (black item in slot).

Figure 40. Display of the measure sensor.

The measurements indicated that the OD of the high hydrogen content irradiated samples (LRR1B5 from HYCD1 and UFC1D1E from HYCD-2) is slightly increased, compared to the nominal OD of the

unirradiated samples (Table 10). However, the OD of the low hydrogen content irradiated samples (LRR4A20 from HYCD-1 and LRR4A23 from HYCD-2) almost remained the same as the unirradiated samples. Tables 11 and 12 summarize the measured OD results for HYCD-1 and HYCD-2 specimens, respectively.

Table 10. Outer diameter measurement for as-fabricated and hydrided samples before the HFIR irradiation

Specimen ID	As-received, LRR4A27	Hydrided, UFC1D1A
1st measurement at 0°, in.	0.3730	0.3725
2nd measurement at 0°, in.	0.3730	0.3720
1st measurement at 90°, in.	0.3730	0.3725
2nd measurement at 90°, in.	0.3730	0.3725
Average	**0.3730**	**0.3724**

Table 11. Outer diameter measurement of the specimens from Capsule HYCD-1

Specimen ID	Irradiated LRR4A20	Hydrided and irradiated LRR1B5
1st measurement at 0°, in.	0.37346	0.37532
2nd measurement at 0°, in.	0.37340	0.37524
1st measurement at 90°, in.	0.37356	0.37578
2nd measurement at 90°, in.	0.37352	0.37524
Average	**0.37349**	**0.37540**

Table 12. Outer diameter measurement of the specimens from Capsule HYCD-2

Specimen ID	Irradiated LRR4A23	Hydrided and irradiated UFC1D1E
1st measurement at 0°, in.	0.37324	0.37566
2nd measurement at 0°, in.	0.37436	0.37544
1st measurement at 90°, in.	0.37394	0.37530
2nd measurement at 90°, in.	0.37394	0.37534
Average	**0.37387**	**0.37544**

2. THE DEVELOPMENT OF A REVERSAL BENDING FATIGUE TESTER FOR SPENT FUEL VIBRATION INTEGRITY INVESTIGATION

1.5 Introduction

Under current US Nuclear Regulatory Commission rules, it is not sufficient for used nuclear fuel (UNF) to simply maintain its integrity during the storage period. It must maintain its integrity in such a way that it can withstand the physical forces of handling and transportation associated with restaging the fuel and moving it to treatment or recycling facilities, or to a geologic repository or other storage facility. Hence it is necessary to understand the performance characteristics of aged UNF cladding and the UNF pellets it surrounds under loadings stemming from transport initiatives. For normal conditions of transport, vibration loads incident to transport must be considered. As the burnup of the fuel increases, a number of changes occur that may affect the performance of the fuel and cladding in storage and during transportation. Spent fuel cladding has traditionally provided defense-in-depth as the primary fission product barrier in the nuclear fuel cycle, and has been relied upon to provide geometry control for criticality safety during transportation. The mechanical properties of high-burnup de-fueled cladding have been previously studied by subjecting defueled cladding tubes to longitudinal (axial) tensile tests, ring-stretch tests, ring-compression tests, and biaxial tube burst tests. The objective of the bend test development is to investigate the mechanical properties and behavior of both the cladding and the fuel in the cladding (including inertia-induced fuel pellet and clad interaction) under vibration/cyclic loads similar to the sustained vibration loads experienced during normal transport.

The vibration loads experienced by UNF rods during transportation can be characterized by dynamic, cyclic, bending loads. The transient vibration signals in a specified transport environment can be analyzed, and frequency, amplitude, and phase components of the vibration can be identified. The methodology being developed at ORNL is a novel approach to support the study of the vibration integrity of actual UNF rod segments through the testing and evaluation of the fatigue performance of UNF rods at defined frequencies and loads. ORNL has developed a fatigue system to evaluate the response of the UNF rods to vibration loads, as noted in Refs. 7, 8, 9 and 10. A three-point deflection measurement technique using linear variable differential transformers (LVDTs) is used to characterize the rod curvature of samples under test conditions, and electromagnetic force linear motors are used as the driving system to provide the mechanical load. ORNL plans to use the test system in a hot cell to perform UNF vibration testing on high-burnup fuel to evaluate the effect of pellet-clad interaction and the effects of material bonding on the effective lifetime of the fuel-clad structure bending fatigue performance.

1.6 Test System Concept

The reversal pure bending is conducted using a U-frame testing setup. A conceptual U-frame setup is shown in Figure 41. The U-frame is constructed with two rigid arms and the associated linking members. The rod specimen is coupled with the U-frame by inserting it into the co-linear holes within the two rigid arms. As a result, reversal bending will be applied to the rod specimen when a controlled push-pull force is applied to the two loading points of the rigid arms. This test system is able to capture the pure reversal bending as desired and, at the same time, must be implemented in a hot cell (use of remote handling and operations). To facilitate this, the system should have a minimal number of moving parts, and test sample installation can be achieved using a simple drop-in action. The test system is designed to use a 6 in. rod segment with a 2 in. gage section. The majority of the test system components are made of stainless steel (SS) 304. Prior to initial equipment design, 3-D finite-element analysis (FEA) showed that the position of

the rod specimen relative to the linking member of the U-frame has a significant impact on the amount of stress applied to the specimen. Using appropriate compliant layers allows a pure bending moment to be achieved in the gage section, as shown in Figure 42. The maximum von Mises stress level occurs at the pellet-clad interface.

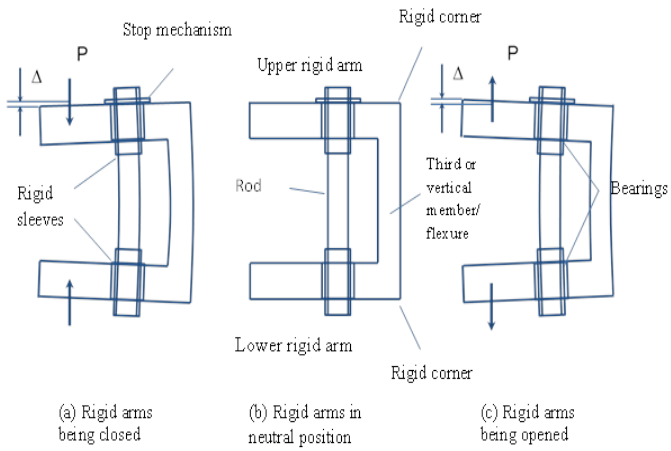

Figure 41. U-frame-assisted bending fatigue testing setup for reversal bending when rigid arms are (a) closing, (b) neutral, and (c) opening.

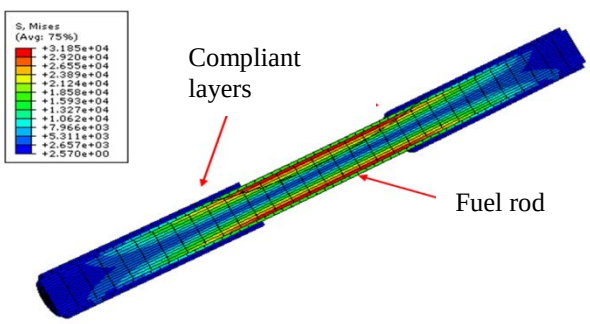

Figure 42. Stress distribution in a fuel rod with compliant layer when the applied force was 178 N; the unit of stress is psi. The maximum von Mises stress is 220 MPa (3.185×104 psi).

1.7 Test System Development and Status

The design and prototype fabrication and evaluation of the test setup have been a multi-year project sponsored by the Nuclear Regulatory Commission and is documented in References (6–9)

The current configuration of the bend test apparatus has the U-frame set horizontally and uses a dual Bose linear motor test bench (Figure 43). This alignment eliminates the effect of the U-frame self-weight entirely; also the push-pull force is applied symmetrically at both loading points by use of the dual linear motors. This design allows the use of a wide frequency range when applying pure bending to the test specimen during dynamic cycling. Moreover, the Bose linear motors use electromagnetic forces to

generate the driving forces, and thus there are no oil issues as would occur when using a servo-hydraulic test machine.

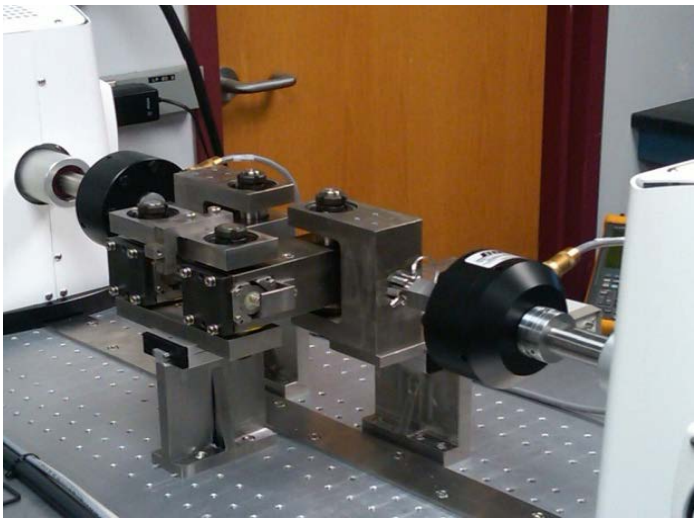

Figure 43. Integrated ORNL U-frame Bose dual linear motor test bench. A horizontal arrangement is used to eliminate the effect of the U-frame mass on the specimen.

This configuration is in the final stages of evaluation and was moved into the hot cell (ORNL Building 3525) at the end of September 2013 to conduct the bend tests sponsored by the NRC. Once the NRC-sponsored tests are complete, the apparatus will be transitioned and made available for Used Fuel Disposition Campaign directed bend tests.

1.8 Development of Measurement Methods

LVDTs are generally reliable for measuring deformations and have been selected for use in the bend tests conducted in the hot cell. However, this measurement method presents challenges to collecting accurate bending data because both the deformation of the compliant layers and the rigid body motion of the test frame contribute to the measured results. A three-point measurement system has been developed to accurately capture the deformation of the rod specimen during testing. The three-point measurement system involves using three LVDTs spaced along the test specimen to accurately measure the deflection over a wide area of the specimen. The three LVDTs are assembled into a single sensor clamp and are mounted to the side connecting plates. The total curvature of the specimen can be deduced from the LVDT measurements, and this information can be used to characterize the true deformation of the specimen. The deformation information collected using this measurement system is relatively independent of the compliant layers and rigid body motion of the U-frame system. The three-point measurement method is shown in Figure 44.

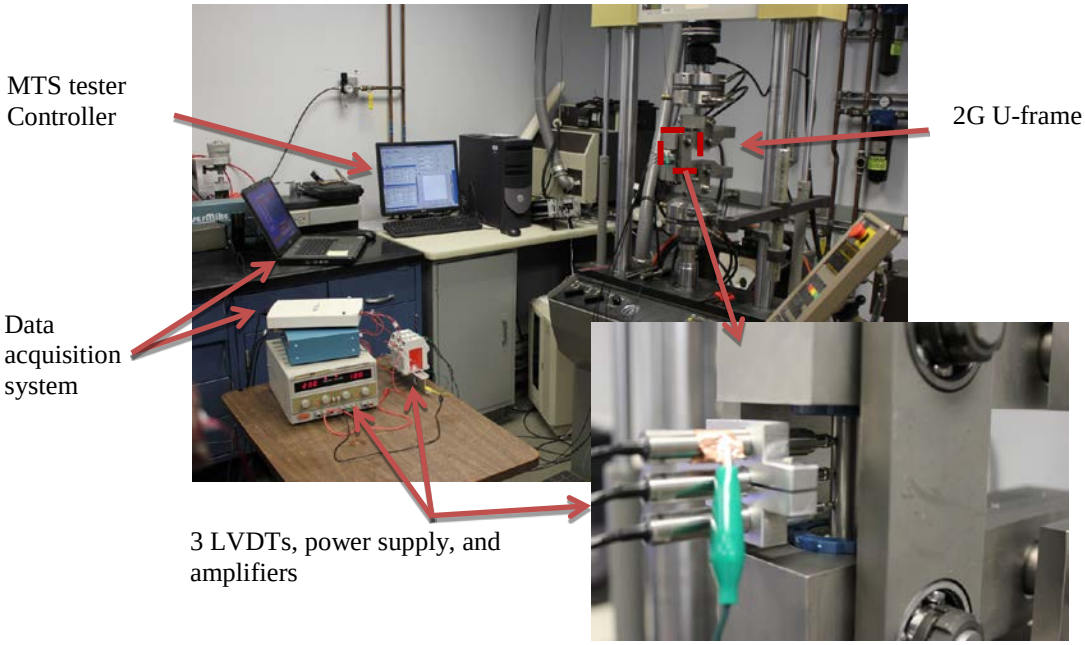

Figure 44. Three-point measurement method for the curvature of specimen through three LVDTs. The demonstration is on the U-frame setup equipped with linear roller bearings and integrated onto a MTS 810 servo-hydraulic test machine.

The use of curvature along with the bending moment enables the rod specimen to be tested and characterized more appropriately than using a single point deflection measurement, substantially reducing the uncertainty. The curvature obtained using a surrogate rod made of SS tube is given in Figure 45. It can be clearly seen that in a force control mode, the waveform of curvature followed that of the moment.

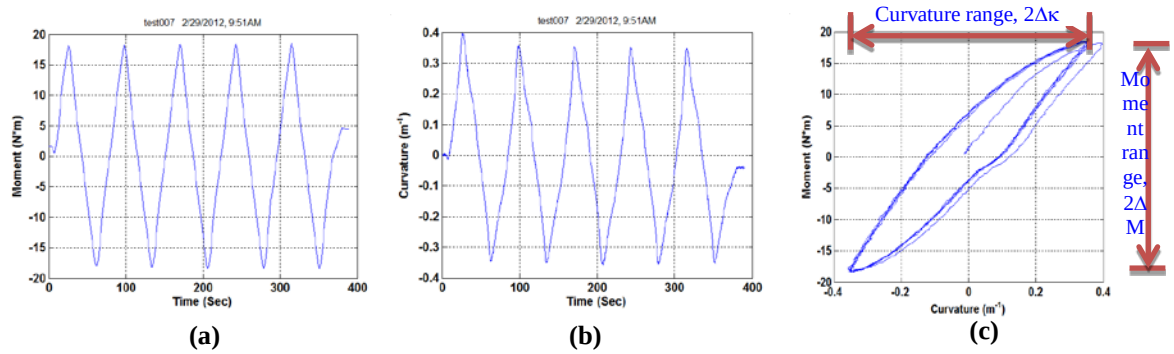

Figure 45. (a) Moment curve, (b) curvature curve, and (c) moment–curvature loops obtained by use of 3G U-frame with preloaded linear roller bearings (LRBs). The results are based on the rod made of SS tube only using the LRB U-frame on MTS 810 test machine under ±180 N, 10 N/s.

The moment-curvature relationship revealed a significant amount of hysteresis because of plastic deformation. However, the amplitude response will be focused as follows: the flexural rigidity is defined as a ratio of moment range, ΔM to curvature range; $\Delta\kappa$ will be used to characterize the property of the rod specimen.

$$\text{Flexural Rigidity, } EI = \Delta M/\Delta\kappa. \quad (1)$$

It is seen that in an elastic system, the flexural rigidity is determined by $E*I$ in which E is Young's modulus and I is the moment of inertia. The flexural rigidity should characterize the bending stiffness in some sense, while the latter also depends on the gage length. It is noted here that for a UNF rod, if one assumed perfect bonding between fuel and clad, the system flexural rigidity (EI) can be written as

$$EI_{System} = E_{Fuel}\, I_{Fuel} + E_{Clad}\, I_{Clad}\ . \quad (2)$$

However, if the cohesion bonding at the pellet-clad interface was not good or was compromised due to vibration loading, the UNF system EI can be written as

$$EI_{System} = E_{Fuel}\, I_{Fuel} + E_{Clad}\, I_{Clad} - f\,(loading, frequency, temperature), \quad (3)$$

where function f is the correction factor to take into account the interface cohesion bond evolution, and is a function of vibration loading, frequencies, and temperature as well as clad-pellet interaction. As shown in Figure 45(c), the hysteresis (loop area) is another important physical quantity revealed from the reversal bending vibration testing, which will be studied in the future.

The flexural rigidity of the rod specimen depends on both rod structure and curvature (load) level, as shown in Figure 46. This characteristic was illustrated from a series of testing on the surrogate rods, made of SS tubing, SS tubes with alumina pellet inserts (no epoxy bond, which resemble fresh fuel pellet inserts), and SS tubes filled with epoxy. The moment-curvature relation is strongly related to rod structure, as shown in Figure 46(a), while as system flexural rigidity of the rod specimen, shown in Figure 46(b), is dependent on both rod structure and curvature level. The epoxy has significant lower stiffness compared to alumina; however, it provides continuous support and has strong bonding to the SS tube, which in turn provides a higher system stiffness (EI) compared to that of the SS tube with alumina insert only. As for the SS tube with pellet inserts, the pellet insert will start to carry more load when the clad reaches certain curvature levels. A SS tube without internal support from alumina insert or filled epoxy has the lowest flexural rigidity.

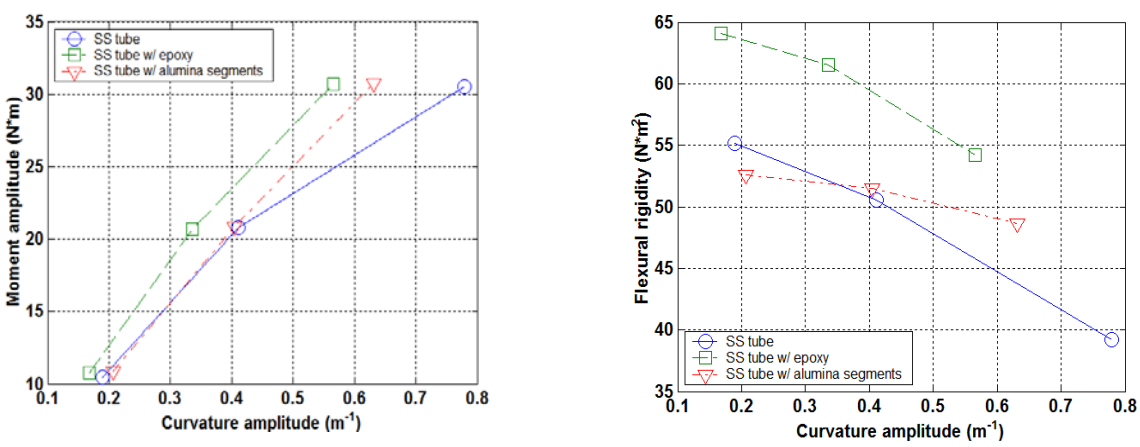

(a) **(b)**

Figure 46. Moment-curvature response and the associated system rigidity evaluation.

1.9 Test Protocol and Experimental Demonstration

A test protocol has been proposed as shown in Figure 47 for the reversal pure bending fatigue test. The protocol mainly consists of the measurement under quasi-static cyclic loading at the specified number of cycles and the cycling itself. The latter is the dynamic cyclic test at a defined frequency and amplitude.

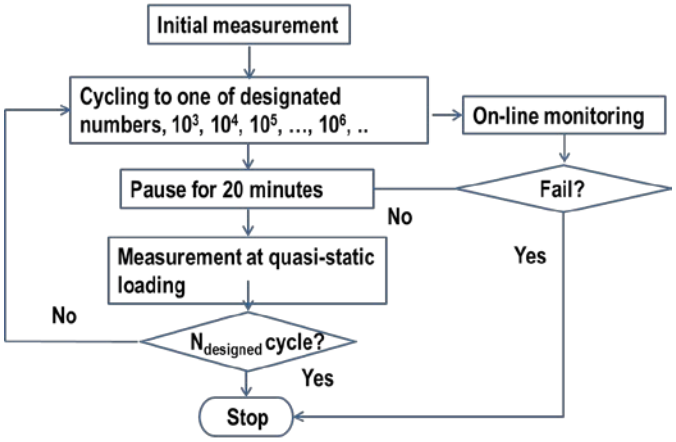

Figure 47. Test protocol for reversal bending test.

Surrogate rods have been used extensively in the out-of-cell U-bend integrated fatigue bending tester development. Two series of surrogate rods were made using SS cladding and alumina pellets. One series had the alumina pellets press-fit into the SS cladding, and the second series had the alumina pellets bonded both to themselves and to the SS cladding using cast epoxy, expressed with prefixed SSAP.

Initial tests were conducted on a MTS 810 servo-hydraulic machine in displacement control mode using the 3G U-frame test setup. Results for one of the tests, SSAP05, with bonded pellets are shown in Figure 48. The curvature of this test was fairly flat. The measurement process obviously captured the fracture of the rod specimen indicated by the sudden drop in monitored moment. The flexural rigidity dropped due to cyclic fatigue, with a 16% decrease in rigidity prior to failure. This shows that the flexural rigidity can serve as an index of the structural integrity of rod specimens. Figure 49 shows curvature and hysteresis loop responses under cyclic bending for the SSAP06 sample under different loading amplitudes applied at U-bent rigid arms. SSAP06 test result shows that the increased curvature and the decreased flexural rigidity are due to cyclic loading.

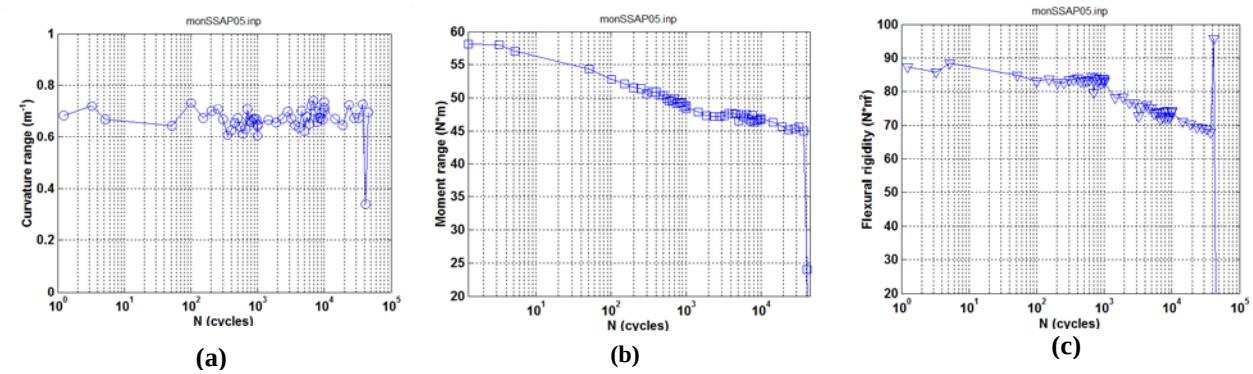

Figure 48. Variation of (a) curvature, (b) moment, and (c) rigidity based on on-line monitoring of SSAP05: ±3 mm, 2 Hz. Specimen with octagonal rigid sleeve without Teflon sheets attached; N_f = 3.7×10^4 cycles.

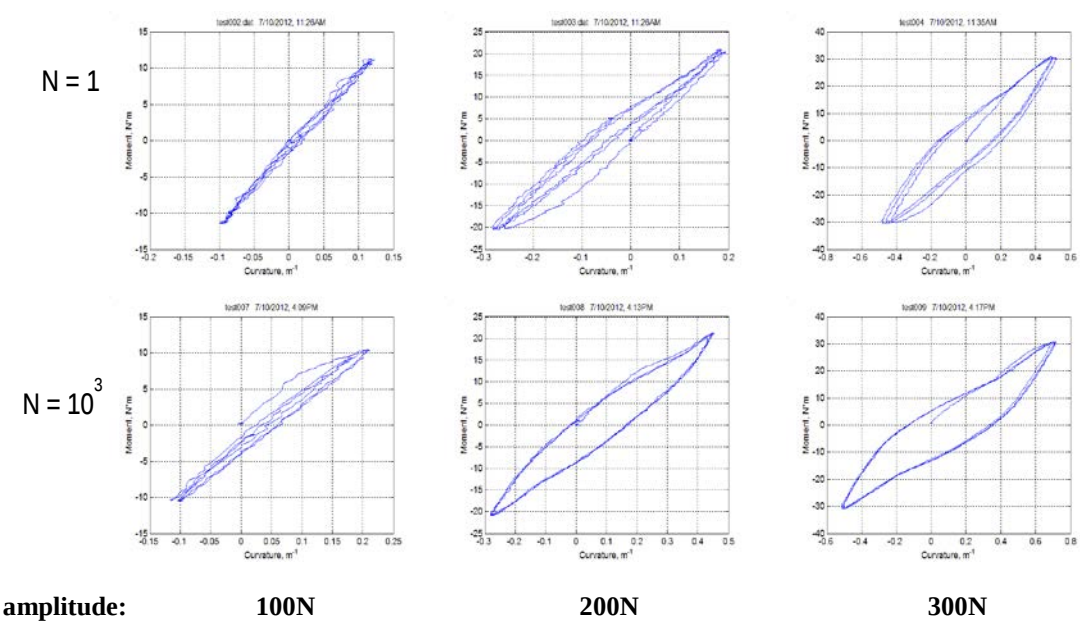

Figure 49. Cycling loading results in increases in curvature and hysteresis; measurements were conducted under load control mode on SSAP06 sample.

Other examples of property changes during the cyclic bending loading from flexural rigidity curves is illustrted in Figure 50. Figure 50(a) shows decreased flexural rigidity under increased load and under increased loading cycles from SSAP02 sample, at interval of 1, 1000, and 10000 cycles. It is noted here that SSAP02 has alumna pellet inserts but without epoxy bond. The decreased flexural rigidity with increase load level can be referred to test rod nolinear response (or yield) under increased loading. A significant decrease in flexural rigidity of SSAP02 could be the result of the direct pining effect of alumina pellet to the clad and resulting in localized yielding at the clad tube. Figure 50(b) shows opposite trends under increased curvature and reveals similar trends of flexural rigidity decrease under increased loading cycles. Due to the linear response of moment-curvature responses, no crack growth in SSAP system will be expected; the decreased flexural rigidity related to cycle frequency of SSAP04 is likely

associated with the progressive degradation of the interface bonding between pellet-pellet and pellet-SS tube.

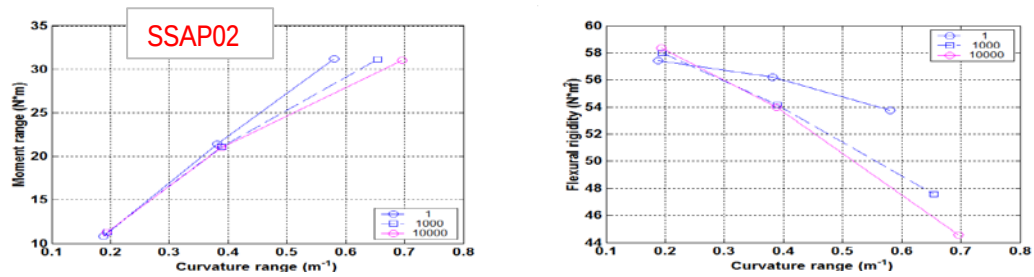

(a)

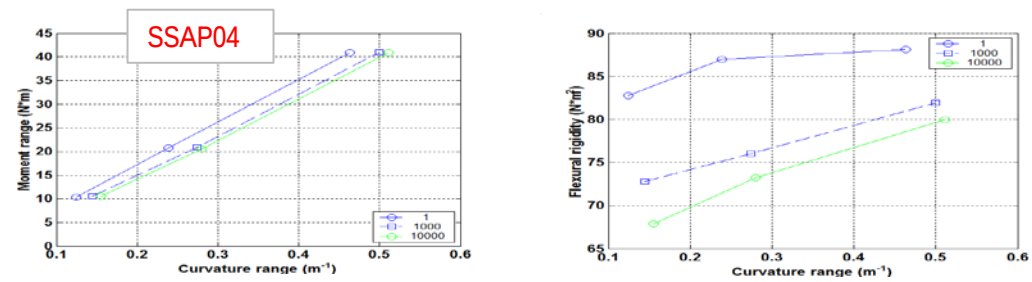

(b)

Figure 50. (a) Flexural rigidity property change results from cyclic loading. The measurements were conducted under static cyclic loading at specified points of cycle test. (b) Moment-curvature curves appeared to be quite linear in the tested range for SSAP04. Higher flexural rigidity was observed compared to SSAP02 due to epoxy bond of SSAP04. More significant decrease was observed in rigidity at higher cycles.

1.10Out-of-Cell Proof of Methodology Test Plan

The proof-of-principle demonstrations were performed on the integrated Bose U-bend tester under the load control mode. The main purpose of the proof-of-principle testing is to demonstrate the repeatability and reliability of the developed reversal U-bent tester for use in the UNF vibration integrity investigation. The surrogate rods made of SS tube embedded with epoxied alumina pellets (SSAP samples) were used for demonstration testing. The tensile test results of the SS tube, based on ASTM E8 tubular testing, is shown in Figure 51, and the estimated mechanical properties are E = 176 GPa, YS (yield strength) at 0.2% offset = 325 MPa, UTS (ultimate tensile strength) = 664 MPa.

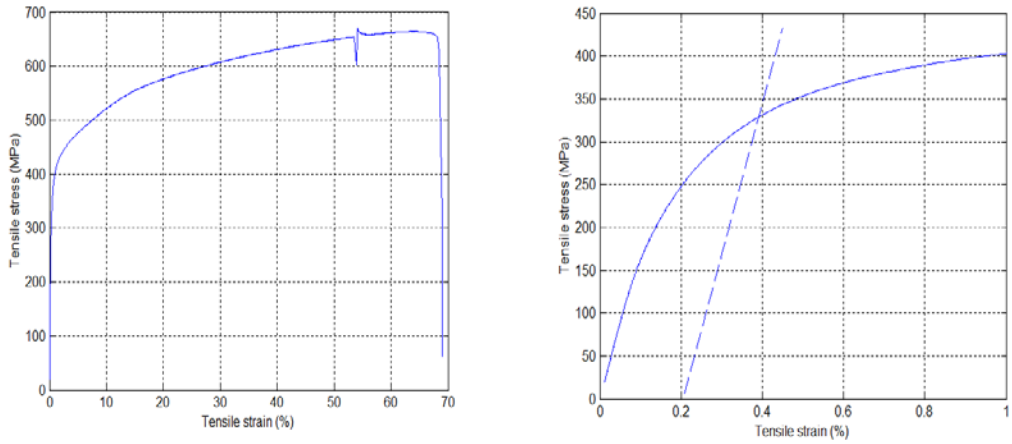

Figure 51. Axial tensile test results for stainless steel tubing used as surrogate rod for bending testing.

The reversal U-bend apparatus was integrated into a dual-linear motor system and served as the driver to conduct both the static and dynamic fatigue bending tests. The integrated testing device is shown in Figure 52, where the Bose linear motors are shown to the left and the curvature measurement device of 3-LVDTs is shown to the right of Figure 52.

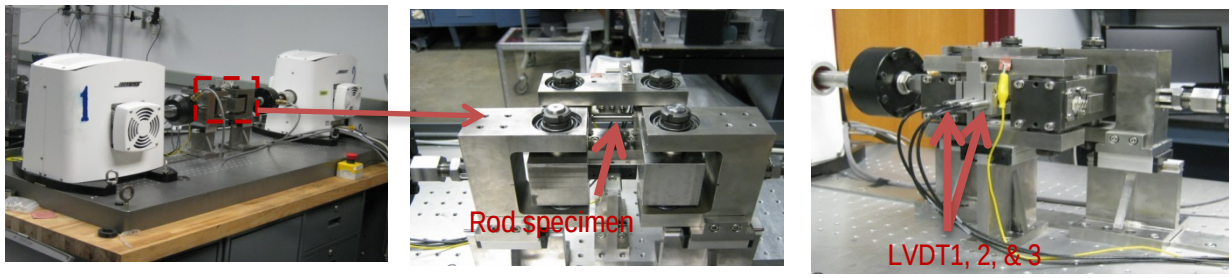

Figure 52. Integrated reversal U-bend tester used for static and dynamic fatigue bending testing.

Three static bending tests were conducted with a maximum displacement amplitude of 20 mm at the loading point, and the static bending test results are shown in Figure 53. Based on these test data, the three targeted dynamic bending loading levels were selected, namely, 20 N-m, 25 N-m, and 30 N-m ranges.

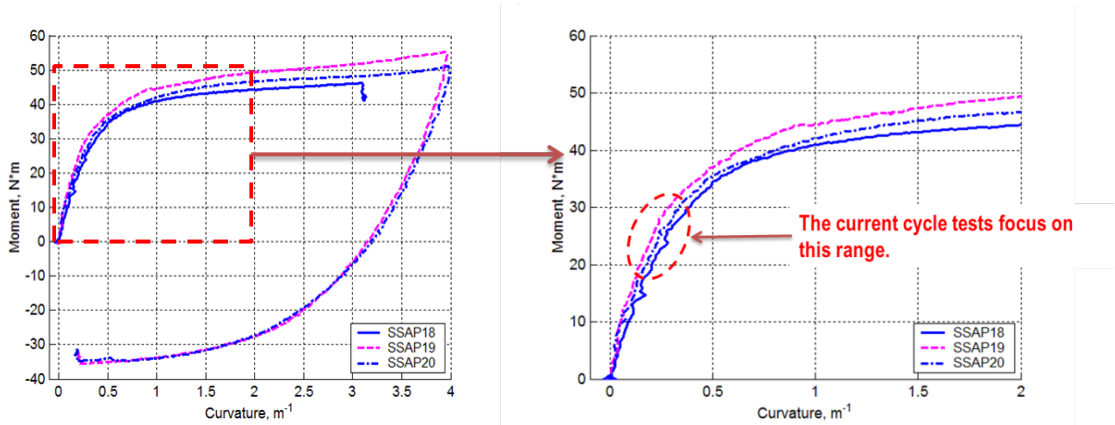

Figure 53. Static bending test result demonstrates repeatability of testing protocol.

Based on these moment loading ranges, a series of reversal bending fatigue tests were conducted. The summary of fatigue test results are shown in Figure 54, and showed that the general trend of fatigue strength is consistent with that of typical S-N (cyclic stress (S) v. cycles to failure (N)) trend curves. In order to validate the reliability of epoxy compliance materials, two of the SSAP samples were exposed to spent fuel for several weeks; the test results show that the compliance material was intact and the fatigue data were consistent with those of non-irradiated SSAP samples

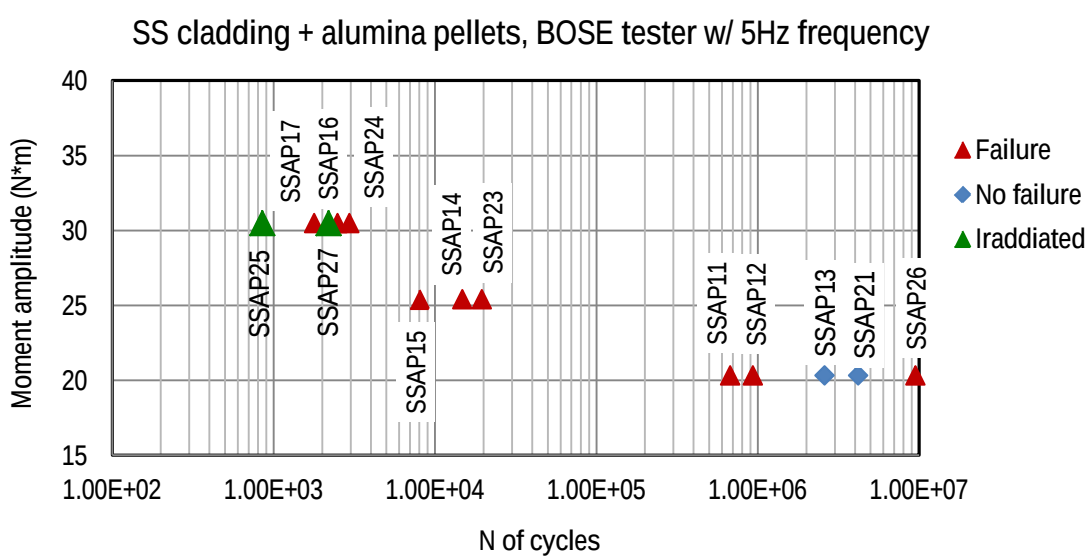

Figure 54. Reversal bending fatigue tests of SSAP samples show typical S-N trend; cycles of SSAP26 include 5.4 M at 10 Hz testing; SSAP25 was irradiated 2 weeks between six and seven fuel rod layers, and SSAP27 was irradiated in the same fuel pile for 4 weeks.

The above-mentioned proof-of-principle testing demonstrated the following.

(1) Repeatability of static testing results for a SSAP material

(2) Static testing data can be used to set meaningful test conditions for dynamic testing

(3) Repeatability of dynamic testing results for SSAP material

(4) The trend for dynamic testing at three different levels produced the expected S-N curve behavior.

(5) Exposing the epoxy in the compliant layer to an irradiation environment revealed no deleterious effects of irradiation on the epoxy.

A summary plot of real-time flexural rigidity evolution for tested SSAP samples fracture is shown in Figure 55. There are five repetitions at 200 N, three repetitions at 250 N, and four repetitions at 300 N loading levels; and there is more variability for the tests at the 200 N loading level. Such a trend curve can be useful in developing governing equations to predict the lifetime of SNF rods under vibration-induced accumulated fatigue damage.

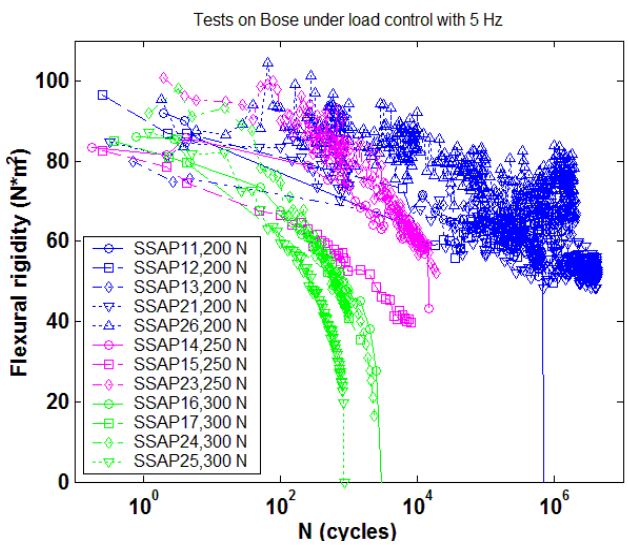

Figure 55. The evolution of SSAP flexural rigidities under different reversal bending fatigue loadings.

All the fractured SSAP samples failed at the gage section as designed; some of the fractured samples and the associated flexural rigidity evolution are shown in Figures 56 and 57 for SSAP 11 and SSAP 12 samples, respectively.

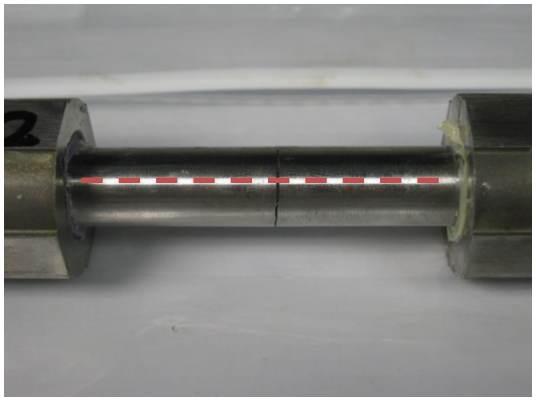

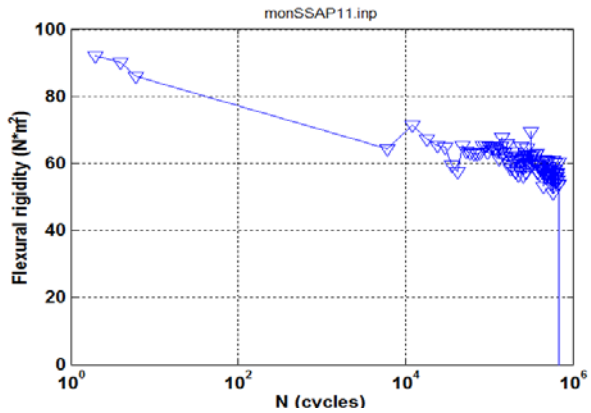

Figure 56. Test for SSAP11 was conducted with original setup: load ±200 N, moment ±20.38 N*m, 5 Hz. Initial displacement ±2.5 mm, initial curvature ±0.27 /m, initial strain ±0.14%. Specimen fractured near 678 K cycles. About 40% drop in flexural rigidity occurred.

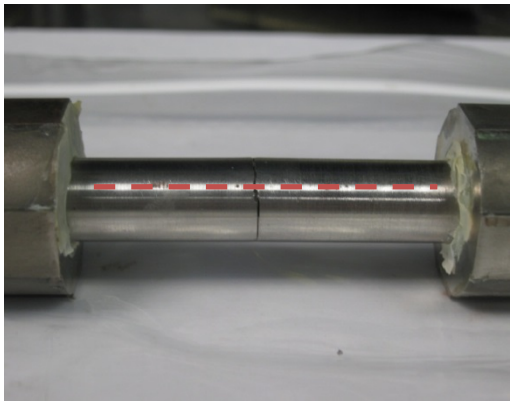

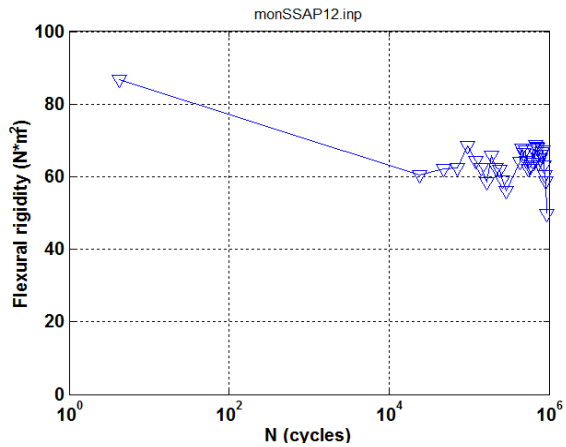

Figure 57. Test for SSAP12 was conducted with modified setup conditions: load ±200 N, moment ±20.38 N*m, 5 Hz. Initial displacement ±2 mm, initial curvature ±0.23/m, initial strain ±0.13%. Specimen fractured near 936 K cycles. About 42% drop in flexural rigidity.

1.11 Out-of-Cell Proof of Methodology Testing Using Zircaloy-4 Samples

In order to support the transition from NRC supported testing to UFD campaign directed bend testing, two 5 ft prototypic Zircaloy-4 tubes with OD 9.50 mm and ID 8.36 mm were obtained from Sandia National Laboratories and sectioned into twenty 6 in. short tubes. At the same time, ten 5/16 in. × 12 in. alumina rods were cut into small 15.24 mm pieces. These small pieces were then used as surrogate fuel pellets within the 6 in. Zircaloy-4 cladding tubes.

The pellet–cladding interaction was studied through simulations with and without epoxy bonding. Preparation of epoxy-bonded surrogate rods involved epoxying the alumina pellet inside the cladding tubes.

1.12 MONOTONIC TEST

Monotonic testing was conducted under displacement control. The displacement channels of the test machine were set at a load rate of 0.2 mm/s to 10.00 mm and back to 0 mm at the same rate. This displacement control is equivalent to a unidirectional 0.01 Hz triangle wave. Because the dual linear motors and U-frame setup are connected in series, the applied displacement to the U-frame is accumulated. Thus, the total (or relative) maximum displacement in the test was 20.00 mm.

The bend of the rod was measured by using three linear variable differential transformers (LVDTs); the curvature was used in this study to characterize the bending of the rod.

1.13 CYCLE TEST

The reverse cyclic bend testing consisted of (1) measurements at the specified number of cycles and (2) the cycling itself. The measurements included three cycles of 0.05 Hz sine waves with peak displacements of ±0.4, ±0.6, and ±0.8 mm.

The cycling involved using 5 or 10 Hz sine waves under load control. The determination of the load amplitudes depended on the experimental results from the monotonic test. In general, the selected load amplitude captured lifetimes at 10^4, 10^5, and 10^6 cycles.

The cycle test stopped whenever the following events occurred: (1) the predetermined limits in displacement 1 or 2 exceeded 4 to 6 mm or (2) the accumulative cycle number exceeded 1 or 2 million.

Data of displacements, loads, and LVDTs were acquired during both the measurements and cycling at defined sampling rate and intervals. The moment-curvature curvatures were carefully examined and validated for each test. The curvature range, moment range, and flexural rigidity (moment per unit curvature) were used in this test program.

2. RESULTS OF MONOTONIC TEST

The resistance of the U-frame to loading can be substantial, especially when the monotonic test demands a large displacement, with average readings of the load channels as high as 40 N near the 10.00 mm displacement channels. Thus, the load channel readings were corrected to take into account the resistant force from the system.

2.1 Surrogate Rod with Epoxy Bond

Results for ZRAP01 and ZRAP02 are shown in Figures 58 and 59. The loading results initially show a linear response, followed by a nonlinear stage with three unloading valleys before the peak point is reached. These unloading valleys correspond to popping sounds emitted during the test. Optical microscopy of ZRAP01 revealed that multiple transverse cracks had developed (Figure 60); therefore, the unloading points observed on the loading curve for ZRAP01 may be related to the cracking events. In the case of ZRAP02, however, no crack can be seen on the surface of the rod, so it remains unclear whether the multiple unloading valleys correspond to cracks inside or outside the cladding tube.

The detailed examination of the moment–curvature plot for each test showed a transition stage existing between 10 and 20 Nm. The loading before 10 Nm and after 20 Nm corresponded to two linear stages. A rigidity of 27.8 to 32 Nm was obtained through linear regression analysis of the initial stage. This value is quite close to the theoretical prediction, assuming 10% of the full alumina rod rigidity is used.

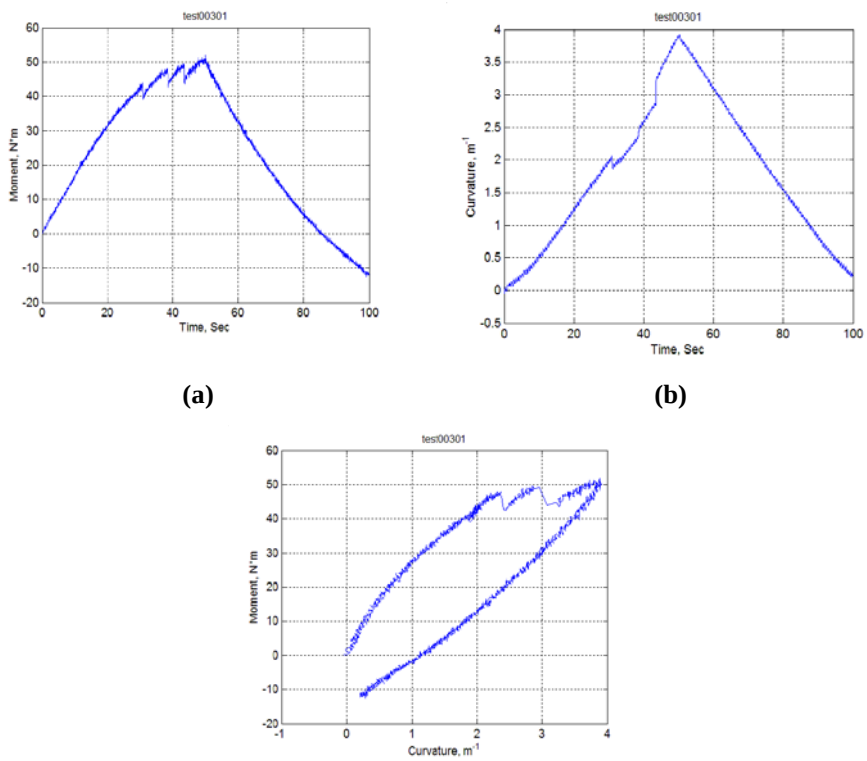

Figure 58. (a) Moment, (b) curvature, and (c) moment–curvature curve for static bending test of ZRAP01 under 0.2 mm/s and maximum relative displacement of 20 mm at loading points of U-frame setup.

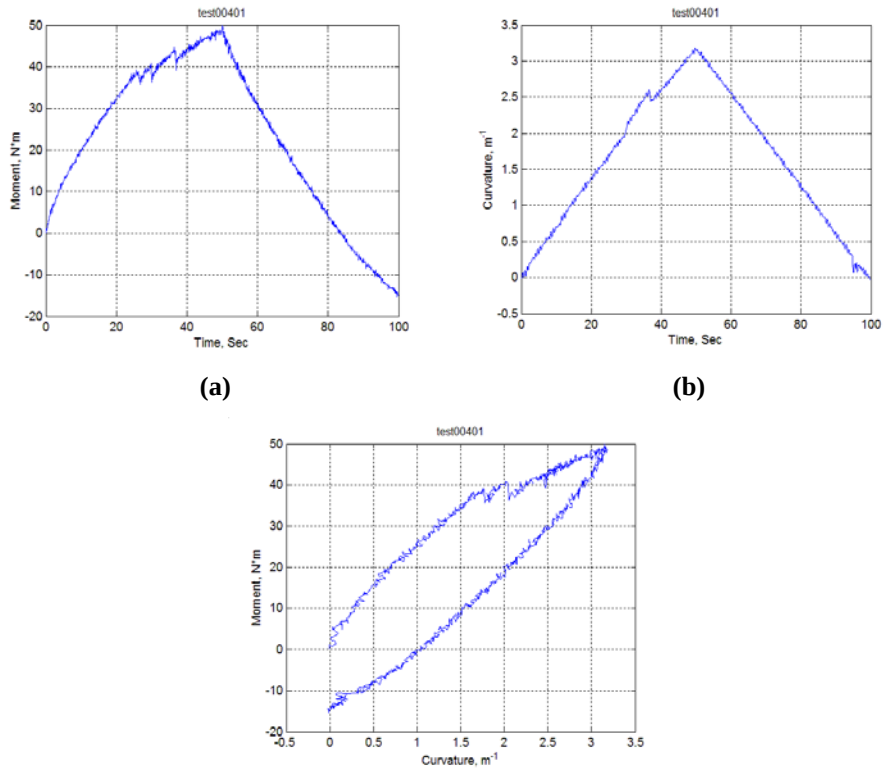

Figure 59. (a) Moment, (b) curvature, and (c) moment–curvature curve for static bending test of ZRAP12 under 0.2 mm/s and maximum relative displacement of 20 mm at loading points of U-frame setup.

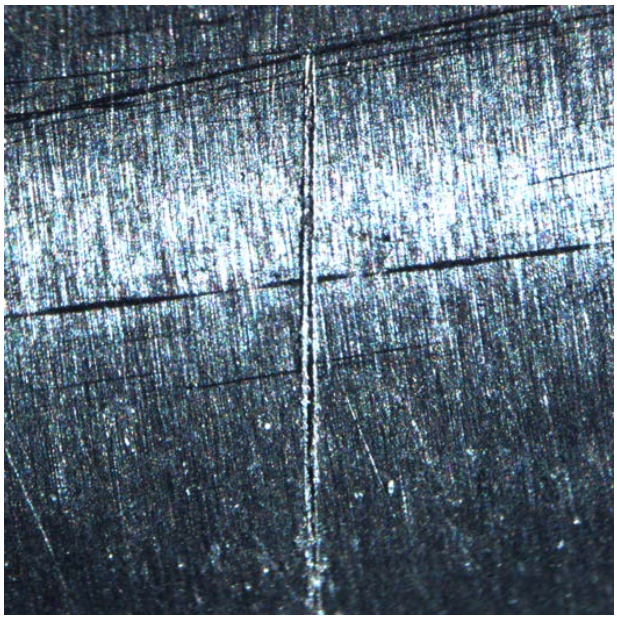

Figure 60. Multiple transverse cracks developed on the surface of ZRAP01 during monotonic loading.

Although the microprocess that dictated the behavior of the rod in this stage is unclear, it is believed that the yielding of cladding and the debonding of the epoxy played critical roles in accelerating the fatigue of the rod being examined. Therefore, the range of 10 to 20 Nm, or 100 to 200 N at the loading points of the U-frame, was set as the target amplitude range for the cyclic test discussed below. Later the upper bound of the load range was extended to 300 N to expand the range of the lifetime of the rod at the left end.

2.2 Surrogate Rod without Epoxy Bond

The results for the rod specimen without an epoxy bond, ZRAPM01, are given in Figure 61. It is interesting to note that both the maximum curvature and moment obtained under the same relative displacement of 20.00 mm are lower than those of ZRAP01. In particular, the maximum moment decreased from 50 Nm to 35 Nm. The estimate of flexural rigidity based on the initial linear stage of moment curvature resulted in a value of 14.5 Nm. This level of rigidity matches the theoretical prediction only if the contribution of alumina pellets is omitted; therefore, the impact of the epoxy bond on the response of the rod under bending is substantial.

At the same time, the range of load amplitudes used in the cycle tests described in Sect. 4 was the same as that for rods with an epoxy bond.

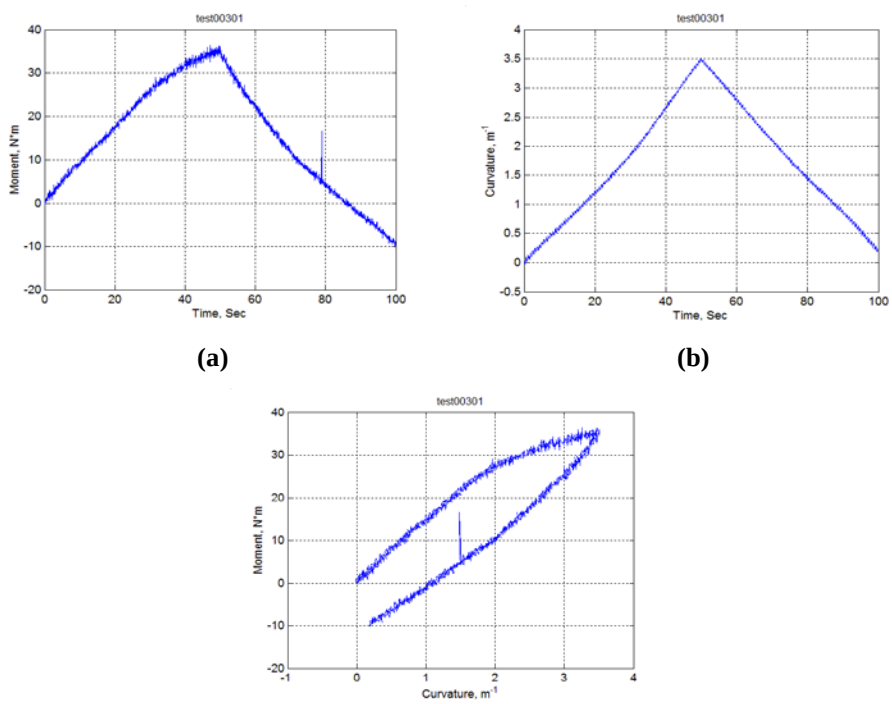

Figure 61. (a) Moment, (b) curvature, and (c) moment–curvature curve for static bending test of ZRAPM01 under 0.2 mm/s and maximum displacement of 20 mm at loading points of U-frame setup.

3. RESULTS OF CYCLE TEST

3.1 Summary

A summary of the results for the cycle tests conducted in this project along with monotonic tests and calibration is provided in Table 13. The relationship of the moment to the number of cycles is given in Figure 62.

For the epoxy-bond case, the rod fractures were observed for most of the cyclic tests with moments of more than 10 Nm. On the other hand, fractures were observed for the no-epoxy-bond case in all of the moment levels.

Table 13. Summary of Zircaloy-4 surrogate rod tests

Specimen No.	Epoxy	Mode	Control	Amp.[a] (mm, N)	Amp. (mm, N*m)	Freq. (Hz)	Lifetime (N or Nf)	Notes
ZRAP01	Bond	Monotonic	Displacement	20	20	0.01		
ZRAP02	Bond	Cycle	Load	100	10.16	5	1.27E+06	No failure
ZRAP03	Bond	Cycle	Load	200	20.32	5	4.06E+04	Fractured
ZRAP04	Bond	Cycle	Load	150	15.24	5	5.49E+05	Fractured
ZRAP05	Bond	Calibration	Load	80	8.128	1,5,10		
ZRAP06	Bond	Cycle	Load	200	20.32	10	7.25E+03	Fractured
ZRAP07	Bond	Cycle	Load	200	20.32	10	6.38E+03	Fractured
ZRAP08	Bond	Cycle	Load	100	10.16	10	2.00E+06	No failure
ZRAP09[b]	Bond	Cycle	Load	150	15.24	5	2.22E+06	Fractured
ZRAP10	Bond	Cycle	Load	175	17.78	5	5.86E+04	Fractured
ZRAP11	Bond	Cycle	Load	200	20.32	5	4.17E+04	Fractured
ZRAP12	Bond	Cycle	Displacement	10	10	0.01		
ZRAP13	Bond	Cycle	Load	250	25.4	5	1.10E+04	Fractured
ZRAP14	Bond	Cycle	Load	300	30.48	5	3.32E+03	Fractured
ZRAPM01	None	Monotonic	Displacement	20	20	0.01		
ZRAPM02	None	Cycle	Load	200	20.32	5	6.71E+03	Fractured
ZRAPM03	None	Cycle	Disp	150	15.24	5	2.31E+04	Fractured
ZRAPM04	None	Cycle	Disp	100	10.16	10	7.44E+03	Fractured

[a] For the displacement, the amplitude means that a relative displacement at the two load points of the U-frame was used.
[b] The last 79,000 cycles used 10 Hz in the cycle test.

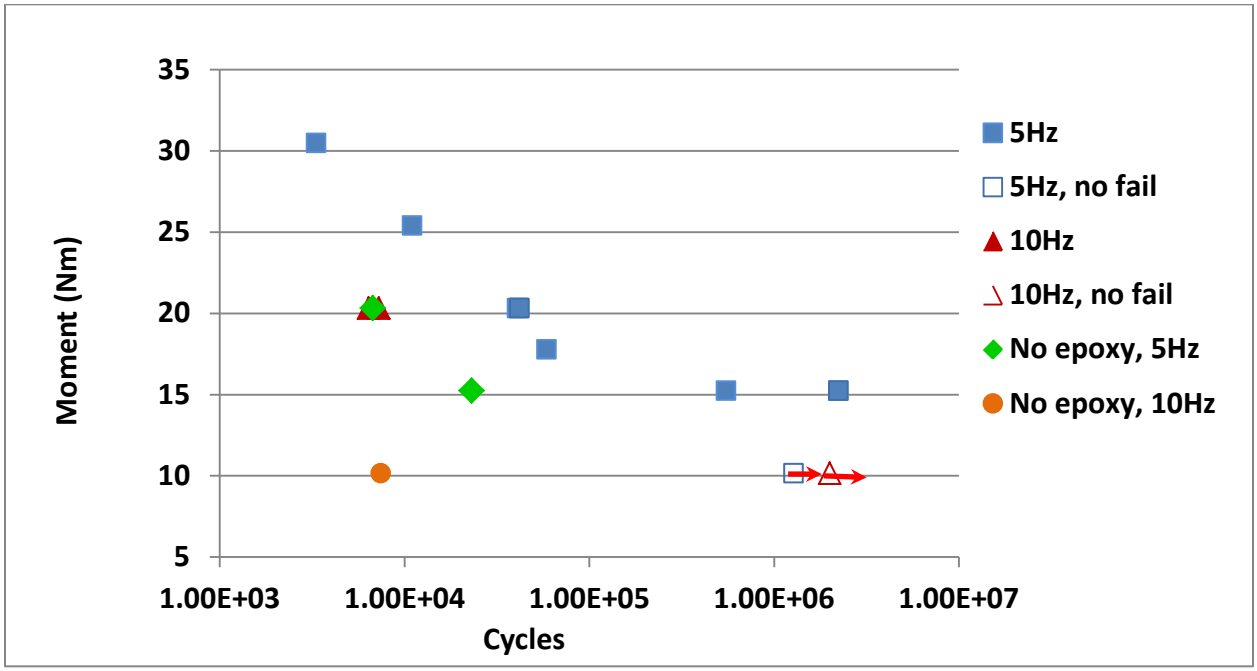

Figure 62. Summary of cycle tests of Zircaloy-4 surrogate rods.

3.2 Surrogate Rod with Epoxy Bond

The resistance of the system under dynamic loading or a cycle test was found to be at the noise level, and therefore, the data processing of dynamic testing did not involve the data correction required for static loading since the level of loading amplitude is relatively small compared to that used in static loading.

3.2.1 5 Hz Cycle Tests

The results of the 5 Hz cycle tests are presented in Figures 63 to 70 for ZRAP02 to ZRAP04, ZRAP09 to11, ZRAP13, and ZRAP14, respectively. Except for that of ZRAP02, all of the rigidity fatigue curves demonstrated a continuous decrease over the entire course of the cyclic test. The continuous degradation was also observed for ZRAP09, whose test (+/-150 N, 5 Hz) went beyond 2 million cycles. The specimen fractured shortly after the test was switched to 10 Hz to accelerate the fatigue. Another important observation is that for those fractured or cracked specimens, the degradation rate did not seem to change very much during the cyclic test, even when the specimen was about to fracture.

The results based on measurements exhibited variation comparable to those from online monitoring data. The selected curvature ranges for measurements allowed the bend of the rod to fall within the elastic region of the moment–curvature curve. These curvature ranges for measurements were all equal to or less than those used in cycling; therefore, the effect of measurement on the cycling is not believed to have been substantial, as validated by the concurrent changes of rigidity in both processes. For example, in the case of ZRAP02, the rigidity curves based on measurements were quite settled within a defined region, while that of online rigidity was correspondingly stabilized near the 35 Nm level.

Figure 71 exhibits the fractured rods of specimens ZRAP03, ZRAP04, ZRAP09, ZRAP10, and ZRAP11. It can clearly be seen that all of failures occurred in the gauge section, as designed. The micrograph in Figure 72 shows a part of rod ZRAP13 in which the fracture also occurred in the gauge section. The two transverse cracks (about 2 to 3 mm long) can clearly be seen to have coalesced near a surface flaw.

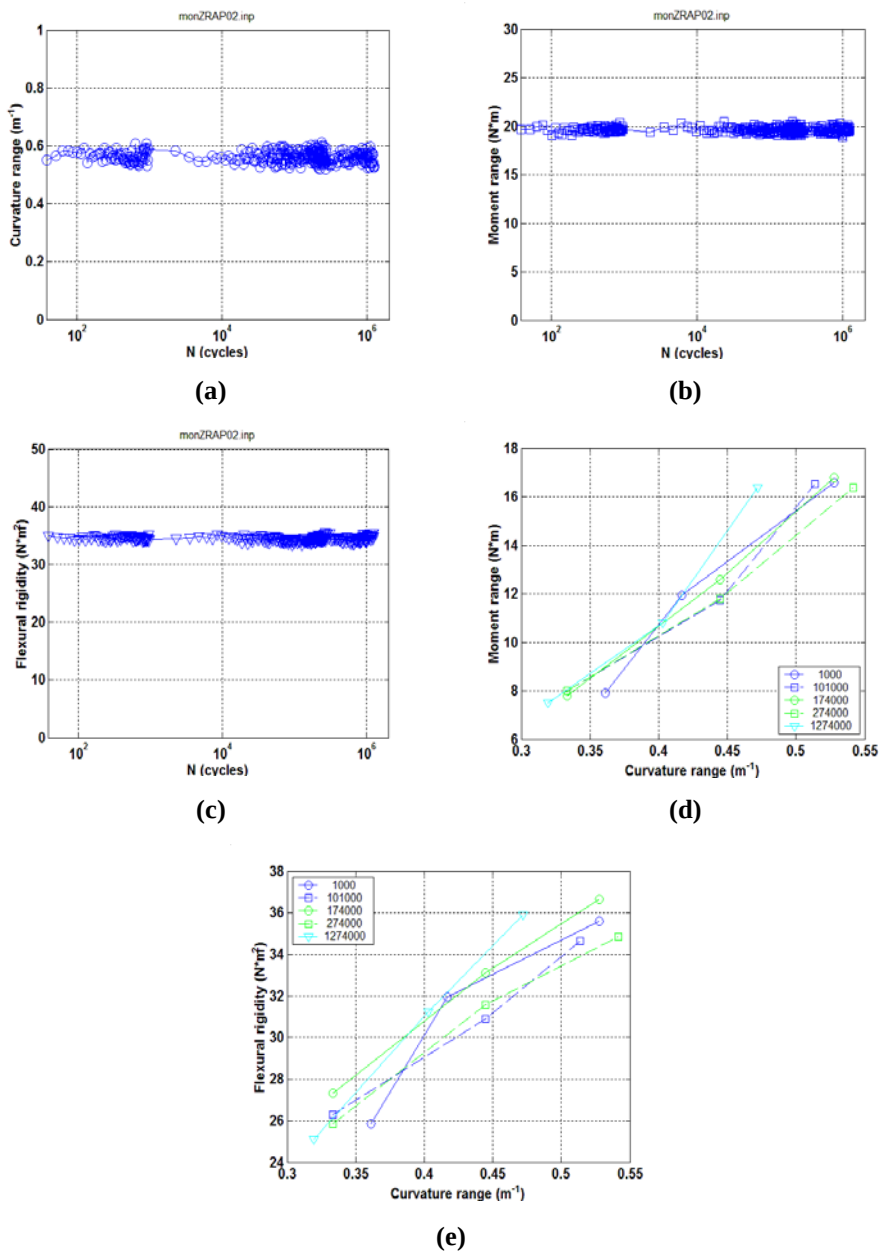

Figure 63. Variation of (a) curvature, (b) moment, and (c) rigidity based on online monitoring; measurement results for (d) curves of moment versus curvature and (e) flexural rigidity versus curvature of ZRAP02: ±100 N, 5 Hz; no failure observed.

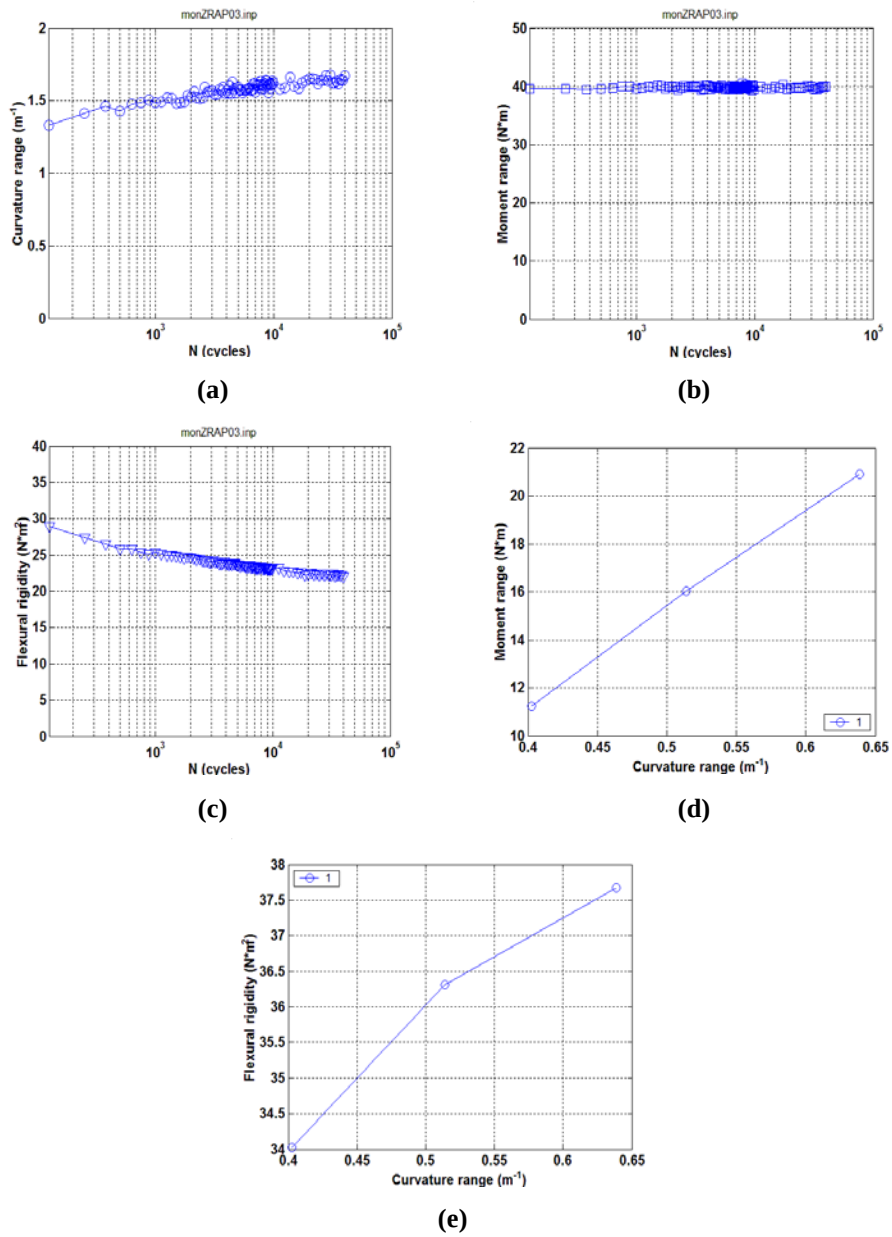

Figure 64. Variation of (a) curvature, (b) moment, and (c) rigidity based on online monitoring; measurement results for (d) curves of moment versus curvature and (e) flexural rigidity versus curvature of ZRAP03: ±200 N, 5 Hz.

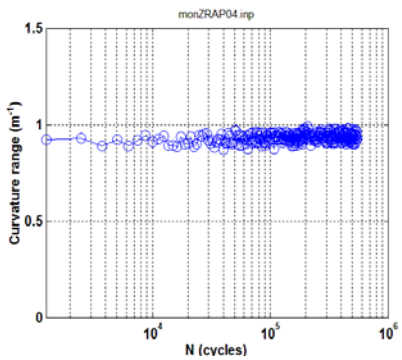

(a)

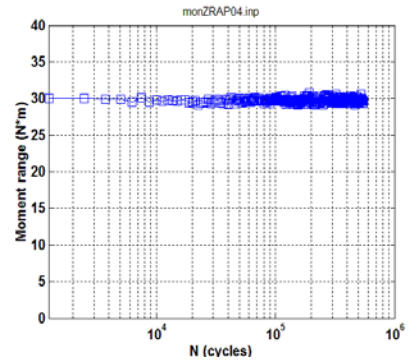

(b)

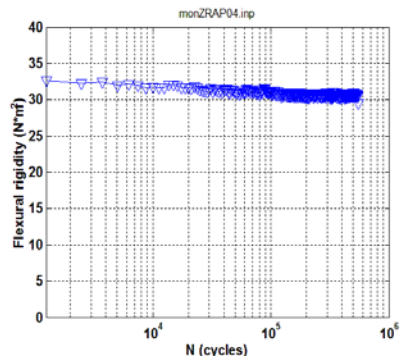

(c)

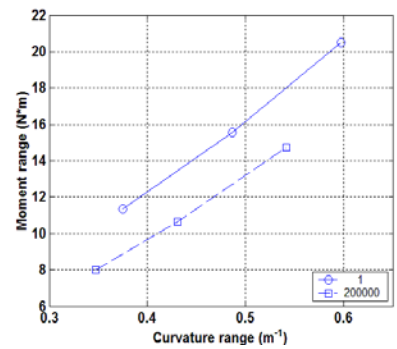

(d)

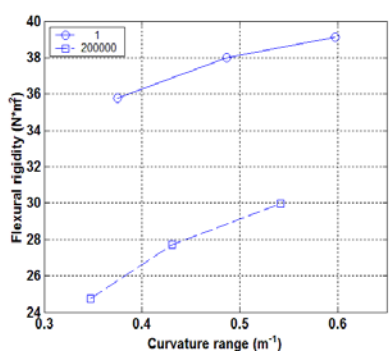

(e)

Figure 65. Variation of (a) curvature, (b) moment, and (c) rigidity based on online monitoring; measurement results for (d) curves of moment versus curvature and (e) flexural rigidity versus curvature of ZRAP04: ±150 N, 5 Hz.

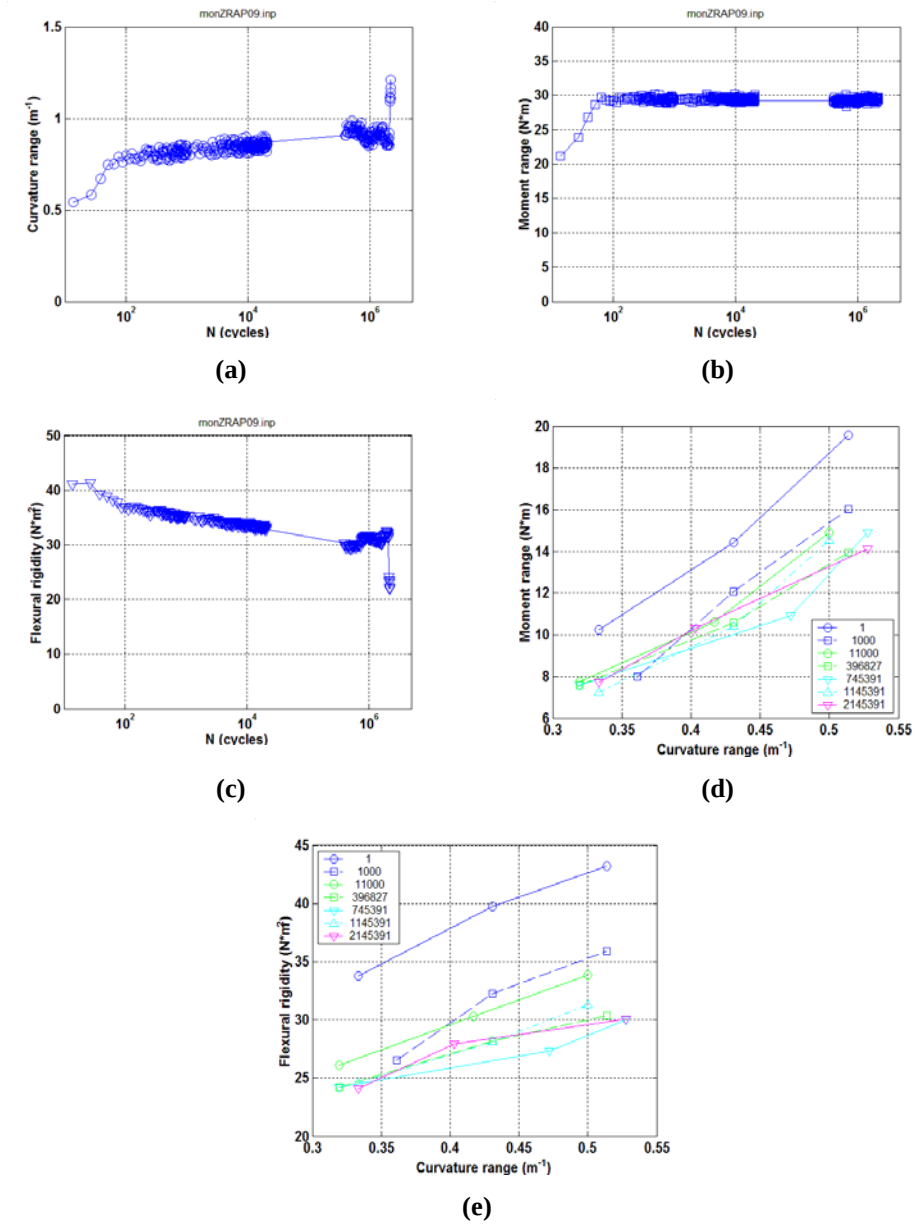

Figure 66. Variation of (a) curvature, (b) moment, and (c) rigidity based on online monitoring; measurement results for (d) curves of moment versus curvature and (e) flexural rigidity versus curvature of ZRAP09: ±150 N, 5 Hz.

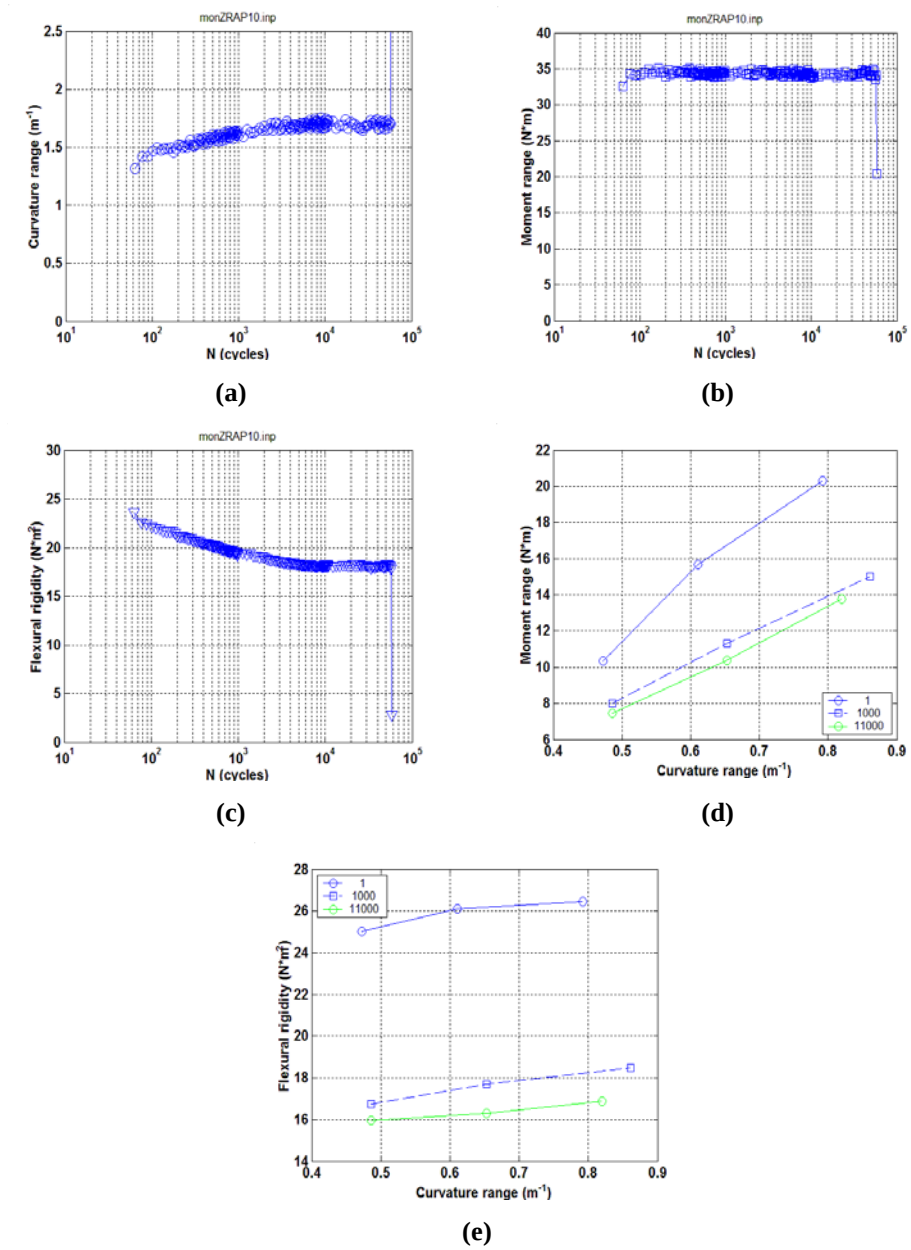

Figure 67. Variation of (a) curvature, (b) moment, and (c) rigidity based on online monitoring; measurement results for (d) curves of moment versus curvature and (e) flexural rigidity versus curvature of ZRAP10: ±175 N, 5 Hz.

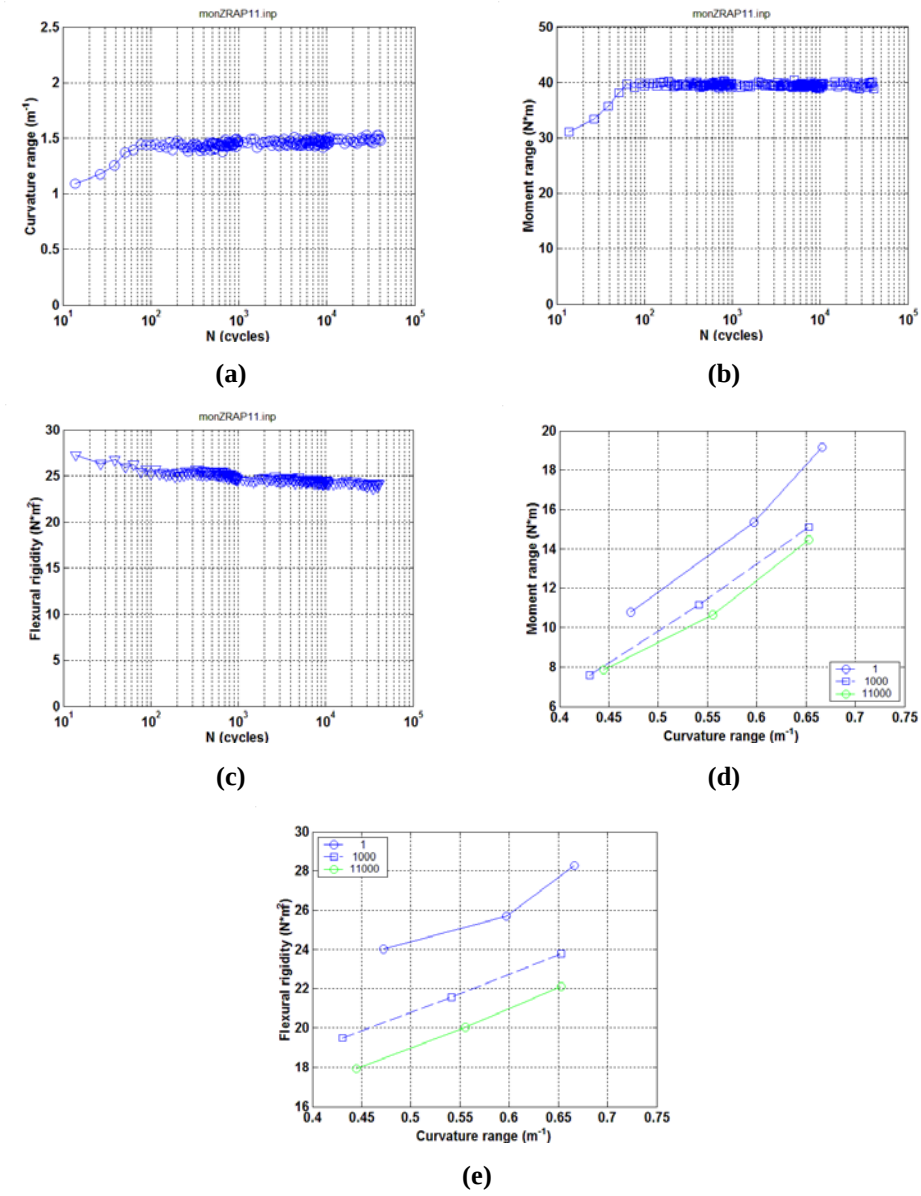

Figure 68. Variation of (a) curvature, (b) moment, and (c) rigidity based on online monitoring; measurement results for (d) curves of moment versus curvature and (e) flexural rigidity versus curvature of ZRAP11: ±200 N, 5 Hz.

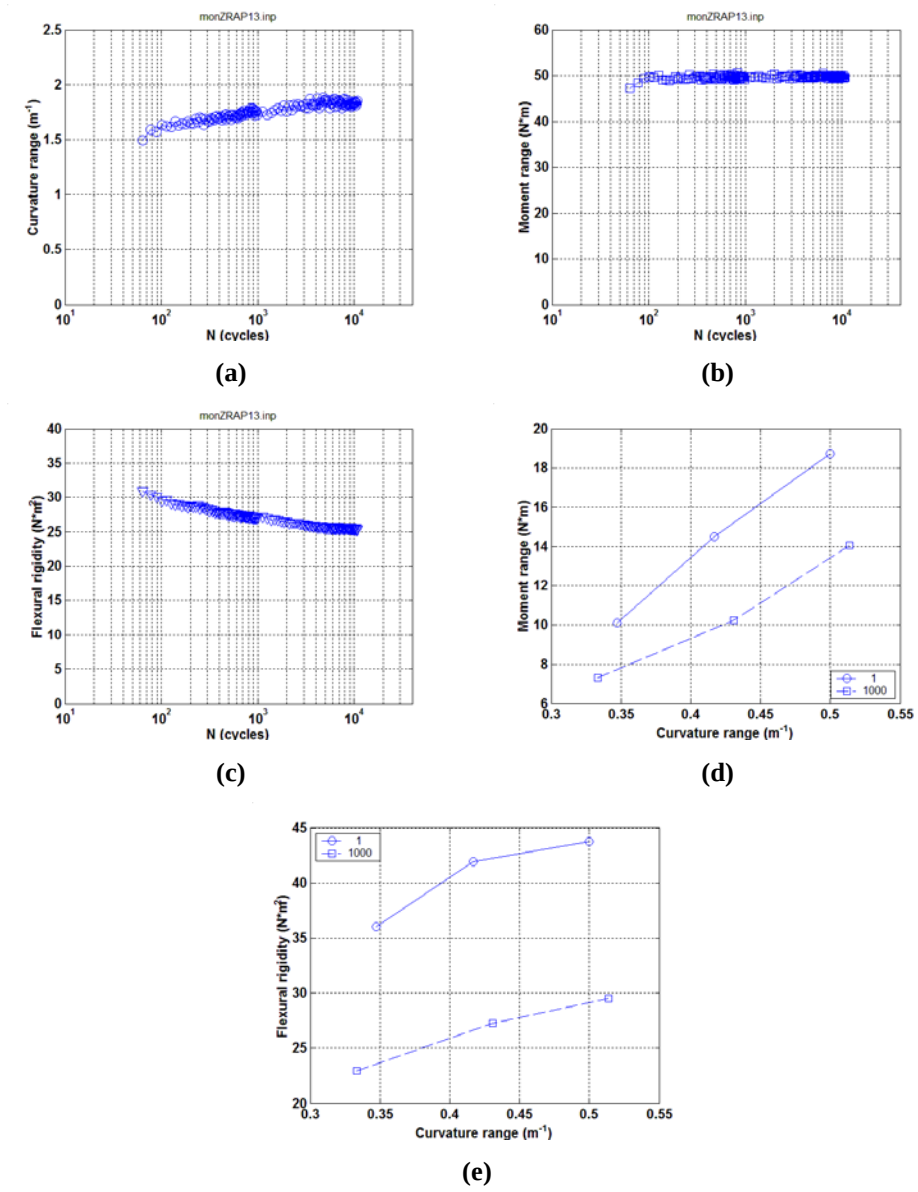

Figure 69. Variation of (a) curvature, (b) moment, and (c) rigidity based on online monitoring; measurement results for (d) curves of moment versus curvature and (e) flexural rigidity versus curvature of ZRAP13: ±250 N, 5 Hz.

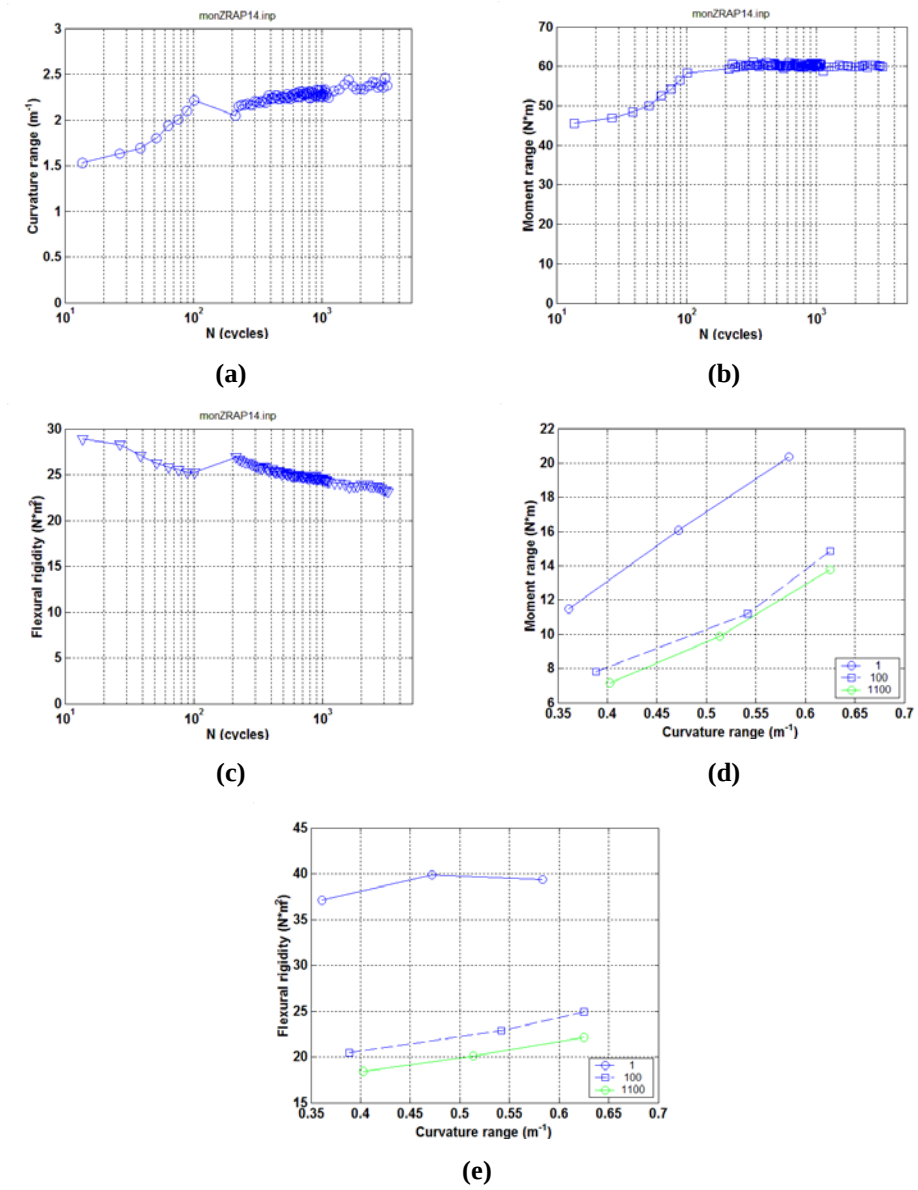

Figure 70. Variation of (a) curvature, (b) moment, and (c) rigidity based on online monitoring; measurement results for (d) curves of moment versus curvature and (e) flexural rigidity versus curvature of ZRAP14: ±300 N, 5 Hz.

(a)

(b)

(c)

(d)

(e)

Figure 71. Images showing fractured rods for (a) ZRAP03, (b) ZRAP04, (c) ZRAP09, (d) ZRAP10, and (e) ZRAP11.

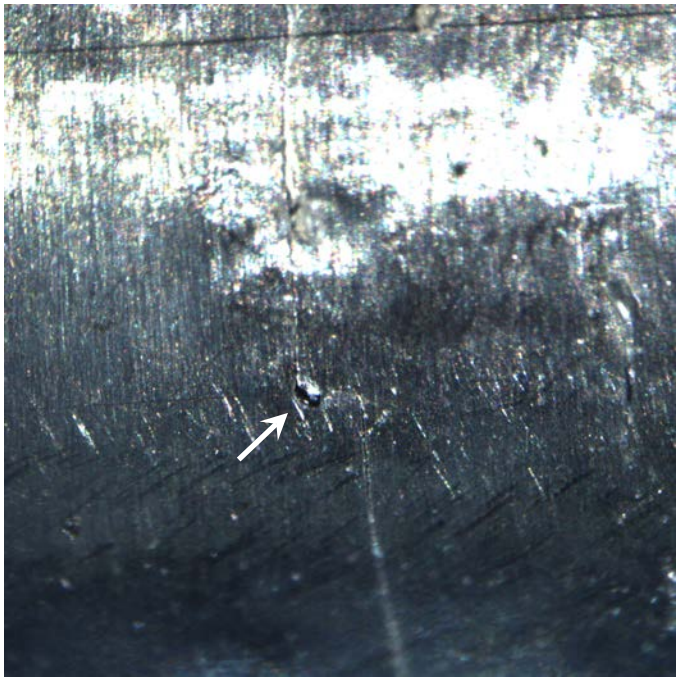

Figure 72. Micrograph of part of the surface of ZRAP13 rod showing transverse fracture of about 4 mm length kinked near a surface flaw.

4. REFERENCES

1. M. Billone, Y. Yan, T. Burtseva, and R. Daum, *Cladding Embrittlement during Postulated Loss-of-Coolant Accidents*, NUREG/CR-6967 (ANL-07/04), prepared for the U.S. Nuclear Regulatory Commission by Argonne National Laboratory, Argonne, IL, 2008.
2. R. Daum, H. Tsai, Y. Liu, and M. Billone, "High-Burnup Cladding Mechanical Performance during Cask Storage and Post-Storage Handling and Transportation," Nuclear Safety Research Conference, Washington, DC, October 25–27, 2004.
3. M. C. Billone, T. Burtseva, Y. Yan, and S. Majumdar, "Overview of Spent Nuclear Fuel Program: Test Plan and High Burnup Cladding at ANL," NRC Program Review Meeting, Argonne, IL, July 7, 2010.
4. J. Huanga and S. Huanga, "Hydriding of Zirconium Alloys in Hydrogen Gas," *Mat. Sci. Eng. A* 161(2), 247–253 (April 1, 1993).
5. Y. Choi, J. W. Lee, Y. W. Lee, and S. I. Hong, "Hydride Formation by High Temperature Cathodic Hydrogen Charging Method and Its Effect on the Corrosion Behavior of Zircaloy-4 Tubes in Acid Solution," *J. Nucl. Mat*. **256**, 124–130 (1998).
6. Y. Yan, J. Kiggans, and C. Davisson, "Hydrogen Charging Techniques Being Developed at ORNL," DOE-UFC Clad Workshop, Las Vegas, NV, November 15–17, 2011.
7. J.-A. J. Wang, H. Wang, Y. Yan, R. Howard, and B. Bevard, *High Burn-up Spent Fuel Vibration Integrity Study Progress Letter Report (out-of-cell fatigue testing development – Task 2.1)*, ORNL/TM-2010/288, Oak Ridge, Tenn., January 2011.
8. J.-A. J. Wang, H. Wang, T. Tan, H. Jiang, T. Cox, and Y. Yan, *Progress Letter Report on U-frame Test Setup and Bending Fatigue Test for Vibration Integrity Study (out-of-cell fatigue testing development – Task 2.2)*, ORNL/TM-2011/531, Oak Ridge, Tenn., January 2012.
9. J.-A. J. Wang, H. Wang, T. Cox, and Y. Yan, *Progress Letter Report on U-frame Test Setup and Bending Fatigue Test for Vibration Integrity Study (out-of-cell fatigue testing development – Task 2.3)*, ORNL/TM-2012/417, August, 2012.
10. J.-A. J. Hong Wang, J. Wang, T. Tan, H. Jiang, T. S. Cox, R. L. Howard, B. B. Bevard, and M. Flanagan, "Development of U-frame Bending System for Studying the Vibration Integrity of Spent Nuclear Fuel," *J. Nucl. Mat.*, **440**, 201–213 (2013).

This page intentionally left blank.

APPENDIX A
DOSE RATE SURVEY REPORT ON HYCD-1 AND HYCD-2

ORNL Radiological Survey (3525-345245)

Survey Number:	3525-345245	**Survey Date:**	02/18/2013 1:42 PM
F Office:	3525	**Submitted Date:**	Not Submitted
Surveyor:	Allison Burnette (00963890)	**Approved Date:**	Not Approved
Surveyor (Other):	NA	**Survey Type:**	Other
Division / Group:	Nonreactor Nuclear Facilities Division	**RWP Number:**	3525-18367-7
Building:	3525	**Tickler Number:**	NA
Room:	130	**Person-Hours:**	1

Specific Location:
Charging Area, West Cell Port

Description:
Radiation and contamination survey in support of Dose Rating 2 HYCD Capsules.

Radiological Conditions:
The Charging Area was posted as a Controlled Area, Airborne Radioactivity Area, Radiation Area, and Contamination Area.

Dose rate at the threshold of the West Cell Port was 35 mrem/hr.
Work Area dose rates ranged from 0.5 to 685 mrem/hr.

The 2 HYCD capsules were raised to the West Cell Port using the in cell Manipulators to obtain dose rates.

Dose rates on the HYCD capsules were:

- UFC1D1C: 20 rem/hr at 1cm and 1 rem/hr at 30cm
- LRR1D7: 40 rem/hr at 1cm and 4 rem/hr at 30cm
- Note: Dose rates were taken using an Ion Chamber. The dose rates were taken at 1 cm per the researchers request.

R vable contamination levels after the dose rates were taken ranged from:

- <20 dpm/100cm^2 alpha
- <200 to 486 dpm/100cm^2 beta-gamma

Created by Allison Burnette (00963890) - Edited by Allison Burnette (00963890)

Instruments (8)

Instrument	Model	Next Calibration	Comments
0069461	ISOLO	09/30/2013	
M075758	3030	09/30/2013	
M133725	PORT	09/01/2013	Low Vol.
M133819	3030	09/30/2013	
M146622	RO-20	10/10/2013	
M146915	PAS	04/15/2013	
M146986	RadEye SX A/B	05/13/2013	
M147073	RadEye B20ER	04/22/2013	

COPY

Smears (3) (dpm/100cm2 unless noted)

Number	Alpha	Beta	Location
1	<20	486	Wall Under West Cell Port
2-	<20	<200	Floor Under West Cell Port

Attachments (0)

This page intentionally left blank.

APPENDIX B
HYDRIDED ZIRCALOY-4 AND ZIRLO SAMPLES FOR HFIR IRRADIATION

Assemble #	Sample length	Materials	Hydrogen content wppm	Status	Comments
HYCD#1	3×1 in.	Zircaloy-4	20, 450, 820	Inserted into HFIR on 3/26/12. Removed after 1 cycle	Feasibility testing (equiv. burnup: <10 GWd/MTU)
HYCD#2	3×1 in.	Zircaloy-4	20, 450, 550	Inserted into HFIR on 3/26/12. Removed after 3 cycles	Provide a guideline for following tests (equiv. burnup: ≈20 GWd/MTU)
HYCD#3	6 in.	Zircaloy-4	770	Inserted into HFIR on 3/26/12 (removed after cycle 447)	Single 6-in.-long sample (equiv. burnup: ≥60 GWd/MTU)
HYCD#4	3×1 in.	ZIRLO	15, 450, 460	Inserted into HFIR on 11/20/12 (removed after cycle 447)	Multi 1-in.-long samples (equiv. burnup: ≥60 GWd/MTU)
HYCD#5	3×1 in.+3 in.	Zircaloy-4	20, 110, 280, 50	To be irradiated	Low H content to address hydride reorientation (equiv. burnup: TBD)
HYCD#6	6 in.	Zircaloy-4	440	To be irradiated	Single 6-in.-long sample having lower H content than HYCD#3 (equiv. burnup: TBD)

This page intentionally left blank.
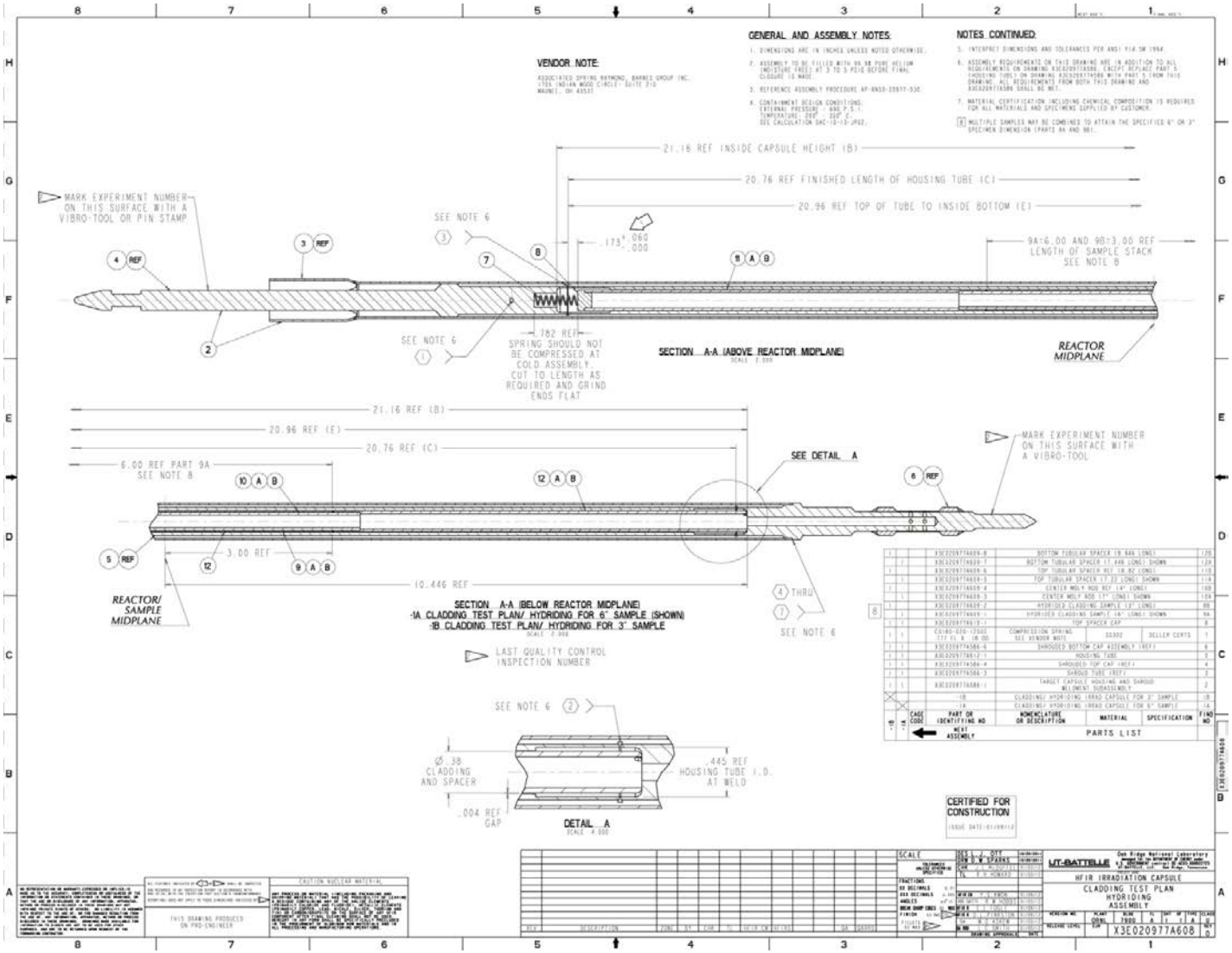
APPENDIX C
DRAWING X3E020977A608